High-dimensional adaptive optics techniques and applications

A Thesis Submitted to the Board of the Faculty of the Mathematical, Physical and Life Sciences Division for the degree of *Doctor of Philosophy* in the University of Oxford

Yifei Ma

St Anne's College

October 2025

Abstract

High-dimensional adaptive optics techniques and applications

By Yifei Ma

Adaptive optics (AO) has traditionally been associated with feedback correction of phase aberrations. However, in practical imaging systems, performance is also significantly limited by coupled vectorial errors, including retardance and diattenuation. This thesis advances AO toward a high-dimensional framework that treats these error channels jointly. As a first step, this work develops and validates the vectorial extension of AO – pushing correction beyond scalar phase error – and establishes methods, metrics, and devices that pave the way to unified, high-dimensional AO toolkit.

First, a vectorial adaptive optics (V-AO) correction module was implemented in a wide-field Stokes polarimetric microscope. Using a pupil-intensity feedback strategy, the system successfully compensated for spatially varying polarisation aberrations, improving the vectorial uniformity across the field of view from 77.1% to 91.2% and achieving a vectorial precision of over 95% across various samples.

Then the vectorial aberration correction concept is subsequently realised from the object's perspective, hence termed as object-wise adaptive optics (O-AO). In this approach, a tunable arbitrary retarder array, realised by cascading polarisation

modulators, is configured to form an inverse object for directly compensating retardance aberrations from the object’s perspective.

Following the investigation of retardance correction, the capability of V-AO to correct diattenuation aberrations in non-depolarising media is investigated. The correction performance is quantitatively assessed using advanced optical skyrmionic beams as indicators.

Finally, I study the correctability limit of V-AO in the presence of diattenuation in non-depolarising media. The correction performance is assessed using optical skyrmion beams as sensitive indicators, and the role of intensity loss and detector noise is made explicit. For example, when the diattenuation is strong (extinction ratio E=3.36), some states fall below the detection threshold and become unrecoverable, whereas for a weaker diattenuation (E=1.65) the Stokes field can be effectively restored.

A summary of this thesis and an outlook on future research directions is provided, focusing on further advancing high-dimensional AO methodology and expanding its applications to a broader range of practical optical systems.

Acknowledgements

To me, the PhD has often felt like crossing a dark sea. My two supervisors were the lighthouses that kept me on course. I am deeply grateful to Prof. Martin Booth for giving me the opportunity to come to Oxford, and for your constant guidance and steadfast support. Your leadership has always been a real model to me, and your broad vision, intellectual generosity, and unwavering standards have shaped my growth. I am deeply grateful to Prof. Chao He. You have been more than an academic supervisor – you have been a mentor in life, my captain, and a brother in all but blood. Under your guidance I gained not only valuable research results, but also many philosophies and principles for navigating life and adapting to society. It has been an honor to sail on the Vectorial Optics and Photonics (VOP) group/ship with you and with all our members; I believe together we will accomplish great things, and we will chart our own great course.

I am grateful to Professor Steve Morris for your generous and incisive advice on my doctoral work. Your continued support has meant a lot and you have long been a role model for me. I also thank Prof. Patrick Salter and Prof. Steve Elston for many constructive discussions and practical advice. My sincere thanks go to Dr. Jingyu Wang and Dr. Qi Hu for their patient guidance and generous help.

I would like to thank all members of VOP group. In particular, Dr. Zimo Zhao, thank you for your constant help. You are a truly talented engineer – whenever a technical problem appeared, you always found the most elegant solution. Working with you has been a joy, and I wish you every success in the years ahead. Mr. An Aloysius Wang, your creative ideas have inspired me again and again, and your steadfast support and care has meant a lot. I will always remember our many Pokémon hunts; I hope you will soon find your own comfort and happiness, and that you will come back to VOP (and open that café!). Mr. Yuxi Cai, I have learnt much from your critical thinking and I am inspired by your entrepreneurial spirit. You are a doer with real drive – may your current project (cohomology) reach a happy conclusion, and may you continue to make great in education business. I also thank Xuke Qiu, Tade Marozsak, Yunqi Zhang, Runchen Zhang, Ruofu Liu, Ji Qin, Jinge Guo, Yihan Liu, Zhenglin Li, and Xiaoyi Shang for your kindness, patience, and the many meaningful conversations that taught me so much. I am also grateful to all group members in DOP group, especially Zhi-Kai Pong and Linquan Yuan, for valuable discussions and easy, cheerful chats; I have learnt a great deal from your work as well.

My heartfelt thanks go to my partner, Yihan (Eva) Liu. Thank you for your unconditional love and support. You are my closest companion, my friend with whom I share everything, and my teammate as we face the uncertain world together. I am lucky to have you. Finally, I thank my parents. I am truly fortunate that we have always related to one another almost as friends. Thank you for your guidance, and for your unconditional love and support for every decision I have made. Wherever I am, home is the safe harbour deep in my heart. I love you.

Yifei Ma

August 2025

Publication

Thesis-related

1. **Yifei Ma**, Zimo Zhao, Yuanxing Shen, Binguo Chen, An Aloysius Wang, Yuxi Cai, Ji Qin, Runchen Zhang, Yunqi Zhang, Jiahe Cui, Bangshan Sun, Jiawen Li, Yuzhu Shi, Liangyu Deng, Honghui He, Lin Luo, Yonghong He, Yun Zhang, Ben Dai, Daniel J Royston, Steve J Elston, Stephen M Morris, Martin J Booth, and Chao He. **Using optical skyrmions to assess vectorial adaptive optics capabilities in the presence of complex aberrations**. *Science Advances* **11***,* eadv7904 (2025).

2. **Yifei Ma**, Zimo Zhao, Jiahe Cui, Jingyu Wang and Chao He. **Vectorial adaptive optics for advanced imaging systems**. *Journal of Optics* **26**, 065402 (2024).

3. [Chao He, Binguo Chen, Zipei Song, Zimo Zhao, **Yifei Ma**], Honghui He, Lin Luo, Tade Marozsak, An Aloysius Wang, Rui Xu, Peixiang Huang, Jiawen Li, Xuke Qiu, Yunqi Zhang, Bangshan Sun, Jiahe Cui, Yuxi Cai, Yun Zhang, Andong Wang, Mohan Wang, Patrick Salter, Julian AJ Fells, Ben Dai, Shaoxiong Liu, Limei Guo, Yonghong He, Hui Ma, Daniel J. Royston, Steve J. Elston, Qiwen Zhan, Chengwei Qiu, Stephen M. Morris, Martin J. Booth and Andrew Forbes. **A reconfigurable arbitrary retarder array as complex**

structured matter. *Nat Commun* **16**, 4902 (2025). *Co-first author (equal contribution)*

4. [Zimo Zhao, **Yifei Ma**, Zipei Song], Jacopo Antonello, Jiahe Cui, Binguo Chen, Jingyu Wang, Bangshan Sun, Honghui He, Lin Luo, Julian AJ Fells, Steve J Elston, Martin J Booth, Stephen M Morris, Chao He. **Intensity adaptive optics.** *Light Sci Appl* **14**, 128 (2025). *Co-first author (equal contribution)*

5. An Aloysius Wang, Zimo Zhao, **Yifei Ma**, Yuxi Cai, Runchen Zhang, Xiaoyi Shang, Yunqi Zhang, Ji Qin, Zhi-Kai Pong, Tádé Marozsák, Binguo Chen, Honghui He, Lin Luo, Martin J Booth, Steve J Elston, Stephen M Morris, Chao He. **Topological protection of optical skyrmions through complex media.** *Light Sci Appl* **13**, 314 (2024). *Elected as Annual Back Cover*

6. Yijie Shen, Chao He, Zipei Song, Binguo Chen, Honghui He, **Yifei Ma**, Julian AJ Fells, Steve J Elston, Stephen M Morris, Martin J Booth, Andrew Forbes. **Topologically controlled multiskyrmions in photonic gradient-index lenses**. *Physical Review Applied* 21(2), 2024.

Conference

The Oxford International Conference on Advanced Optics and Photonics (highlighted by UNESCO's International Day of Light) – Conference Secretary

Oxford, UK, July 2024

Light Conference 2024 – Oral presentation

Changchun, China, June 2024

SPIE Photonics West 2024 – Oral presentation

San Francisco, US, January 2024

List of Abbreviations

AO	Adaptive optics
V-AO	Vectorial adaptive optics
SoP	State of polarisation
SLM	Spatial light modulator
DM	Deformable mirror
DoP	Degree of polarisation
DoLP	Degree of linear polarisation
DoCP	Degree of circular polarisation
PSA	Polarisation state analyser
PSG	Polarisation state generator
PS	Poincaré sphere
PB	Pancharatnam–Berry
QWP	Quarter-wave plate
O-AO	Object-wise adaptive optics
ND	Neutral density
FID	Focal intensity distribution
SN	Skyrmion number
ATA	Arbitrary to arbitrary
LUT	Look-up table
CN	Condition number
EWV	Equally weighted variance
PSIV	Poincaré sphere internal volume
DLW	Direct laser writing

PSF	Point-spread function
SIM	Structured illumination microscopy
SDOM	Saturated depletion optical microscopy

Contents

Chapter 1: Overview

Chapter 2: Background

Chapter 3: V-AO for advanced polarimetric imaging system

Chapter 4: Object-wise adaptive optics adopting tuneable arbitrary retarder array

Chapter 5: Assessing V-AO correction for complex aberrations

Chapter 6: Conclusion and Future Work

Chapter 1 Overview

1.1 Introduction

This thesis investigates the principles, implementation strategies, and applications of high-dimensional adaptive optics – a next-generation aberration correction technique that extends conventional adaptive optics (AO) beyond scalar phase manipulation. In practice, optical systems also suffer from polarisation errors (retardance, diattenuation, etc.) and intensity errors. These errors often act together and set the true limit of image quality and information fidelity.

The work presented here develops methods and tools that move AO toward this broader, higher-dimensional view. In particular, the thesis begins with the vectorial part of high-dimensional AO framework – vectorial adaptive optics (V-AO) – and demonstrates correction effect and correction capacity for polarisation aberration in non-depolarising media. The results provide a pathway to a unified high-dimensional AO toolbox that can be configured for different architectures and applications.

1.2 Research motivation

Optical imaging techniques such as microscopy have long been an essential tool for biomedical research. It has the ability to reveal multidimensional structural information of a specimen in a non-invasive and non-contact manner[1–3]. Although the resolution of conventional optical systems is fundamentally limited by diffraction, the actual imaging performance is further degraded by optical aberrations, which always exist in optical imaging systems. These aberrations often arise when light propagates through complex media with spatially varying refractive indices, thereby preventing diffraction-limited imaging[4]. The impact of such aberrations becomes more severe when imaging deeper into tissues, where both resolution and image quality are significantly compromised.

To address these limitations, AO has been introduced as a powerful technique for compensating wavefront distortions. The AO technique was first proposed by Horace W. Babcock in 1953[5] and further developed by Linnick in 1957[6] to improve the quality of astronomical images through closed-loop correction of wavefront aberration. Traditional AO systems primarily focus on correcting scalar phase aberrations of the optical wavefront. However, subsequent research has shown that other dimensions of aberration – notably retardance and diattenuation (polarisation errors) and intensity errors – may have a more significant effect on the performance of optical system. Such aberrations perturb the state of polarisation (SoP), introduce extra (dynamic and geometric) phase distortions[7–9], cause spatial intensity error[10], and may reduce the degree of polarisation (DoP)[11], all of which lead to a reduced performance of the system[12]. These effects become particularly pronounced in high-NA imaging, deep tissue observations[13], and polarisation-sensitive imaging techniques, such as Stokes and Mueller microscopes[14–19].

Taken together, these points indicate that practical imaging architectures will benefit from high-dimensional AO framework that senses and corrects multiple aberration dimensions. This thesis advances that direction by first establishing the vectorial foundation of this framework in non-depolarising media and then analysing its correction limits. Three complementary studies are undertaken:

1) V-AO in wide-field polarimetric imaging – a polarisation and phase correction module driven by intensity-based feedback based on a microscope is implemented. New metrics for evaluating vectorial precision and uniformity across the field of view are also introduced.

2) Object-wise AO (O-AO) with an arbitrary retarder array (another type of V-AO) –The key idea is to treat the object (or a part of the optical system) as a spatially varying vectorial element that distorts the polarisation state across the field of view. Instead of correcting these distortions only in the pupil plane, O-AO aims to build a programmable “inverse object” whose local Jones/Mueller response cancels the measured vectorial aberration. In practice, this inverse object

is realised using a pixel-addressable retarder array, so that different retardance and fast-axis orientation can be applied at different field points. The aims of O-AO are: (i) to measure or estimate the spatially varying vectorial aberration in a full-field manner, (ii) to map this aberration to the settings of the retarder array, and (iii) to restore a spatially uniform state of polarisation (SoP) and improve the accuracy of downstream vectorial imaging.

3) Probing limits of the correction ability of V-AO system towards complex aberration – a combined theoretical and experimental analysis investigates the fundamental limits of V-AO performance when correcting complex aberrations.

Together, these studies establish the vectorial core of high-dimensional AO that can be further extended to intensity control and, ultimately, depolarisation manipulation.

1.3 Thesis outline

Chapter 2 begins with a brief introduction to the fundamental polarisation properties of light and objects. It then details the two main techniques used in the research projects: AO technique and polarisation measurement methodologies. For the AO section, the basic working principle, correction device and implementation of conventional phase AO, and advanced V-AO are introduced. In the polarisation measurement section, both Stokes polarimetry and Mueller matrix polarimetry are detailed. This comprehensive background provides the necessary context for understanding the subsequent chapters.

Chapter 3 focuses on the advanced V-AO technique and how V-AO can enhance polarimetric imaging systems by correcting complex polarisation aberrations and improving the quality of vectorial information. This chapter begins with an introduction to V-AO and its correction strategies. It highlights the limitations of conventional AO, which primarily addresses phase aberrations, and explains how V-AO extends these capabilities to correct polarisation aberrations. The key concepts and importance of V-AO in improving the performance of optical systems, particularly in maintaining the precision and uniformity of vectorial information is also introduced.

Chapter 4 explores the development and implementation of O-AO optics by using a tunable arbitrary retarder array. This innovative approach aims to address the limitations of traditional V-AO by providing dynamic control over both polarisation and phase aberrations from object aspect. This chapter highlights the ability of O-AO to achieve precise control over vectorial aberrations, making it a powerful tool for various optical applications.

Chapter 5 investigates the limits of V-AO by utilising optical skyrmions to probe and characterise the correction ability of V-AO systems towards complex aberration for non-depolarising media. While V-AO has successfully corrected retardance aberrations, this project focuses on the complex diattenuation aberration. The chapter begins by explaining the fundamental properties of diattenuation aberrations, highlighting the inherent difficulties in correcting diattenuation aberrations due to the reduction in intensity and alteration of polarisation state. To evaluate the correction abilities of V-AO, the topological property of optical skyrmions serves as a criterion. It also highlights the potential application of optical skyrmion to evaluate the performance of Stokes vector polarimetry under diattenuation.

Chapter 6 summarises the thesis and outlines the potential future work towards advanced high-dimensional AO methodologies, such as control of depolarisation and multi-dimensional sensing and correction. It also proposes their potential application in practical scenarios, from laser/nano-fabrication to optical communication areas.

Chapter 2 Background

2.1 Introduction to polarisation

Light, as an electromagnetic wave, consists of mutually perpendicular electric and magnetic fields[20–22]. Polarisation describes the orientation of the electric field vector in the plane perpendicular to the direction of propagation. For a monochromatic beam traveling along the z-axis, the electric field at any instant can be decomposed into two orthogonal components in the x- and y-directions, each with its own amplitude and phase. Unless otherwise stated, the analysis in this thesis assumes the use of monochromatic light; wavelength dependence and broadband (chromatic) effects are not considered. Here the plane wave can be expressed as:

$$\boldsymbol{E} = \boldsymbol{E_0} \cos(\tau + \delta_0) \tag{2.1}$$

where $\boldsymbol{E}$ denote the electric-field vector, $\boldsymbol{E_0}$ is the vector amplitude and δ_0 is the initial phase. The variable $\tau = \omega t - kz$ is the travelling-wave phase, with ω is the angular frequency and k is the wavenumber (in a medium of refractive index n at wavelength λ, $k = 2\pi n/\lambda$). Writing the field in Cartesian components gives:

$$\begin{cases} \boldsymbol{E_x} = E_{0x}\cos(\tau + \delta_1) \\ \boldsymbol{E_y} = E_{0y}\cos(\tau + \delta_2) \\ \boldsymbol{E_z} = 0 \end{cases} \tag{2.2}$$

where E_{0x} and E_{0y} are the amplitude of x- and y- components, and δ_1 and δ_2 are their respective initial phase. The field is transverse ($\boldsymbol{E_z} = 0$) as the electric and magnetic fields are orthogonal to the direction of propagation. Then the state of polarisation (SoP) is determined by the amplitude ratio and relative phase difference$\Delta = \delta_2 - \delta_1$.

When the relative phase difference between these two orthogonal components is zero or π radians, the beam is linearly polarised. If the phase difference is ±π/2 radians and the amplitudes are equal, the resulting beam is circularly polarised, with the electric field vector following a circular trajectory in the transverse plane. More generally, any arbitrary combination of phase and amplitude yields elliptical polarisation, which includes both linear and circular polarisation as special cases. In contrast, if the electric field components fluctuate randomly and become uncorrelated, the beam is considered unpolarised.

Because SoP is fully determined by the relative amplitudes and phase of two transverse components, it is naturally represented by vectors. Two concise vector formalisms are used throughout this thesis[23–27]:

1) Jones vector – a complex 2-element column vector that represents both amplitude and phase, ideal for describing fully polarised light.

2) Stokes vector – a real 4-element vector derived from intensity measurements, applicable to fully, partially, or unpolarised light.

2.1.1 Vectorial properties of light

2.1.1.1 Jones vector

A fully polarised monochromatic beam can be described by two orthogonal electric field components E_x and E_y. Their amplitudes A and B and their phase difference $\delta = \varphi_x - \varphi_y$ completely determine the SoP. By collecting the two complex amplitudes into a column, we obtain the Jones vector:

$$J = \begin{bmatrix} E_x \\ E_y \end{bmatrix} = \begin{bmatrix} Ae^{i\varphi_x} \\ Be^{i\varphi_y} \end{bmatrix} \tag{2.3}$$

As both magnitude and phase are retained, the Jones formalism can predict any coherent effect such as interference, retardance, or diattenuation introduced by an optical element. Such elements act through a 2 × 2 complex Jones matrix:

$$J' = M_{Jones} \bullet J \tag{2.4}$$

The method is compact and powerful, while it applies only when the beam keeps a fixed phase relation between its field components; it breaks down once depolarisation or randomness presents.

2.1.1.2 Stokes vector

When the beam is partially polarised or even unpolarised, its electric field fluctuates so that a single, fixed phase relation no longer exists. In such cases, we adopt the Stokes vector, a real, four-element column vector constructed from straightforward intensity measurements[28–30]:

1) S_0 is the total intensity.

2) S_1 measures the degree of horizontal or vertical polarisation

3) S_2 measures the degree of +45° or -45° linear polarisation

4) S_3 measures the degree of right circular or left circular polarisation.

$$S = \begin{pmatrix} S_0 \\ S_1 \\ S_2 \\ S_3 \end{pmatrix} = \begin{pmatrix} I \\ I_x - I_y \\ I_{45^\circ} - I_{-45^\circ} \\ I_R - I_L \end{pmatrix} \tag{2.5}$$

The values of these four parameters range from -1 to 1 and satisfy:

$$S_0{}^2 \geq S_1{}^2 + S_2{}^2 + S_3{}^2 \tag{2.6}$$

Together these four parameters describe any statistical mixture of polarisation states. Several scalar quantities derived from the Stokes vector are particularly useful:

1) Degree of polarisation: quantifies how much of the beam is polarised (1 = fully, 0 = unpolarised).

$$DoP = \frac{\sqrt{S_1{}^2+S_2{}^2+S_3{}^2}}{S_0} \tag{2.7}$$

2) Degree of linear polarisation (DoLP): measures the linear polarised component.

$$DoLP = \frac{\sqrt{S_1{}^2+S_2{}^2}}{S_0} \tag{2.8}$$

3) Degree of circular polarisation (DoCP): captures the circular polarised component.

$$DoCP = \frac{S_3}{S_0} \tag{2.9}$$

Polarisation transformations – including retardance, diattenuation and depolarisation – are described by a 4 × 4 Mueller matrix:

$$S' = M_{Mueller} \cdot S \tag{2.10}$$

Because both S and M rely only on measured intensities, the Stokes–Mueller formalism links naturally to real instruments and remains valid regardless of coherence.

2.1.2 Vectorial properties of objects

In the previous subsection, we described the SoP of light using either a Jones or Stokes vector, depending on whether the light is fully or partially polarised. In the following section we illustrate how these vectors change after the beam passes through or interacts with an object, such as a lens, a waveplate, a piece of glass, or even a biological sample.

2.1.2.1 Jones matrix

For a fully polarised beam, the input electric field is represented by a Jones vector $\boldsymbol{J_{in}}$. The effect of the object is described by a 2 × 2 complex Jones matrix M_{Jones}, which transforms the input into the output field:

$$\boldsymbol{J_{out}} = M_{Jones} \bullet \boldsymbol{J_{in}} = \begin{pmatrix} J_{11} & J_{12} \\ J_{21} & J_{22} \end{pmatrix} \bullet \boldsymbol{J_{in}} \tag{2.11}$$

Since the Jones formalism preserves amplitude and absolute phase, it captures all coherent and non-depolarising interactions in a simple and efficient form.

2.1.2.2 Mueller matrix

If the object introduces depolarisation, the Jones formalism is no longer adequate. Instead, we use the Stokes–Mueller approach, where the input Stokes vector S_{in} is transformed by a 4 × 4 real Mueller matrix $M_{Mueller}$:

$$\boldsymbol{S_{out}} = M\boldsymbol{S_{in}} = \begin{bmatrix} m_{11} & m_{12} & m_{13} & m_{14} \\ m_{21} & m_{22} & m_{23} & m_{24} \\ m_{31} & m_{32} & m_{33} & m_{34} \\ m_{41} & m_{42} & m_{43} & m_{44} \end{bmatrix} \boldsymbol{S_{in}} \tag{2.12}$$

Each matrix element corresponds to a measurable intensity ratio, meaning the Mueller-formalism is valid for any object – whether it is a birefringent crystal, thin-film coating, or scattering biological tissue – and valid for any input light, from coherent to unpolarised.

2.2 Polarimetry

Polarimetry is a widely used technique to measure the SoP of light and, by extension, how that state is altered by an object or medium. A polarimetric instrument deliberately modulates the beam’s polarisation, records a set of intensities with a detector, and then reconstructs the Stokes vector of the light or Mueller matrix of the object. Accordingly, polarimetric techniques fall into two main categories:

1) Stokes polarimetry – determines the SoP emerging from a scene or object.

2) Mueller matrix polarimetry – determines the polarisation transforming ability of the object.

2.2.1 Stokes polarimeter

A Stokes polarimeter treats the unknown beam as a four-component vector:

$$\boldsymbol{S} = [S_0, S_1, S_2, S_3]^T \tag{2.13}$$

where S_0 is the total intensity and (S_1, S_2, S_3) encode the SoP. Since each Stokes parameter is defined through intensity differences, a Stokes instrument operates purely on intensity measurements.

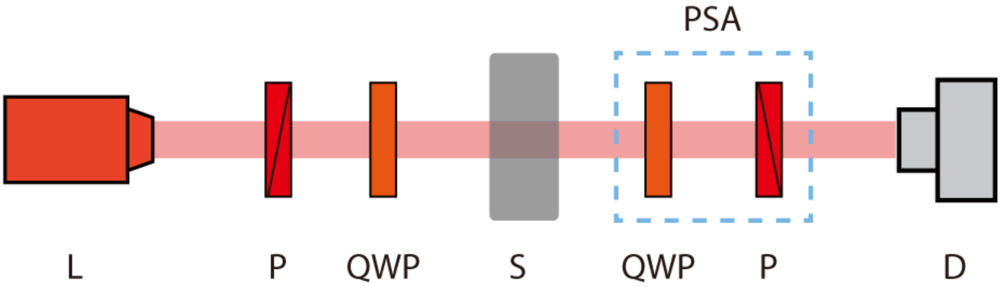

Figure 2.1: General setup of Stokes polarimeter. L: light source; P: fixed polariser; QWP: quarter-wave plate; S: sample; PSA: polarisation state analyser; D: detector.

The core of a Stokes polarimeter is the polarisation-state analyser (PSA) followed by a detector, as shown in Fig. 2.1. A widely adopted PSA configuration consists of a fixed linear polariser and a rotatable quarter-wave plate[31–36]. By rotating the wave plate to at least four linearly independent angles, the PSA projects the beam onto four known analyser states and records the corresponding intensities. For the qth measurement, assuming the incident Stokes vector maintain the same, the output light field can be described as:

$$S_{out}^{q} = M_P M_{QWP}^{q} S_{in} \tag{2.14}$$

where S_{in} represents the input Stokes vector, M_P and M_{QWP}^q are the Mueller matrix of the polariser and quarter-wave plate, respectively. The overall measurement process can then be expressed as:

$$P = W \bullet S_{in} \tag{2.15}$$

where the instrument matrix W is defined as a $q \times 4$ matrix that can be derived from $M_P M_{QWP}^q$, P is a $q \times 1$ intensity vector formed by the measured signals.

With four independent analyser settings, the instrument matrix W becomes a unique and non-singular 4×4 matrix, thus the incident Stokes vector can be retrieved directly:

$$S_{in} = W^{-1} \bullet P \tag{2.16}$$

Calibration proceeds by measuring a small set of reference states (e.g. horizontal, vertical, ±45° linear and circular polarisations) to determine the actual W including non-idealities such as finite extinction ratio and slight retardance errors. It is also good practice to normalise the recovered vector by S_0 to obtain the normalised Stokes vector, and to report the DoP which quantifies partial depolarisation in the measurement. For imaging polarimeters, the same analysis is performed pixelwise; the trade-offs then lie between temporal modulation speed, per-pixel signal-to-noise ratio (SNR), and the number of analyser states.

2.2.2 Mueller matrix polarimeter

While Stokes polarimetry provides information about the output polarisation state, Mueller matrix polarimetry offers a more complete picture by characterising how the object transforms all possible input SoPs. Specifically, it reconstructs the full 4×4 Mueller matrix of the sample, where each of the 16 real-valued elements encodes a particular polarisation response – such as retardance, diattenuation, and depolarisation[37–42]. As a result, Mueller matrix measurements provide much richer information than Stokes measurements.

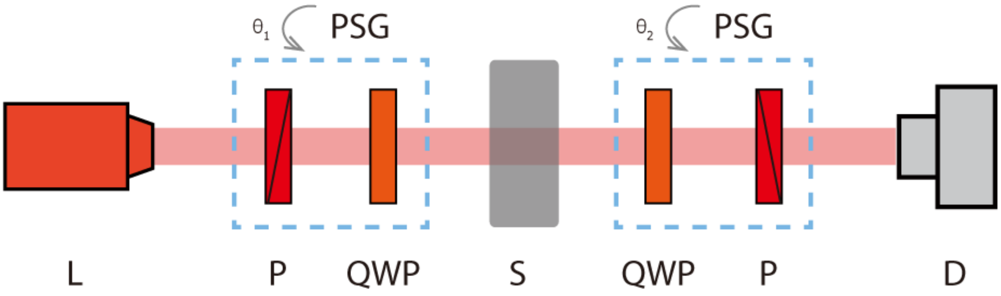

Figure 2.2: General setup of Mueller matrix polarimeter. L: light source; P: fixed polariser; QWP: rotating quarter-wave plate; PSG: polarisation state generator; S: sample; PSA: polarisation state analyser; D: detector.

Fig. 2.2 illustrates one of the most commonly used Mueller matrix polarimeter configuration firstly proposed by Azzam[43], where both the polarisation state generator (PSG) and PSA employ a fixed polariser and a rotating quarter-wave plate. The key idea is to rotate the two quarter-wave plates at different angular velocities, typically with an angular ratio $\theta_1 = 5\theta_2$, enabling Fourier-based demodulation of the signal.

The main principle of this dual-rotating quarter-wave plate method can be expressed as:

$$I_{out} = (1\ 0\ 0\ 0)M_{P2}M_{QW2}M_{sample}M_{QW1}M_{P1}S_{in} \tag{2.17}$$

This measurement can be compactly written as:

$$I_{out} = A \bullet M_{sample} \bullet P = \sum_{i,j=1}^{4} u_{ij}m_{ij} \tag{2.18}$$

where S_{in} is the incident Stokes vector, M_{P1} and M_{P2} are the Mueller matrices of linear polarisers, M_{QW1} and M_{QW2} represent the those of quarter-wave plates; M_{sample} represents the Mueller matrix of the sample and I_{out} is the intensity received by the detector. The terms $A = (1\ 0\ 0\ 0)M_{P2}M_{QW2}$ and $P = M_{QW1}M_{P1}S_{in}$ combine the analyser and generator effects respectively, and their product gives rise to weight coefficients ${u_{ij}}^{43,44}$:

$$u = \frac{1}{4}\begin{bmatrix} 1 & \cos^2 2\theta_1 & \sin 2\theta_1 \cos 2\theta_1 & \sin 2\theta_1 \\ \cos^2 2\theta_2 & \cos^2 2\theta_1 \cos^2 2\theta_2 & \sin 2\theta_1 \cos 2\theta_1 \cos^2 2\theta_2 & \sin 2\theta_1 \cos^2 2\theta_2 \\ \sin 2\theta_2 \cos 2\theta_2 & \cos^2 2\theta_1 \sin 2\theta_2 \cos 2\theta_2 & \sin 2\theta_1 \sin 2\theta_2 \cos 2\theta_1 \cos 2\theta_2 & \sin 2\theta_1 \sin 2\theta_2 \cos 2\theta_2 \\ -\sin 2\theta_2 & -\cos^2 2\theta_1 \sin 2\theta_2 & -\sin 2\theta_1 \sin 2\theta_2 \cos 2\theta_1 & -\sin 2\theta_1 \sin 2\theta_2 \end{bmatrix} \tag{2.19}$$

where θ_1 and θ_2 are the rotation angles of the quarter waveplates R_1 and R_2 respectively. By rotating the waveplates continuously, the output intensity becomes a periodic function that can be expanded into a Fourier series:

$$I_{out} = a_0 + \sum_{n=1}^{12}(a_n \cos 2n\theta_1 + b_n \sin 2n\theta_1) \tag{2.20}$$

where a_n and b_n are Fourier coefficients, θ_1 is the rotation angle of the first quarter waveplate. Then the Mueller matrix can be obtained as follows[43,45],

$$M_{sample} = \begin{bmatrix} a_0 - a_2 + a_8 - a_{10} + a_{12} & 2a_2 - 2a_8 - 2a_{12} & 2b_2 - 2b_8 - 2b_{12} & b_1 - b_9 - b_{11} \\ -2a_8 + 2a_{10} - 2a_{12} & 4a_8 + 4a_{12} & 4b_{12} - 4b_8 & -2b_9 + 2b_{11} \\ -2b_8 + 2b_{10} - 2b_{12} & 4a_8 + 4b_{12} & 4a_8 - 4a_{12} & 2a_9 - 2a_{11} \\ b_3 - b_5 + b_7 & -2b_3 - 2b_7 & -2a_3 + 2a_7 & -a_4 + a_6 \end{bmatrix} \tag{2.21}$$

and the Mueller elements are recovered algebraically from the 25 Fourier coefficients via (2.21). In practice, as few as 30 intensity images per period suffice to estimate all coefficients with good accuracy.

As with Stokes instruments, calibration is essential. Retardance offsets, angle zero-points, and polariser extinction ratios can be identified by measuring a set of well-characterised reference samples (air, linear polarisers at several angles, known retarders). The physical-realisability constraints on M_{sample} provide additional sanity checks during reconstruction. For Mueller polarimetry, the modulation can be performed either temporally (sequential frames[14,18,46–48]) or spatially (division-of-wavefront/focal-plane designs[49–56]), trading off acquisition speed against signal-to-noise ratio (SNR) and calibration complexity[48].

For both Stokes and Mueller matrix polarimeter, rotating elements introduce mechanical error and slow acquisition speed. In practice, fast-modulation devices such as liquid-crystal variable retarders[47,57,58] or SLMs can replace the rotating element. These alternatives offer improved temporal resolution and enhance mechanical stability, making them more suitable for dynamic or real-time measurements.

2.3 Adaptive optics

Aberrations widely exist in optical imaging systems. They may arise from imperfect optical components, sample-induced refractive index variations, or misalignment within the system. Such errors span multiple dimensions – scalar phase, polarisation (retardance, diattenuation, etc.) and intensity errors — and together they degrade the system performance. These effects are especially critical in high-resolution microscopy, polarisation-sensitive imaging, and deep-tissue imaging. High-dimensional AO framework addresses these challenges by combining aberration sensing (or estimation) with real-time correction to recover image quality and information fidelity.

This chapter focuses on the two pillars used throughout the thesis: (1) phase AO, which corrects scalar phase distortions; and (2) vectorial AO (V-AO), which extends correction to the vectorial domain (phase and polarisation) in non-depolarising media. Intensity-uniformity control and depolarisation-handling strategies are noted here for context but are outside the scope of this section.

2.3.1 AO correction elements

AO correction is achieved by setting the conjugate aberration onto the wavefront with a reconfigurable element. In practice, two types of devices are used most widely (as shown in Fig. 2.3): DMs, which reshape a reflective surface to change the optical path in reflection, and SLMs, typically liquid-crystal devices that modulate phase via voltage-controlled birefringence.

A DM is a wavefront-correction device operating in reflection mode, consisting of a reflective surface that can be either continuous or segmented[59–62]. By applying mechanical forces through actuators, the DM surface shape is actively adjusted, altering the optical path length and thereby correcting wavefront distortions.

Continuous surface is the most widely used form of DM. In these mirrors, each actuator pushes or pulls the reflective surface to form a smooth, local deformation called an influence function. The overall mirror shape results from the sum of these influence functions. In contrast, segmented DMs consist of independently controlled mirror facets, allowing each segment to adjust in piston mode (forward or backward motion) and potentially tip and tilt.

The capability of wavefront correction depends significantly on the number and arrangement of actuators. Generally, higher actuator counts provide finer correction control. An advantage of DM is their insensitivity to wavelength and incident polarisation state, making them particularly suitable for applications such as fluorescence microscopy, where multiple illumination and detection wavelengths are common.

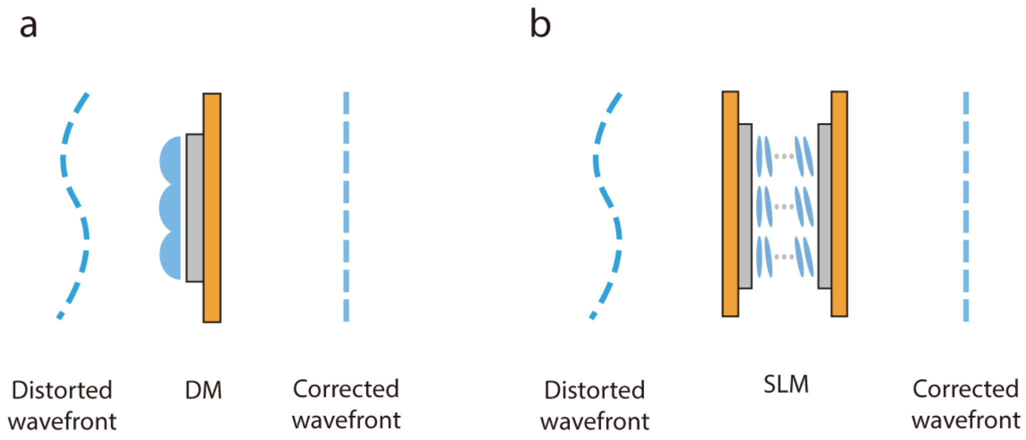

Figure 2.3: General schematic of AO correction elements. (a) DM: consists of a reflective surface. (b) SLM: consists of liquid-crystal molecules whose effective refractive index changes with applied electric field.

Generally, a SLM is a liquid-crystal based device capable of modulating the optical path length through changes in refractive index, thus providing wavefront correction[63–65]. In liquid crystal SLMs, an external voltage adjusts the birefringence by reorienting liquid crystal molecules. This, in turn, changes the refractive index experienced by linearly polarised incident light, leading to a precise phase modulation.

Compared to DMs, SLMs typically offer greater spatial resolution due to their higher pixel count. They can generate more complex and precise wavefront profiles, which makes them particularly suitable for correcting aberrations in laser illumination paths, for example in multiphoton microscopy. However, careful consideration is necessary when using SLMs, as they generally require linearly polarised monochromatic incident light. The modulation effect varies with wavelength, potentially causing chromatic issues. For applications involving broadband or multiple wavelengths, DMs may be more suitable due to their achromatic nature.

In summary, while SLMs provide higher spatial resolution and flexible modulation patterns, their wavelength and polarisation dependence contrasts with the wavelength- and polarisation-insensitive characteristics of DMs. Beyond these, platforms – including digital micromirror devices[66] and metasurface based modulators[67] – offer promising routes to faster, more efficient, and more highly integrated AO correctors.

2.3.2 Phase adaptive optics

Traditionally, AO has focused on correcting aberrations in the phase of the optical wavefront. A wavefront represents the surface of constant phase in a propagating electromagnetic field. Any deviation in the wavefront is represented by spatial distortions in this phase profile, often arising from imperfections in optical components or refractive index inhomogeneities in the sample. Such aberrations lead to degraded image quality, including blurring, loss of contrast, and reduced spatial resolution[1,2,68–71].

2.3.2.1 Phase AO correction module

Phase AO employs a single pupil-conjugate corrector – either a DM or an SLM – to impose a conjugate phase $\phi_{correction}(x, y) = -\phi_{aberration}(x, y)$. The choice follows the trade-offs outlined in section 2.3.1: DMs for achromatic, polarisation-insensitive correction; SLMs when higher spatial degrees of freedom or specific phase patterns are required. Closed-loop operation updates the element until the residual phase is minimised by a chosen metric.

2.3.2.2 Phase AO implementation

Phase AO implementation depends critically on how the aberration is sensed or estimated. There are two main approaches: sensor-based and sensor-less methods:

1) **Sensor-based method**

Sensor-based AO systems directly measure the wavefront distortion with a dedicated sensor and then drives the corrector accordingly (as illustrated in Fig.

2.4). The most widely used device is the Shack–Hartmann wavefront sensor, which samples the pupil with a lenslet array and converts local tilts into spot displacements on a camera, from which the full phase map is reconstructed. However, in microscopy, direct wavefront sensing is challenging due to the complex and three-dimensional nature of the specimens. Multiple scattering points or fluorophores create overlapping wavefronts that complicate the measurements. Techniques such as confocal pinholes, coherence gating, or the use of fluorescent beads as "guide stars" have been introduced to isolate the wavefront from the focal region and improve the reliability of sensor-based AO methods in microscopy[79–82].

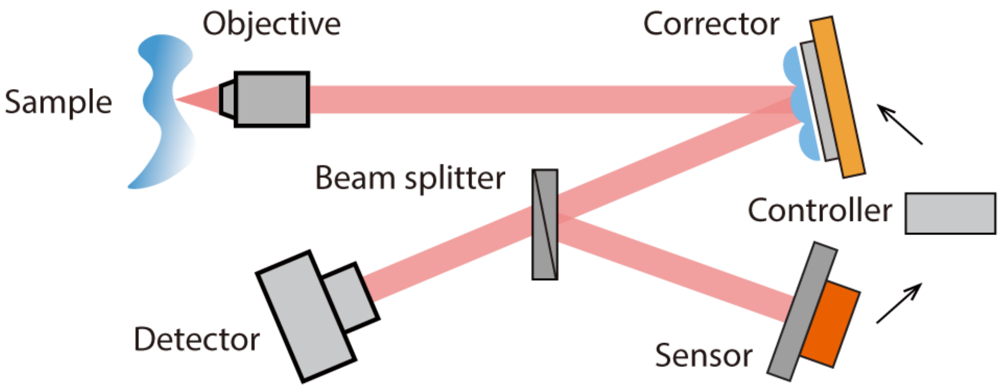

Figure 2.4: General schematic of sensor-based AO system. This configuration consists of a wavefront corrector, a wavefront sensor, and a feedback control system for closed-loop control.

2) **Sensor-less methods**

Indirect sensing approach avoids a separate sensor but rather estimates the aberration from a sequence of images instead. Such method is also known as “modal wavefront sensing”, as in this method, aberration can be expressed as a weighted sum of orthogonal modes (such as Zernike polynomials)[83–85]. By sequentially applying known modal aberrations, a series of images is recorded and image quality metrics such as sharpness guide an optimisation that converges in as few as $2n + 1$ frames for n modes[86–91]. Another sensor-less approach, the "zonal" (or pupil-segmentation) method, divides the pupil into segments, recording images through each segment individually. Local shifts of these images reveal the wavefront tilts in each segment, allowing the reconstruction of the overall aberration. Sensor-less methods simplify the optics and operate effectively even at low signal levels, but they demand careful algorithm design and accurate in-situ calibration of the corrector.

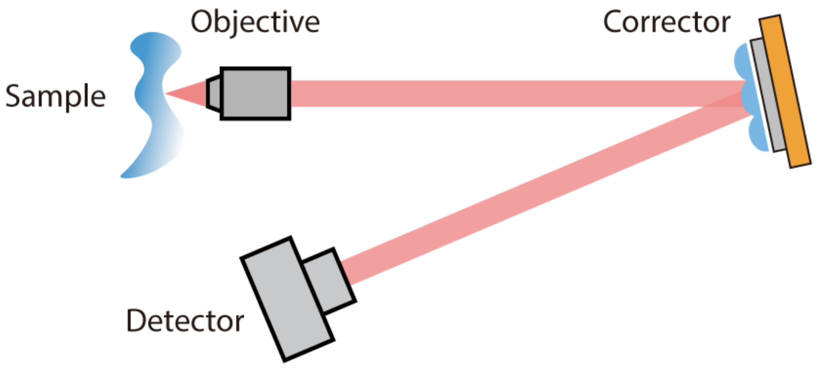

Figure 2.5: General schematic of sensor-less AO system. This configuration consists of a wavefront corrector and a detector only.

2.3.3 Vectorial adaptive optics

Phase AO mainly restores image quality by flattening the scalar phase of the wavefront, however, it leaves polarisation errors uncorrected. Polarisation aberrations – including retardance, diattenuation and depolarisation – can alter the SoPs and also introduce additional phase shifts[23,28,29]. Recent work on polarisation adaptive optics has shown effective correction of polarisation aberration through an adaptive polarisation control system[92], forming the basis for correction of spatially variant polarisation errors. Here, to address both polarisation and phase errors in a unified framework, we extend conventional AO techniques from the phase domain to the vectorial domain, giving rise to V-AO. In V-AO systems, the sensing module measures (or estimates) the combined phase-and-polarisation error, while the correction module applies the appropriate conjugate compensation so that the output field recovers both its intended phase profile and its intended SoP. By jointly compensating phase error and polarisation error together, V-AO delivers a more complete correction than phase AO alone and is therefore essential for high-precision vectorial imaging and beam-engineering applications.

2.3.3.1 V-AO correction module

The V-AO correction module is divided into two parts as illustrated in Fig. 2.6: 1) polarisation correction module that corrects SoP distortions; 2) phase compensation module that compensate any residual scalar phase aberrations.

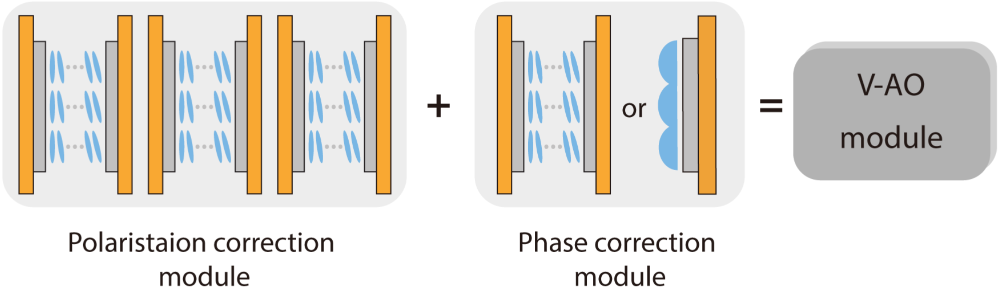

Figure 2.6: Configuration of a V-AO correction module. Generally, a V-AO module consists of a polarisation correction module and a phase correction module.

1) **Polarisation correction module**

For non-depolarising media, the output field after passing through the specimen can be described by a Jones vector. Any undesired change of SoP can therefore be reversed by applying the inverse Jones transformation. A practical approach uses three phase-only liquid-crystal SLMs – or an equivalent set of polarisation modulators – to realise an arbitrary SU(2) transformation, i.e., they can map any input SoP to any desired output SoP with unit amplitude, achieving full vectorial field manipulation[12].

Prior to use, a calibration routine is required to characterise the response of each modulator and stores the drive voltages that realise the required elementary polarisation rotations. During operation, the controller computes the composite inverse Jones matrix based on the measured or estimated polarisation aberration and programmes the three SLMs dynamically, thereby restoring the correct SoP across the pupil, ensuring spatially resolved and accurate vectorial correction.

2) **Phase correction module**

Before V-AO correction, a preliminary phase-flattening step is applied to remove system aberrations (from relay optics, and the modulators themselves) and to establish a stable reference for the subsequent polarisation correction. This pre-correction is usually performed by using a DM or phase SLM driven by a standard sensor-based or metric-optimised loop.

After the polarisation errors have been compensated, small residual scalar phase errors may still remain. These typically arise from two sources: 1) classical optical-path aberrations introduced by the modulators or relay optics; 2) the position-dependent Pancharatnam–Berry (PB) phase introduced during SoP compensation by the V-AO module[7,8,93]. Both contributions can be addressed by introducing traditional phase AO methods.

In summary, the overall V-AO correction module performs aberration compensation in two sequential stages – first correcting vectorial (polarisation-dependent) distortions, then addressing residual scalar phase errors – thereby providing complete correction of joint vectorial aberrations in non-depolarising samples.

2.3.3.2 V-AO implementation：traditional V-AO and O-AO

As in conventional AO, V-AO can be implemented using either with a sensor-based approach, which employs Mueller matrix measurements to capture the properties of the vectorial aberration, or with a sensor-less approach which infers the correction by optimising metrics through modal control.

V-AO can be framed in two perspectives – traditional V-AO (from aspect of light), and O-AO (from aspect of object). In a traditional V-AO configuration, the modulators manipulate directly on the aberrated light field, programming the inverse Jones/phase transformation to restore the target SoP and phase. Rather, O-AO realises the same compensation from the object’s perspective: a reconfigurable object is configured to synthesise an “complementary” object whose Jones/Mueller matrices cancel the sample-induced aberration, thereby achieving direct object-wise compensation.

For traditional V-AO approach, there are three implementations:

1) **Sensor-based method**

This approach employs a full-field Mueller matrix polarimeter (as discussed in Section 2.2.2) as the aberration sensor to characterise the full vectorial properties of the aberration in a pixel-by-pixel manner, as shown in Fig. 2.7. The inverse of this aberration map is then decomposed into three elemental SU(2) rotations and written onto a stack of three phase-only SLMs, producing a spatially uniform output SoP across the field. The residual scalar phase is then removed by a fourth modulator, completing the vectorial and phase compensation in a single closed loop.

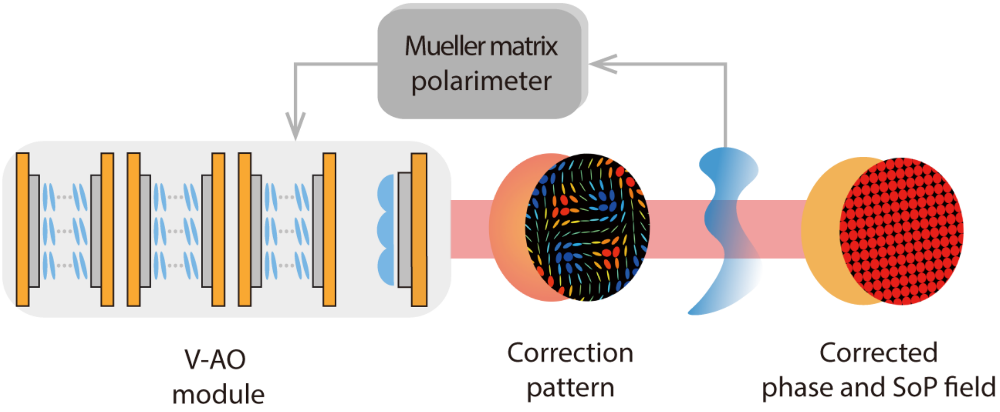

Figure 2.7: General schematic of sensor-based V-AO system. A Mueller matrix polarimeter characterises the vectorial aberration and provides feedback to V-AO module to generate pre-correction pattern. After compensation, a spatially uniform phase and SoP field is achieved.

2) **Quasi-sensorless method**

In this hybrid approach the vectorial aberration is not measured. Instead, a polariser is placed in a pupil-conjugate plane with its transmission axis aligned to the target SoP (take right-hand circular state for example), and the transmitted intensity is used as the sole feedback signal – hence the term quasi-sensorless[12]. A general schematic of quasi-sensorless implementation is illustrated in Fig. 2.8. For any pupil point, the intensity is maximised if and only if the corrected SoP is parallel to the analyser's eigenvector; the intensity therefore acts as an effective metric for the residual SoP error. Operationally, starting from an initial guess, a sequence of trial retardance patterns is written to the two SLMs, an intensity image is recorded after each update, and per-pixel interpolation locates the pattern that yields the local maximum. The resulting SLM maps are then applied as the SoP pre-compensation, after which a conventional phase-only loop on the DM removes the residual scalar phase.

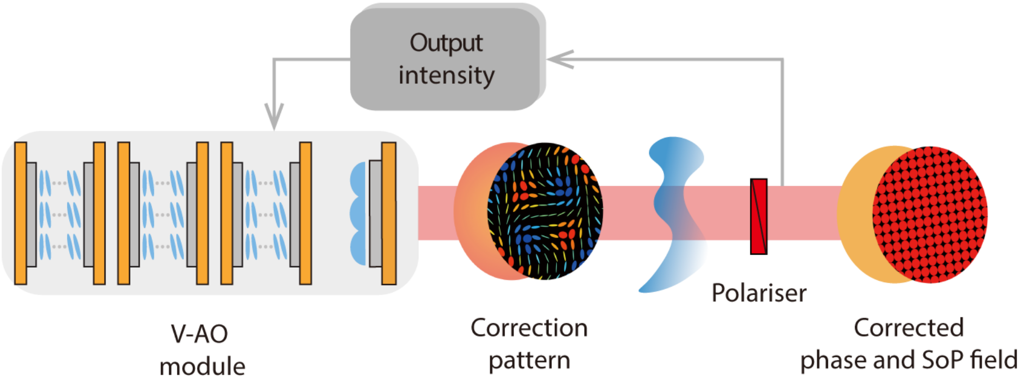

Figure 2.8: General implementation of quasi-sensorless V-AO system. A polariser with its principal axis aligned with the target SoP was placed after the aberration. The transmitted intensity is recorded as feedback to iteratively update the correction pattern applied to the V-AO module.

3) **Sensorless method**

In the fully sensorless variant no analyser or pupil measurement is used. Instead, the system jointly modulates the SLMs and DM with a small set of vectorial modes[12] (e.g., Zernike-based retardance/phase modes) and optimises a focus-quality metric measured at the image plane. Prior knowledge of the aberration symmetry (e.g., axis geometry) constrains the modal search, and the optimisation over mode coefficients maximises the metric, thereby recovering both the SoP and phase without explicit measurement of the aberration. While the sensor-less approach reduces hardware complexity, it typically requires additional image acquisitions and greater computational effort to converge.

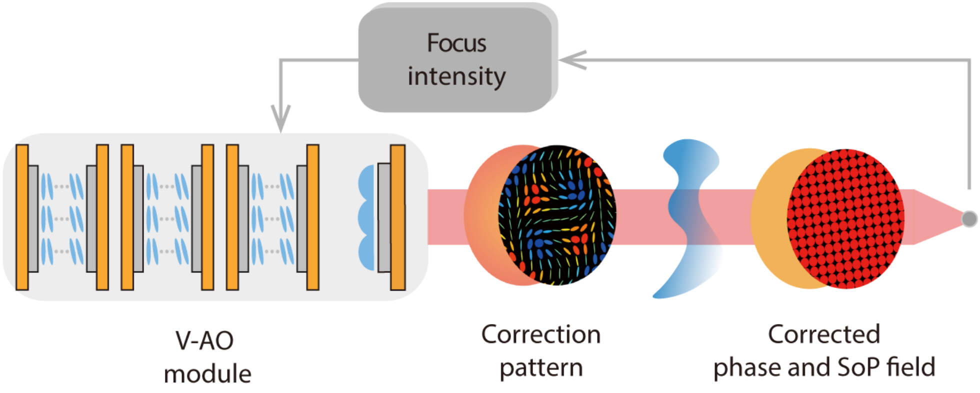

Figure 2.9: General implementation of sensorless V-AO system. The focal intensity is used as feedback for optimising the output phase and SoP field.

4) **O-AO method**

For O-AO approach, two implementations parallel those above. 1) In sensor-based method, a Mueller polarimeter (or equivalent) measures the sample's spatially varying vectorial properties; the controller then programs the reconfigurable object to apply the per-pixel inverse Mueller matrix and thus cancel the aberration directly. 2) In sensorless method, no explicit measurement is conducted; instead, the object is driven with a small set of object modes (e.g., axis-geometry, retardance magnitude, etc.) whose coefficients are optimised against a metric to synthesise the compensating object. The realisation of O-AO architecture, and experimental validation are described in Chapter 4.

2.4 Summary

This chapter establishes the theoretical and methodological foundation for the work presented in the subsequent chapters. First, the vectorial description of light and matter using Jones and Stokes vectors, as well as their corresponding matrix representations is introduced. Section 2.2 then links the theory to practical measurement, outlining Stokes and Mueller polarimeters and explaining how to reconstruct the beams or the objects' vectorial profile through intensity-based measurement. Then a brief overview of AO strategies is presented. Conventional phase AO is considered as a powerful solution for scalar wavefront errors, after which the concept is extended to V-AO, capable of compensating retardance, diattenuation and residual phase aberration. Sensor-based, quasi-sensorless and sensorless implementations of traditional V-AO are discussed, highlighting how polarisation sensing or metric-based optimisation can drive the correction architecture. In addition, O-AO is briefly introduced as an advanced V-AO viewpoint that achieves vectorial correction by synthesising an explementary object to cancel the sample-induced aberration, with its architecture and experimental validation developed in Chapter 4. Together these sections provide a coherent basis for the experimental and methodological developments presented in the following chapters.

Chapter 3 V-AO for advanced polarimetric imaging system

Chapter statement:

This chapter is based on the following publication: Vectorial adaptive optics for advanced imaging systems. *Journal of Optics* 26, 065402 (2024). The content has been adapted and extended for the purpose of this thesis.

3.1 V-AO implementation in imaging system

Building on the framework established in Chapter 2, this chapter describes the implementation of vectorial adaptive optics (V-AO) in a wide-field Stokes polarimetric microscope and evaluates its performance in the imaging domain.

3.1.1 Vectorial aberration

As outlined in Chapter 2, optical aberrations are not limited to phase errors. As we focus on wide-field imaging here for proof-of-concept demonstration, residual phase aberrations in such systems are relatively small. Consequently, the emphasis is placed on polarisation aberrations and their correction strategies. As sketched in Fig. 3.1, phase, polarisation, and intensity components (throughout this thesis, intensity errors such as non-uniform distribution and energy loss are referred to intensity aberrations) can jointly degrade performance[29,94,95]. In particular, polarisation aberrations – arising, for example, from oblique incidence on birefringent elements, Fresnel effects at interfaces, or interactions with complex biological/media materials[96,97] – distort the state of polarisation (SoP). The resulting SoP errors impair interference at the focus and thus reduce resolution, and they also bias polarisation-sensitive measurements such as Stokes/Mueller microscopy.

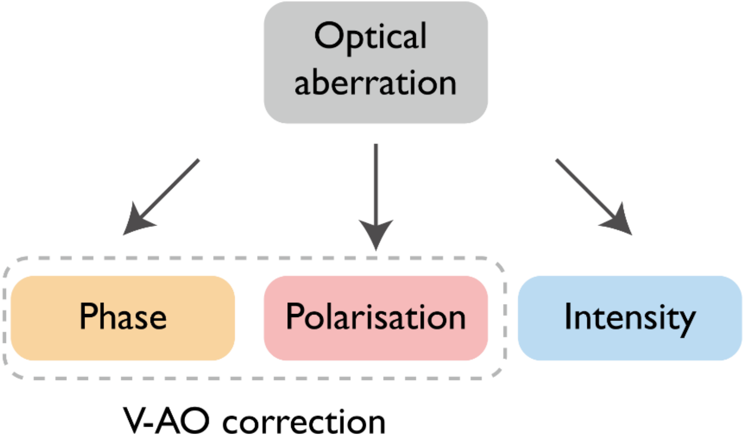

Figure 3.1: Optical aberrations. Generally, optical aberrations can be broadly categorised into three types: phase, polarisation, and intensity aberration. These components often degrade the performance of an optical system jointly.

3.1.2 Vectorial aberration correction strategy

As described in Chapter 2, V-AO can operate in either sensor-based or sensor-less configurations. In this chapter, a sensor-less correction strategy is adopted, using the pupil intensity as a feedback signal to guide aberration compensation. A fixed polariser is placed after the V-AO module, with its transmission axis aligned to the desired output SoP. In this arrangement, vectorial aberrations are converted into an intensity signal, allowing intensity to serve as a metric for optimisation.

Fig. 3.2 depicts a V-AO correction system where the V-AO module consists of SLMs to achieve pixelated control of the SoPs and a DM to compensate for initial system phase aberrations, which will remain unchanged throughout the rest of the experiments. Intensity measured after the polariser serves as the feedback signal: when the corrected SoP matches the desired target SoP, the transmitted intensity reaches its maximum. By optimising the SLM patterns to maximise this metric, the system converges toward a spatially uniform output SoP field.

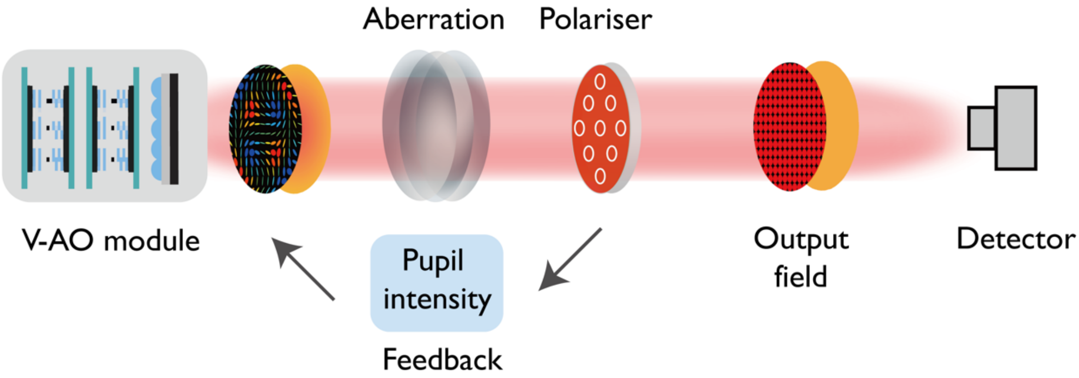

Figure 3.2: V-AO correction strategy. A fixed polariser with its transmissive axis aligns well with the desired SoP filters the pupil intensity and provides feedback to the V-AO module for aberration compensation.

In this chapter, the cutting-edge V-AO demonstration for wide-field imaging is presented. First, polarisation aberration correction for Stokes polarimetric imaging is conducted, and two important criteria – vectorial information precision and vectorial uniformity – are introduced to evaluate the correction ability of V-AO system. A high-quality, spatially uniform vectorial field is then achieved and analysed based on these criteria. The V-AO correction is performed on three different samples associated with polarisation aberration: 1) air; 2) a polarisation calibration sample; 3) a birefringent crystal sample. A set of results before and after V-AO correction is presented for each sample to demonstrate the effectiveness of our V-AO method in correcting for aberrations in wide-field imaging systems.

3.1.3 V-AO correction experimental setup

The V-AO strategy was implemented in a wide-field Stokes polarimeter, with the optical layout is shown in Fig. 3.3. A He-Ne laser (Melles Griot, 05-LHP-171, 632.8 nm) served as the light source. After beam expansion, the illumination beam was reflected by the first SLM (SLM1; Hamamatsu, X10468-01), passed through a half-wave plate (Thorlabs, WPH10M-633), and reflected by the second SLM (SLM2; Hamamatsu, X10468-01) and then directed onto a DM (Boston Micromachines Corporation, Multi-3.5). A 50:50 non-polarising beam splitter (Thorlabs BS010) divided the beam into two paths.

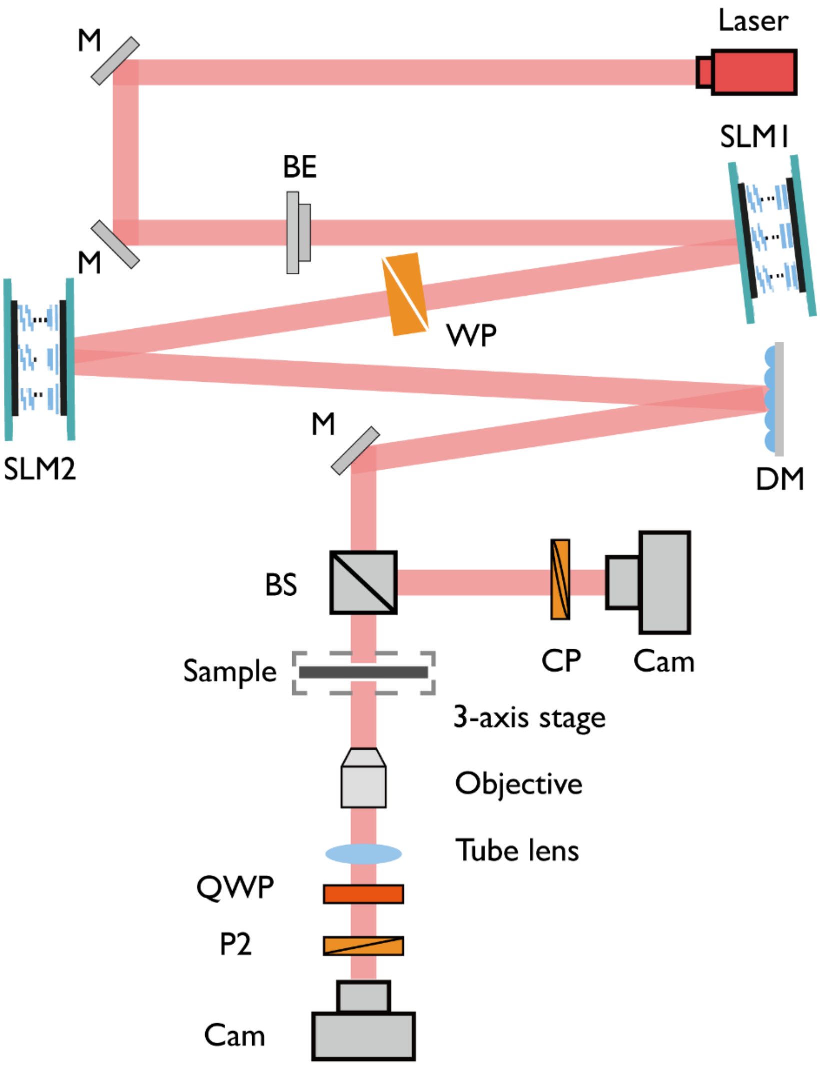

Figure 3.3: A schematic of the experimental setup. M: mirror, BE: beam expander, SLM: liquid-crystal-on-silicon spatial light modulators (Hamamatsu X10468-01, 800 × 600 pixels), WP: half-wave plate, QWP: quarter-wave plate, DM: deformable mirror (Boston Micromachines Multi-3.5, 140 actuators), BS: 50:50 non-polarising beam splitter (Thorlabs BS016), CP: circular polariser, P: linear polariser. Objective: Olympus PLN 4x objective, NA=0.1 (FOV=1.488 mm × 1.190 mm), Cam: camera (Thorlabs DCC3240N). The majority of 4F systems are omitted for clarity.

In the reflection arm, the beam traversed a circular polariser composed of a horizontal linear polariser (Thorlabs GL10-A) and a quarter-wave plate set at 45° (Thorlabs WPQ10M-633). A camera (Thorlabs, DCC3240N) was placed after the equivalent circular polariser to capture intensity images to furnish feedback for V-AO optimisation. The transmission path acts as the illumination source for the sample, the movement of which is controlled by a three-axis translation stage (Thorlabs, RBL13D). A PSA is adopted to measure the output Stokes vector, which consists of a quarter-waveplate (Thorlabs, WPQ10M-633) mounted into a motorised rotation stage (Thorlabs, PRM1/MZ8) and a linear polariser (Thorlabs, GL10-A) with its transmissive axis oriented in the horizontal direction. The resulting images are recorded by a second camera (Thorlabs, DCC3240N).

3.1.4 Theoretical framework of V-AO correction

The V-AO SoP corrector consists of two SLMs (the first oriented at 0° and the second at 45°), enabling pixelwise generation of arbitrary, spatially varying SoPs[92,98,99]. The Jones vectors $\boldsymbol{j}_{out}$ after SoP corrector can be represented as:

$$\boldsymbol{j}_{out} = e^{i\frac{\theta_1+\theta_2}{2}} \cdot \mathrm{SU2}(\boldsymbol{H},\pi)\mathrm{SU2}(\boldsymbol{H},\theta_2) \cdot \mathrm{SU2}(\boldsymbol{W},\pi) \cdot \mathrm{SU2}(\boldsymbol{H},\pi)\mathrm{SU2}(\boldsymbol{H},\theta_1) \cdot \boldsymbol{j}_{in} \quad (3.1)$$

where $\boldsymbol{j}_{in}$ represents the incident light with its corresponding SoP represented by normalised Stokes vectors as $\boldsymbol{S_{in}} = [S_{in_1}; S_{in_2}; S_{in_3}]$; $\boldsymbol{j}_{out}$ represents the outcome light with its corresponding Stokes vectors $\boldsymbol{S_{out}} = [S_{out_1}; S_{out_2}; S_{out_3}]$;

SU2 denotes the special unitary group of degree 2; $\boldsymbol{H} = [1; 0; 0]$ and $\boldsymbol{W} = [1; -1; 0]/\sqrt{2}$ represent rotation axes in the Poincaré sphere (PS); and θ_1 and θ_2 denote the retardances applied on two SLMs. The transformation from $\boldsymbol{S_{in}}$ to $\boldsymbol{S_{out}}$ can be achieved when:

$$\begin{cases} \theta_1 = \arccos S_{out_1} - \arccos S_{in_1} \\ \theta_2 = \operatorname{arctan2}(-S_{out_2}, S_{out_3}) - \operatorname{arctan2}(-S_{in_2}, S_{in_3}) \end{cases} \tag{3.2}$$

As a result, the corrector is able to transform incident SoP into desired output SoP, by applying corresponding pixel values p_1, p_2 onto two SLMs, resulting in desired retardance $\theta_1 = f(p_1)$ and $\theta_2 = \mathrm{g}(p_2)$.

Traditionally, each SLM pixel should be calibrated to obtain the precise relation (f and g) between retardance value and applied voltage[92]. The present strategy circumvents this calibration by directly optimising the pixel values that maximise the pupil intensity. At the heart of this correction method is to find the best pixel values p_1, p_2 for every point in the pupil, where p_1, p_2 represent values applied to each of the two SLMs, respectively, resulting in the desired retardance θ_1 and θ_2.

Consider an arbitrary point at the pupil plane of the analysing channel (note in principle, any type of analysing component can be inserted in this channel with careful design to guide the V-AO corrector in displaying the optimal pre-compensation SoP), when the pixel values p_1, p_2 change on the SLMs, the resulting intensity will change as a function of p_1, p_2 and reach the highest value once the generated SoP matches the targeted SoP determined by the circular polariser before the camera. Now the problem of correcting the SoP has been converted from finding the correct SLM retardance values to directly finding the best pixel values p_1, p_2 on the SLMs which result in the maximum intensity after the analyser placed at the pupil plane. The following procedures are adopted to find the best pixel values p_1, p_2 for every point in the pupil.

1) **Coarse scan set-up.** The initial information required to start the correction is the pixel value boundary for each SLM, $p_1 \in [l_1, h_1]$ and $p_2 \in [l_2, h_2]$, where p_i represents the value to be applied to each pixel on the SLM, and l_i and h_i are the lower and upper boundaries for each SLM. No explicit relationship between the pixel value and SLM retardance is required at this stage. The procedure starts with the derivation of a group of coarse scan values that take all possible ordered pairs from two fixed length integer arrays, the first extracted from the pixel value boundary of SLM1 and the second from that of SLM2, which is also the Cartesian product of these two arrays $[l_1, a, b, \cdots, h_1] \times [l_2, d, e, \cdots, h_2]$. Specifically, the pupil was sampled on a coarse 11×11 grid and then reconstructed using cubic-spline interpolation, which has been shown to capture low-spatial-frequency aberrations accurately[12].

2) **Intensity acquisition.** For each pair of coarse scan values (p_1, p_2), p_1 is applied to all the pixels of SLM1 and p_2 to SLM2. Then the corresponding pupil intensity image is captured. The above steps are then repeated until an intensity image is captured for all coarse scan value pairs.

3) **Interpolation and refinement.** Next, the corresponding pupil intensity against p_1 and p_2 is plotted for each pupil coordinate. By interpolating for remaining pixel values within the boundaries, the optimal values p_1, p_2 for each pupil pixel can then be derived by locating the maximum value in the interpolation result. In these experiments, the pixel arrays used for the coarse scan process are $p_1 \in [8, 28, 48, \cdots, 128, 148]$ and $p_2 \in [44, 60, 76, \cdots, 140, 156]$. Both arrays take 8 steps to maintain a uniform interpolation region. It is noted that the SLM patterns calculated from the captured image may not be directly applicable to the two SLMs, as the number of pixels on the SLM may not be identical to that covered by the light beam on the camera. However, this can be easily overcome by performing another interpolation to map the calculated pattern back to the size of the SLM.

3.2 Experimental results and analysis

3.2.1 Evaluation criteria

Two important criteria, vectorial precision (*P*) and vectorial uniformity (*U*), were introduced to evaluate the performance of the correction procedure.

3.2.1.1 Vectorial precision

The vector difference *D* on PS between the target SoP and the experimentally obtained SoP is defined as:

$$D = c_p \left\| S - \tilde{S} \right\| \tag{3.3}$$

where the target SoP is defined as $S = [S_1, S_2, S_3]$ and actual SoP defined as $\tilde{S} = [\tilde{S}_1, \tilde{S}_2, \tilde{S}_3]$, both of them are normalised and all parameters are within the range of $[-1, 1]$. $\left\| S - \tilde{S} \right\|$ denotes the Euclidean norm here. c_p is a constant normalisation factor chosen to ensure that *D* falls within the range of [0, 1]. As the norm of the SoP vector difference $\left\| S - \tilde{S} \right\|$ is in the range of [0, 2], thus $c_p = \frac{1}{2}$ is used.

We then define the precision metric *P*:

$$P = 1 - D \tag{3.4}$$

such that *P* = 1 signifies perfect matching between the target and actual SoP, while *P* = 0 represents the maximum mismatch on the PS. Note that this evaluation metric is valid over a line, a region of interest, or the whole pupil area.

3.2.1.2 Vectorial uniformity

The uniformity difference U_D is defined as the standard deviation of the actual SoP ($\tilde{S}$) from the mean SoP ($\bar{S}$) across the whole region of interest:

$$U_D = c_u \sqrt{\overline{\left\| \tilde{S} - \bar{S} \right\|^2}} \tag{3.5}$$

where c_u is a constant normalisation factor set to 1 to ensure U_D falls within the range of $[0, 1]$. A smaller U_D represents a more uniform distribution. Each parameter $\bar{S} = [\bar{S}_1, \bar{S}_2, \bar{S}_3]$ is defined as the mean of parameters $\tilde{S} = [\tilde{S}_1, \tilde{S}_2, \tilde{S}_3]$ across the whole pupil, as expressed below:

$$\bar{S}_i = \bar{\tilde{S}}_i \tag{3.6}$$

Therefore, the vectorial uniformity metric U is defined so that larger values of U indicate more uniform SoP distribution.

$$U = 1 - U_D \tag{3.7}$$

Note that this evaluation metric is valid over the whole imaging pupil or sub-regions. Hence, this metric can be used to evaluate global uniformity.

3.2.2 Polarisation aberration correction results

3.2.2.1 Systematic aberration correction

After the two evaluation metrics had been defined, the systematic aberration correction procedure was carried out with V-AO. Fig. 3.4 illustrates the Stokes vector field of the pupil along with their Stokes parameters before and after the correction process. From the sub-figures, it can be observed that the uncorrected pupil shows SoPs that are both inaccurate and non-uniform relative to the target, while the V-AO approach can provide an excellent correction resulting in a uniform targeted SoP profile across the whole pupil area.

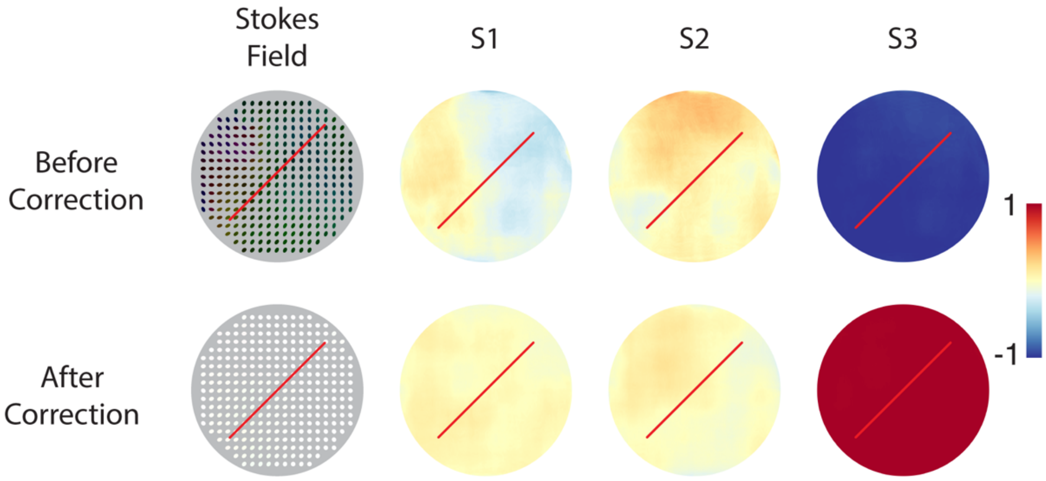

Figure 3.4: Stokes vector field before and after V-AO correction. Stokes vector fields and individual Stokes parameters before and after V-AO correction.

Then a quantitative assessment was performed along a randomly chosen cross-section, as shown in Fig. 3.5. It can be found that, despite the significant distortion in S_3, high-quality Stokes-vector restoration was achieved. A further evaluation of the correction performance was carried out using the parameters P and U, plotted in Fig. 3.5. As illustrated by the pink and red lines, the vectorial precision increased dramatically from below 1% to over 95%, highlighting the effectiveness of V-AO method in recovering accurate polarisation information. Meanwhile, the uniformity of the Stokes vector field is also boosted from 77.1% to 91.2%. These results validate that V-AO correction process can effectively compensate for spatially varying polarisation aberrations in the imaging domain.

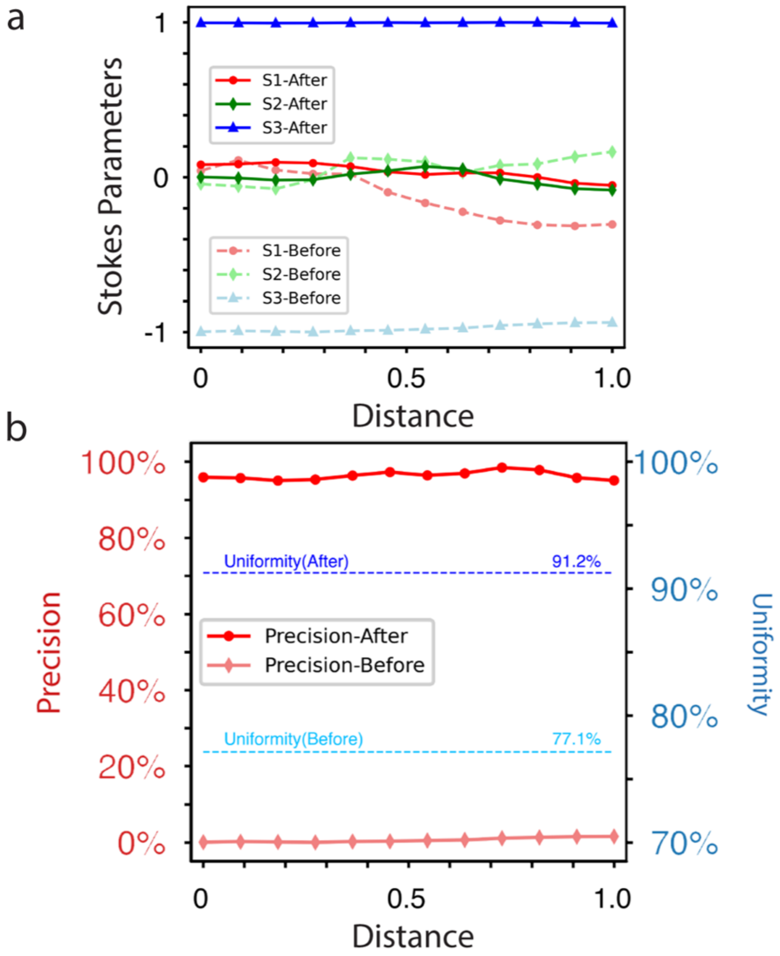

Figure 3.5: Stokes vector field analysis before and after V-AO correction. (a) The variation of each Stokes parameter before and after correction along the red line in Fig. 3.4. (b) The values of *P* (vectorial precision) and *U* (vectorial uniformity) were calculated along the same line before and after correction.

3.2.2.2 Practical polarisation aberration correction

The effectiveness of the proposed V-AO method is further demonstrated in practical scenarios. Experiments were conducted on three representative samples: a) air; b) a polarisation calibration sample; and c) a birefringent crystal sample, as shown in Fig. 3.6. For the latter two samples, a standard quarter-wave plate was used as the calibration target, and a thin film of uniaxial positive crystal sample featuring different retardance and fast axis orientation distributions as the birefringent sample. The columns represent the sample schematic (column 1), and the Stokes vector (large pattern) and intensity (small pattern) fields corresponding to the target SoP under the following conditions: ground truth (column 2), aberrations present with V-AO off (column 3), and aberrations present with V-AO on (column 4).

For the air sample, the ground truth suggests a uniform circular SoP and a bright intensity distribution. A comparison between the V-AO off and on conditions reveals enhanced vectorial precision, spatial uniformity, and pupil intensity following correction.

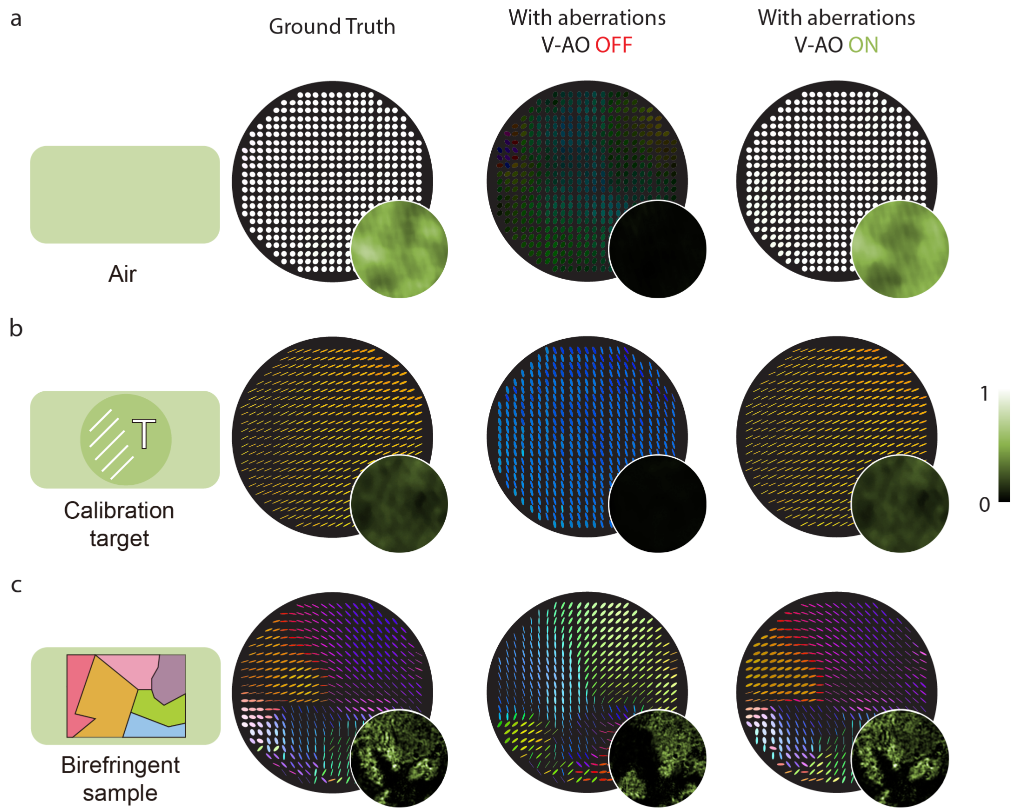

Figure 3.6: V-AO correction for aberrated imaging systems. Stokes vector field images and intensity images of three different representative samples: (a) air, (b) a calibration target sample, and (c) a birefringent sample. For each sample, three conditions are illustrated: ground truth, aberration present with V-AO off, and aberration present with V-AO on. In each panel, the large circles show the reconstructed Stokes-vector field (SoP map), while the small circles show the corresponding intensity image under the same analyser setting.

In (a), as the sample is air, the expected SoP and intensity distributions should match the input beam. The results show that the uniform circular SoP and high intensity level are successfully restored when V-AO is applied. In (b), the calibration target (QWP) introduces a linear polarisation transformation, and the resulting Stokes vector field and intensity map (measured under the same analyser condition) change accordingly. In (c), a birefringent sample with spatially varying retardance and fast axis orientation is tested. With V-AO on, the spatially varying SoP and intensity agree well with the ground truth. The global correction precision, calculated by comparing the imaging errors between the corrected and ground truth images, is quantified as follows: 1) for air, 95.84%; 2) for the calibration target, 95.02%; 3) for the birefringent sample, 95.86%. These results confirm the effectiveness of the V-AO method in compensating vectorial aberrations across a range of sample conditions.

It should be noted that:

1) the ground truth was acquired using a conventional low-resolution Stokes vector microscope, where system induced aberrations such as Fresnel's effects – typically introduced by high numerical aperture lenses [100,101] can be neglected. The experimental wide-field setup in this work employs an objective lens with a low numerical aperture (NA = 0.1), ensuring that system-induced polarisation aberrations remain negligible.

2) the original intensity is not perfectly uniform, which happens in traditional wide-field imaging. It can be compensated via beam shaping or further adaptive correction techniques.

3) the displayed intensity images were captured using circular SoP illumination and right-hand elliptical SoP analysis only, implemented by orienting the QWP at 128.3° and the polariser at 0°, respectively, as an example.

For the latter two cases, the corrected results closely resemble the ground truth, validating the V-AO system's correction capability. In particular, for the case of the birefringent sample, structural features become more apparent in the corrected vectorial and intensity images, further highlighting the potential of the V-AO approach for revealing spatially varying vectorial contrast.

3.3 Summary and discussion

In this work, V-AO has been validated through a widely adopted polarisation-sensitive Stokes vector microscope system. Two key criteria – vectorial precision *P* and uniformity *U* have been introduced to quantitatively assess the correction performance of the V-AO method. Using these metrics, a vectorial precision exceeding 95% and a uniformity greater than 91% have been demonstrated, confirming the effectiveness of the correction process.

This method paves the way for various AO-targeted imaging scenarios including super-resolution imaging and vectorial imaging. For wide-field super-resolution imaging methods, not only both phase and polarisation perturbations in the structured illumination light path can be corrected, but also new V-AO strategies for the detection path has been competently designed. For traditional vectorial imaging methods such as Stokes vector/Mueller matrix imaging suffering from spatially varying aberrations, e.g., those induced by high numerical aperture objective lenses or the specimens themselves, V-AO has now been taken a step further to enable novel V-AO enhanced vectorial imaging methodologies, with the expectation to benefit various fields such as biomedical and clinical characterisation and astronomical observations.

Chapter 4 Object-wise adaptive optics adopting a tuneable arbitrary retarder array

Chapter statement:

This chapter is based on the following publication: A reconfigurable arbitrary retarder array as complex structured matter. *Nat Commun* **16**, 4902 (2025). The content has been adapted and extended for the purpose of this thesis.

4.1 Concept

4.1.1 Object-wise adaptive optics (O-AO)

Chapter 3 established a V-AO architecture for compensating retardance aberration in polarimetric imaging, in which two SLMs restored a uniform state of polarisation (SoP) using pupil-intensity feedback. While it is effective for pre-compensating a fixed target SoP, the arrangement does not realise arbitrary-to-arbitrary transformations of SoP or phase across the pupil, which is essential for key applications such as aberration correction in the detection pathway[102–104]. Additionally, it is unable to eliminate the complex field conversion process required for sensor-less correction procedures[103].

To address these limitations, an object-wise adaptive optics (O-AO) corrector is introduced. The core idea is to compensate vectorial error from the object's perspective by synthesising, at or near the object plane, a spatially varying medium whose Jones matrix (or Mueller matrix) is the explement (i.e., inverse) of the measured aberration. In other words, an explementary polarisation-aberrated layer is formed so that the cascade “sample + corrector” becomes polarisation-insensitive (for instance, a retarder with 2kπ radians retardance value, which has no impact on the SoP).

Practically, this is achieved with a tuneable arbitrary retarder array**:** four cascaded modulators (e.g. SLMs) are encoded so that each virtual pixel behaves as an elliptical retarder with independently adjustable axis geometry, retardance, and induced phase. This enables true arbitrary SoP and phase conversion, allows the corrector to be placed anywhere in the system—including the detection arm—and removes the need for the external field-conversion step used by conventional sensor-less schemes. The following sections present the experimental realisation of this array and its use in both sensor-based and sensor-less O-AO.

4.1.2 Arbitrary retarder array

Tuneable linear retarder arrays, such as SLMs, have a long history, the earliest of which can be traced back to Hamamatsu in the 1980s. There are many ways of realising beam modulators based on tuneable linear retarder arrays[105–112], with the dynamic control of metasurfaces[113] being a particularly promising one. While the linear retarder-based devices offer tuneability for phase and polarisation control, their use of linear retardation limits the controllable degrees of freedom for manipulating light[105–112], elliptical retarder devices can do arbitrary retardation, but suffer from lack of tuneability. A tuneable arbitrary retarder array could address both challenges simultaneously and has been proposed theoretically[98,114,115].

Here, for the first time, a tuneable arbitrary retarder array was achieved (see Fig. 4.1(a)) via virtual pixels with full control over all degrees of freedom by cascading a series of low functionality devices (see Fig. 4.1(b)), implemented in this work as three SLMs and a DM. It shows that cascade of elements with judicious encoding can mimic a pixel-controllable arbitrary retarder of any axis geometry, retardance value, and induced phase, simultaneously. This allows us to demonstrate that by using the array's direct polarisation aberration compensation capability as a vectorial adaptive corrector, the spatially varying arbitrary retardance aberrations can be dynamically corrected. This approach, employing novel adaptive optics methods, is validated through focus correction in a complex aberrated system.

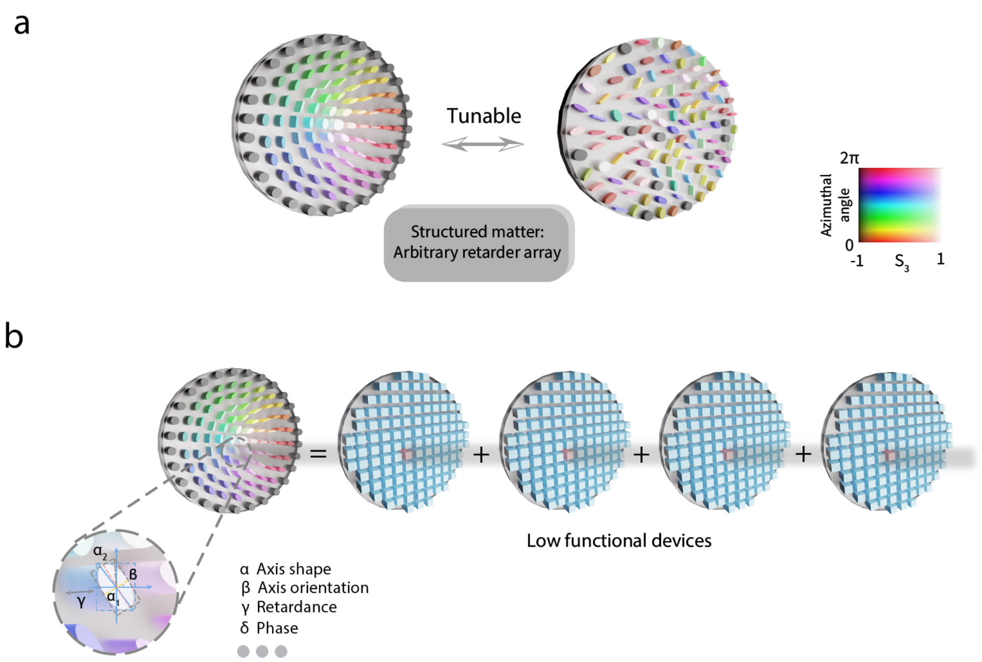

Figure 4.1: Tuneable arbitrary retarder array. (a) A schematic of a tuneable elliptical (arbitrary) retarder array. The shape and colour of each pillar indicate different retarder axis geometries, while the pillar height corresponds to its retardance value. A vector representation (like the Stokes vector using S_1, S_2, and S_3) is used to describe the axis geometry. For visualisation, hue is used to represent the azimuthal angle $\tan\theta = \frac{S_2}{S_1}$ and lightness to indicate the magnitude of S_3, similar to Ref[116,117]. (b) A tuneable arbitrary retarder array-based device can be formed via reconfigurable pixels, allowing control over axis geometry α (α_1 and α_2 denote the semi-major and semi-minor axes of the ellipse), orientation β, retardance value γ, and induced phase δ, allowing its functionality to be switched on demand. Through this work, the construction of the device is achieved by four cascading low-functionality devices such as SLMs and DM.

4.2 O-AO aberration correction

The configuration of the focusing system for proof-of-concept demonstration is shown in Fig. 4.2, where the O-AO corrector enables validation of sensor-based method through a Mueller matrix polarimeter and sensor-less method via focal spot images.

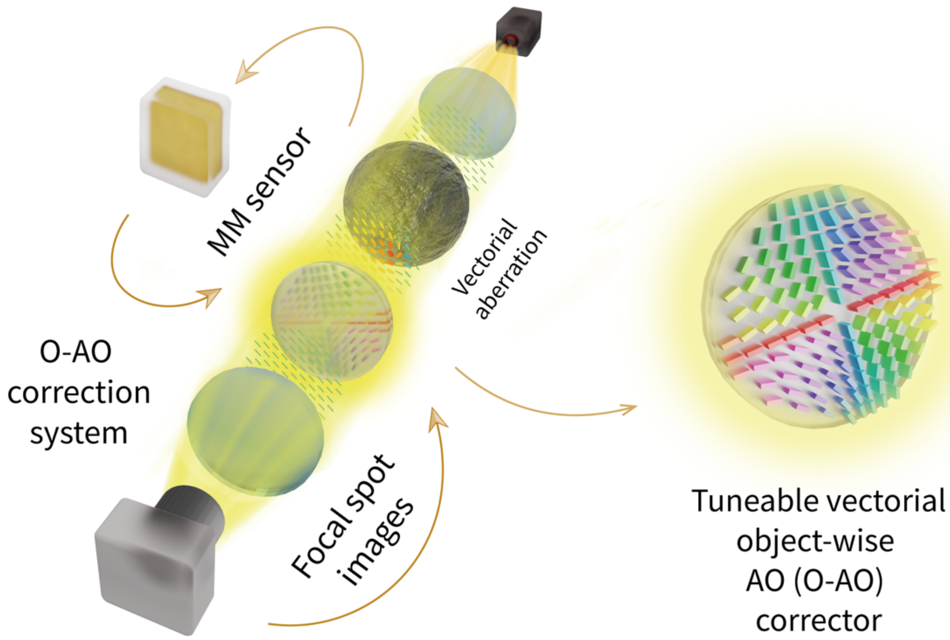

Figure. 4.2: O-AO correction using the arbitrary retarder array. An optical focusing system with induced aberrations, utilising the O-AO corrector to validate sensor-based (through a Mueller matrix polarimeter) and sensor-less (through focal spot images) methods.

4.2.1 Sensor-based method

This method contains two core parts. The first part is the initial calibration and characterisation of the SLMs, whose dynamic range will need to be measured and used in the following experiments. A LUT will be generated after the calibration, preparing for the correction process. The second part is to use the Mueller matrix polarimeter to directly measure the polarisation aberration introduced by an external target in a pixelated way. The phase patterns on the SLMs will be adjusted based on the LUT to compensate for the measured polarisation aberration. The residual phase aberration will then be corrected by the DM.

4.2.1.1 Initial calibration of SLM

To generate the LUT for the SLMs modulation, the following steps are taken. Initially, the source laser intensity is adjusted using a neutral-density (ND) filter, and the exposure time of the CCD camera is carefully chosen to ensure the calibration data will use the full dynamic range of the CCD camera. These parameters are fixed throughout the experiment. Each SLM pixel has an 8-bit modulation depth, with flat grayscale values F_i ranging from 0 to 255 ($F_i \in [0,255], F_i \in \mathbb{Z}$), where “flat” denotes a spatially uniform frame used to compensate pixel-wise phase offsets caused by liquid-crystal nonuniformity. Each flat value F_i is applied across the SLM so that the per-pixel phase offsets can later be equalised into a zero phase (“flat map”), and the corresponding intensity images are captured. Because the size of the captured image is larger than the pattern that is loaded onto the SLM, the image will then be resized to fit the number of pixels on the SLM using the bicubic method. Thus, the corresponding intensities with all N pixels assigned with the flat value F_i will be derived and converted back to the phase introduced as $[P_{i1}, P_{i2}, \dots, P_{iN}]$, where P_{iN} stands for the corresponding phase value of *n*th pixel applied flat value F_i. This process is iterated for all grayscale values F_i, resulting in a dynamic range of phase values $[P_{0n}, P_{1n}, \dots, P_{255n}]$ for each pixel. The result is then unwrapped based on the minimum phase value S_n and the maximum phase value L_n at the corresponding flat value F_S and F_L. After these processes, the resulting linear mapping between input flat values F_{in} and the output phase values P_{out} is saved into the LUT for each SLM for further utilisation.

4.2.1.2 Aberration correction process

The correction process is as follows:

1) All SLMs in the system are flattened (using the LUT generated before to have a uniform phase profile), and images of the SLM surface and the focal intensity distribution (FID) of the system are recorded as references.

2) Conventional DM-based sensor-less correction process (as mentioned in section 2.3.2.2) is executed to compensate the system's phase aberration. A standard focal Airy disk shape will be recorded to indicate that the system has been calibrated.

3) An external vectorial aberration is introduced into the system. By utilising Mueller matrix polarimetry, the polarisation aberration D introduced by the external sample can be quantitatively obtained without any iterations.

4) The explementary value of the polarisation aberration valued as $2\pi - D$ will be decomposed into three individual modes D_1, D_2, D_3. These modes will be applied to the three SLMs to form an “complementary elliptical retarder” to compensate for the aberration.

5) After the O-AO sensor-based method, a conventional sensor-less phase correction is followed to further improve the FID quality.

The related flow chart is shown in Fig. 4.3.

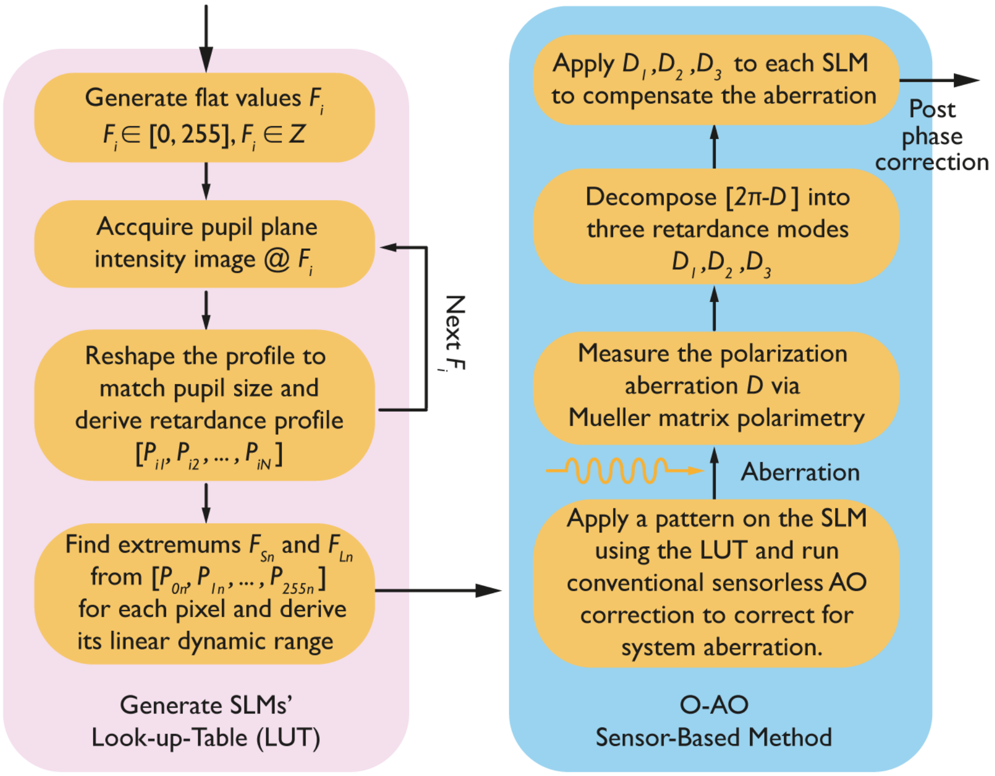

Figure 4.3: Sensor-based O-AO correction flowchart. The left side outlines the initial SLM calibration process for LUT generation, while the right side details the steps for implementing the sensor-based O-AO correction.

The sensor-based O-AO correction results are shown here. The measured Mueller matrix for aberration, the compensation patterns on four devices (i.e., the corrector), as well as a cross-section comparison of the focal spots (O-AO off vs. on) are shown in Fig. 4.4 to validate the improvement.

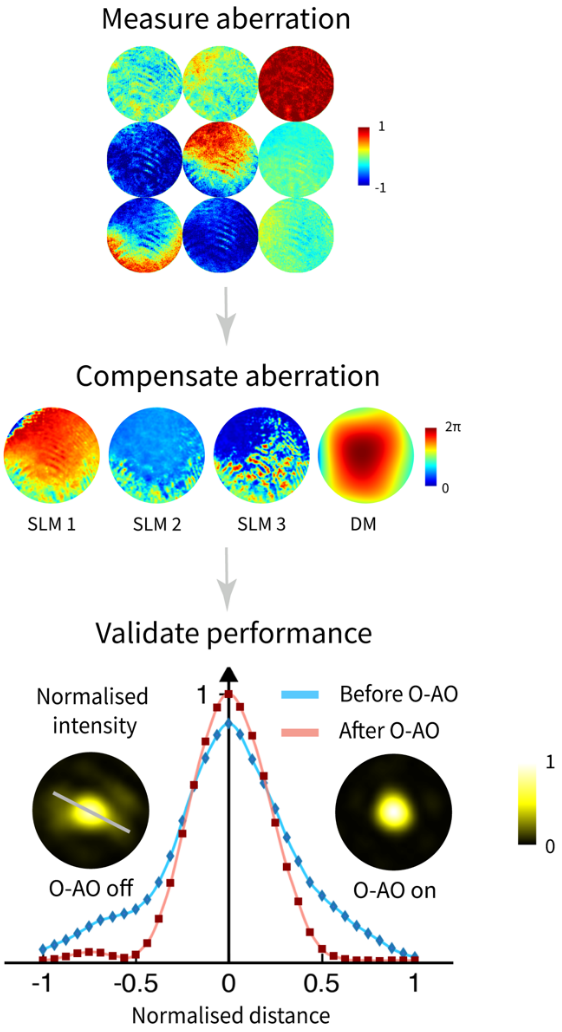

Figure 4.4: Sensor-based O-AO correction results. Measured Mueller matrix of the aberration, phase patterns on all four devices after O-AO correction, foci profiles as well as sampled focal spot cross-sections (white line on the focal spot image) before and after correction are presented. The vectorial aberration is a tilted waveplate array[103]. Y-axis in the line chart represents the normalized intensity value and x-axis represents the distance of the sampled curve on the focal spot.

The measured Mueller matrix confirms that the aberrating element produces a spatially varying polarisation transformation across the field. The three SLM patterns are then used to synthesise the complementary retarder response, while the DM removes the remaining scalar phase term. After applying the correction, the focal spot becomes more symmetric and approaches the calibrated Airy pattern. This improvement is also clear in the line profiles, where the central peak increases and the main lobe becomes narrower, indicating that the dominant vectorial error has been largely cancelled.

4.2.2 Sensor-less method

The core idea of this sensor-less method is to iteratively apply a group of designed retardance patterns onto SLMs to compensate for the vectorial aberration. Here, only the FID images will be captured and a selection of designed patterns for O-AO correction will be scanned across a given pattern coefficient range to obtain the optimal pattern for aberration correction. The SLMs are assumed to be calibrated as described in the previous section.

4.2.2.1 Retardance mode

A newly defined set of object-specific modes (which are termed vectorial retardance modes (see Fig. 4.5) are applied to estimate polarisation aberration. The modes utilised in this method have controllable parameters similar to standard Zernike modes, with the exception that the phase values are replaced by the retardance values. The real-valued retardance aberration function δ (ρ, θ), which is defined over the unit disk, is given by:

$$\delta(\rho,\theta) = \sum_{n,m} a_n^m Z_n^m(\rho,\theta) \tag{4.1}$$

where the definition of n and m follows the one given by Zernike and Noll. $a_n^m \in \mathbb{R}$ are the coefficients of the real-valued Zernike polynomials Z_n^m, which are defined by:

$$Z_n^m(\rho,\theta) = c_n^m R_n^{|m|}(\rho)\Theta_n^m(\theta) \tag{4.2}$$

where

$$c_n^m = \begin{cases} \sqrt{n+1} & m = 0 \\ \sqrt{2(n+1)} & m \neq 0 \end{cases} \tag{4.3}$$

$$R_n^{|m|}(\rho) = \sum_{s=0}^{\frac{n-|m|}{2}} \frac{(-1)^s (n-s)!}{s!\left[\frac{n+|m|}{2}-s\right]!\left[\frac{n-|m|}{2}-s\right]!} r^{n-2s} \tag{4.4}$$

$$\Theta_n^m(\theta) = \begin{cases} \cos(m\theta) & m \geq 0 \\ -\sin(m\theta) & m < 0 \end{cases} \tag{4.5}$$

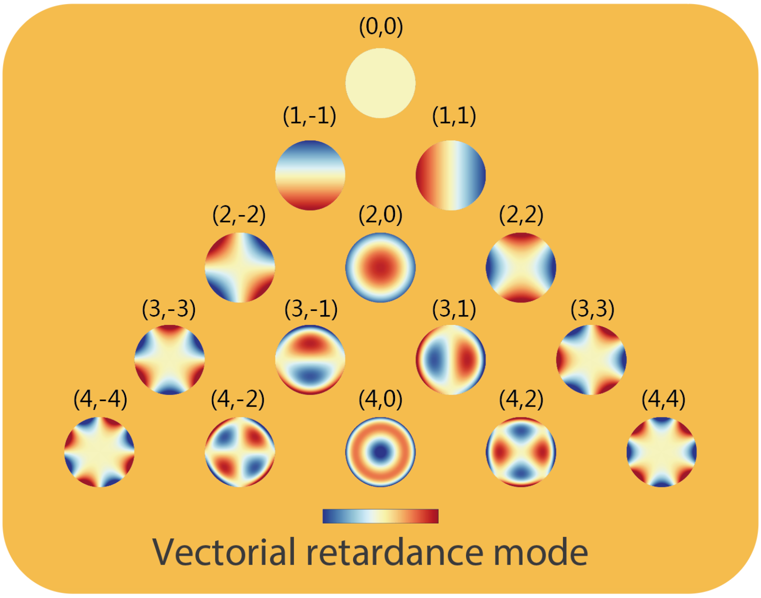

Figure 4.5: Vectorial retardance modes. The first 15 vectorial retardance Zernike modes are designed within a range of [−π, π]. These patterns are arranged following Noll's indexing convention.

4.2.2.2 Aberration correction process

For the correction process:

1) All SLMs in the system were initially flattened and images of the system FID are captured as reference. Then the same calibration process described in the previous section was conducted.

2) Different retardance modes were applied to the arbitrary retarder array. These modes were used to manipulate the retardance distribution on the array in a pixelated manner with varying parameters, and focal spot images were recorded

sequentially. The recorded images provided information that allowed for the estimation of retardance aberrations.

3) The estimated aberrations were used to drive the array to correct the aberration. The related flow chart is shown in Fig. 4.6.

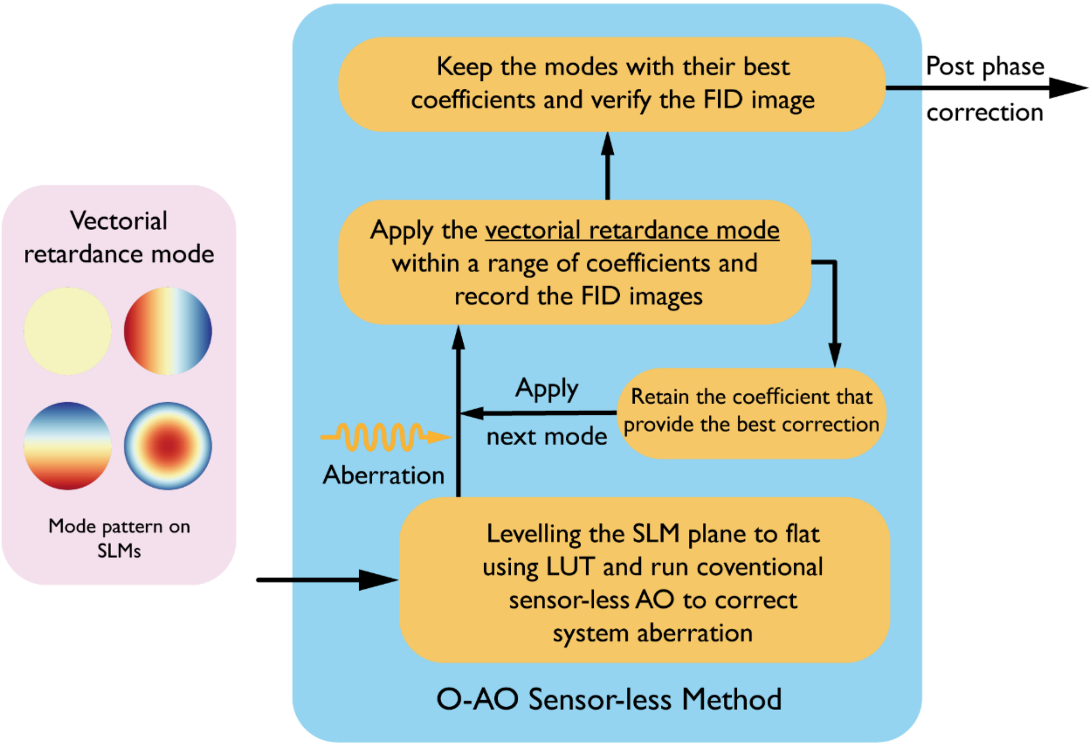

Figure 4.6: Sensor-less O-AO correction flowchart. The main sensor-less O-AO loop utilizing the designed vectorial retardance modes is demonstrated.

The sensor-less O-AO correction results are shown here. Figure 4.7 presents phase pattern and focal spot analyses akin to those described in the sensor-based section, with the addition of a fitted curve for a retardance mode – piston, which is usually neglected in traditional AO. Note in this case, the piston mode represents the object's retardance value, which alters the overall retarder performance and, in turn, affects the focal spot. It is evident that the O-AO successfully recovered the focal spot.

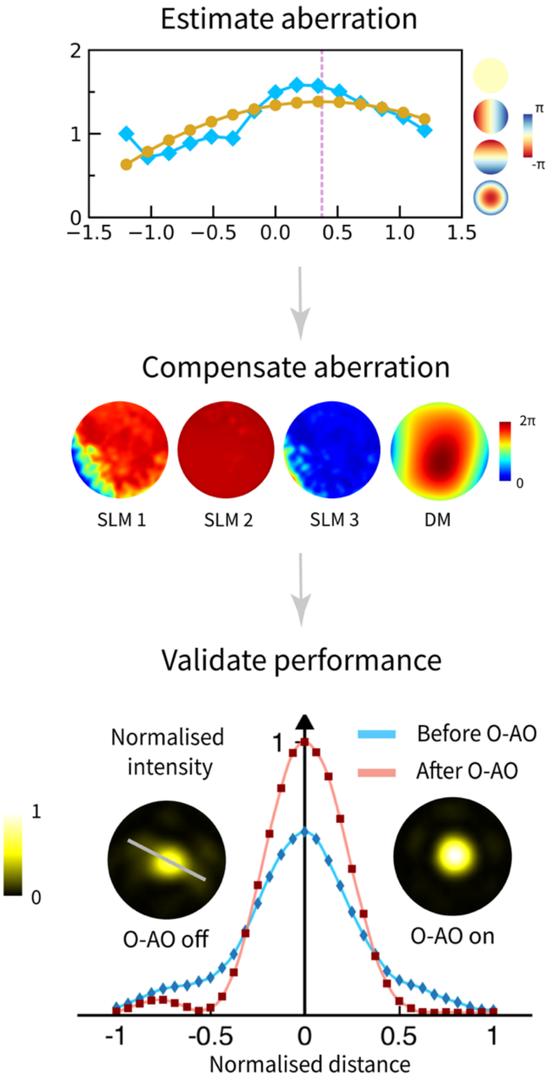

Figure 4.7: Sensor-less O-AO correction results. Results for sensor-less O-AO off vs. on for the same retardance aberration in sensor-based experiment. A fitted curve for retardance piston mode is given as an example for aberration estimation. Phase patterns on all four devices after O-AO correction, foci profiles as well as sampled focal spot cross-sections before and after correction are also presented.

The example fit in Fig. 4.7 shows that a retardance piston term can also be retrieved. This is important because, although a piston term does not change the wavefront phase, it changes the effective retarder response and can therefore distort the focal spot. After correction, the intensity is re-concentrated into the central lobe and the spot shape becomes closer to the calibrated reference, demonstrating that O-AO can operate without a polarimetric sensor, at the cost of additional measurements and a model-based estimation step.

It is worth noting that the correction accuracy may be reduced when the deviation is complex or exceeds the available mode range, leading to slower convergence and increased iterations. Additionally, the correction quality may degrade under strong superposition of mode patterns due to the SLM pixel resolution, particularly for large deviations or high-frequency aberrations. However, these limitations are highly likely to be mitigated by refining the calibration process for mode superposition with more modes using higher-resolution SLMs. Furthermore, expanding the mode range with enhanced learning-based correction algorithms could further enhance accuracy and efficiency.

4.3 Summary and discussion

This chapter has presented the first experimental realisation of O-AO, a concept that extends vectorial AO from pupil-plane correction to object-wise compensation by means of a tunable arbitrary-retarder array. The approach unlocks capabilities that were previously unattainable and promises significant benefits in applications ranging from materials characterisation to clinical diagnostics.

The work was driven by two limitations of existing vectorial adaptive optics (V-AO) schemes. First, they cannot deliver truly arbitrary, pixel-resolved conversion of phase and SoP, a prerequisite for comprehensive aberration correction anywhere within an optical system. Second, current sensor-less V-AO implementations still require cumbersome field-conversion steps. These challenges were overcome by cascading three SLMs with a DM to create a virtual pixel array that functions as a tunable elliptical retarder at every pixel. The resulting device forms a universal vectorial corrector that can be placed directly at the object plane and operated in either sensor-based or sensor-less mode, thereby giving rise to the concept of O-AO.

Experimental results confirmed high correction quality for both operating modes through focal-spot metrics. The main practical constraints arise from the finite resolution and dynamic range of the SLMs, which limit performance when aberrations possess very high spatial frequency or large amplitude. These constraints are expected to relax with the introduction of higher-resolution modulators, improved superposition calibrations, and learning-based optimisation algorithms.

The array (i.e., the new AO corrector) expands the modern vectorial AO toolbox, enabling the correction of polarisation aberrations that previous devices could not address. Future research could explore more advanced vectorial modes, such as axis geometry manipulation. These implementations may benefit research areas beyond those discussed in this chapter, including direct laser writing and lithography technology.

Chapter 5 Assessing V-AO correction for complex aberrations

Chapter statement:

This chapter is based on the following publication: Using optical skyrmions to assess vectorial adaptive optics capabilities in the presence of complex aberrations. *Science Advances* **11**, eadv7904 (2025). The content has been adapted and extended for the purpose of this thesis.

5.1 Introduction V-AO and optical skyrmions

5.1.1 V-AO in non-depolarising media

This thesis considers V-AO implementation in non-depolarising media, where phase, retardance and diattenuation aberration may exist (see Fig. 5.1)[41,118]. For phase aberration, correction can in principle be achieved whenever the modulator provides sufficient dynamic range, as outlined in phase AO section in Chapter 2. Retardance aberrations have been shown to be correctable with the V-AO architectures developed in Chapters 3 and 4, provided adequate degrees of freedom for state of polarisation (SoP) conversion are available.[10,92,98,99,118–120]. Since phase and retardance aberrations have been readily compensated by existing strategies across various scenarios in prior works[12], this chapter focus here solely on diattenuation.

When it comes to diattenuation aberration, the decrease in intensity as light passes through the system intrinsically limits its amenability to SoP correction. The errors introduced by a perfect polariser, to take a trivial example, would be impossible to correct, as the attenuated polarization has zero intensity. This highlights the need to devise metrics that characterise diattenuating systems based on their potential correctability. Doing so enables a better understanding of the degree of correction that can be achieved, considering given important physical parameters of the set-up such as camera sensitivity. One way such a metric can be formulated is to consider the mapping that the system induces on the Poincaré sphere (PS). This chapter introduces non-trivial structured light, in the form of an optical skyrmion, which simultaneously possesses every possible SoP as a means to probe and characterise a system.

Figure 5.1: Non-depolarising media. Illustrations of how non-depolarising media affect the spatial distributions of intensity, phase and polarisation fields. Retardance in non-depolarising media affects phase and polarisation, while diattenuation impacts phase, polarisation, and intensity[12,121–123]. The spatially varying distributions of intensity, phase, and polarisation fields before and after passing through the non-depolarising media are shown. Circular planes represent the beam's spatial profiles in each of the three domains.

5.1.2 Optical skyrmion

The skyrmion[124] is a unified model to describe fundamental particles. Since its conception, the topological nature of the magnetic skyrmion has driven investigations into its use as potential information carriers, and such structures have been touted for their potential to revolutionise ultra-dense data storage[125–129]. Recently, optical skyrmions have been observed in evanescent waves, where their topological properties are carried through a spatially varying polarisation field[130–132]. Since then, the generation of optical skyrmions has been achieved in paraxial vector beams through a variety of different techniques[116,132–137]. The topological properties of the skyrmion along with associated applications still offer large scopes to be explored.

Skyrmions are characterised by their topological number (skyrmion number; SN) defined as

$$\mathrm{SN} = \frac{1}{4\pi} \iint_{\sigma} \mathbf{n} \cdot \left(\frac{\partial \mathbf{n}}{\partial x} \times \frac{\partial \mathbf{n}}{\partial y}\right) dx\, dy \tag{5.1}$$

where **n(x,y)** represents the vector field that describes the two-dimensional skyrmion, and σ represents the confined region.

In this chapter, the SN of a *Néel-type* skyrmionic beam[135] is harnessed to serve as a probe for characterising non-depolarising optical systems. Then a V-AO correction methodology for optimising measurements in aberrated polarimetric (Stokes/Mueller) microscopes was detailed. This work opens new avenues to the advanced use of the optical skyrmion in the context of V-AO, with broad implications for the future of sensing and imaging technologies.

5.2 V-AO for diattenuating optical systems

5.2.1 Mathematical descriptions of diattenuation

A diattenuator possesses two different absorption ratios for two eigen polarisation states[28]; it, in effect, attenuates the intensity of one eigenstate more than the other. Consequently, not only will there be a power reduction when light passes through a diattenuator, but also a change of SoP. Unlike phase or retardance aberrations, which can be fully compensated given a sufficient correction dynamic range or degrees of freedom (as they did not change polarisation entropy and therefore theoretically did not affect the correctability of AO devices), diattenuation can reduce portions of the beam's intensity below the camera's detection threshold. This intensity limitation fundamentally restricts correctability and does not occur when only phase or retardance is involved. Diattenuation can be induced from various common optical elements including through Fresnel's effects due to reflection and refraction and the intrinsic polarisation properties of biomedical tissues or materials samples[12,29,48,138–140].

Note an arbitrary diattenuator is characterised by three parameters: its extinction ratio (E), transmissive axis shape (S) and axis orientation (θ). The transmission ratios of the two orthogonal axes are denoted by p_x and p_y then the orthogonal components of the light field are related by:

$$E_x' = p_x E_x, 0 \leq p_x \leq 1 \tag{5.2}$$

$$E_y' = p_y E_y, 0 \leq p_y \leq 1 \tag{5.3}$$

where p_x and p_y are the attenuation coefficients and $0 \leq p_x$, $p_y \leq 1$. p_x (Or p_y) = 1 is for perfect transmission whereas p_x (or p_y) = 0 is for complete attenuation. Normally, the normalised attenuation coefficients are defined in trigonometric function form:

$$p_x = \cos\gamma \tag{5.4}$$

$$p_y = \sin\gamma \tag{5.5}$$

$$p_x{}^2 + p_y{}^2 = 1 \tag{5.6}$$

E is an intensity extinction ratio which is defined as the ratio between the attenuation coefficients of transmissive axis and orthogonal axes (normally we define $p_x \geq p_y$ to represent the attenuation coefficient of the transmissive axis),

$$E = \frac{p_x}{p_y} = \cot\gamma \tag{5.7}$$

S represents the shape of the transmissive axis of the diattenuator which can be described with Jones vector as:

$$S = \begin{bmatrix} \cos\theta \\ \sin\theta\, e^{i\delta} \end{bmatrix} \tag{5.8}$$

It has the exact same vectorial format as a light-wise Jones vector but represents the object-wise property of the shape of the transmissive axis. Thus, the Jones matrix of an arbitrary diattenuator can be expressed as:

$$\begin{aligned} J &= \begin{bmatrix} \cos\theta & -\sin\theta\, e^{-i\delta} \\ \sin\theta\, e^{i\delta} & \cos\theta \end{bmatrix} \begin{bmatrix} \cos\gamma & 0 \\ 0 & \sin\gamma \end{bmatrix} \begin{bmatrix} \cos\theta & \sin\theta\, e^{-i\delta} \\ -\sin\theta\, e^{i\delta} & \cos\theta \end{bmatrix} \\ &= \begin{bmatrix} \cos\gamma\cos^2\theta + \sin\gamma\sin^2\theta & (\cos\gamma - \sin\gamma)\cos\theta\sin\theta\, e^{-i\delta} \\ (\cos\gamma - \sin\gamma)\cos\theta\sin\theta\, e^{i\delta} & \cos\gamma\sin^2\theta + \sin\gamma\cos^2\theta \end{bmatrix} \end{aligned} \tag{5.9}$$

The Mueller matrix of an arbitrary diattenuator can be converted from a Jones matrix by:

$$\begin{aligned} M &= A\,(J \otimes J^*)A^{-1} \\ &= \frac{1}{2}\begin{bmatrix} 1 & D^T \\ D & m_D \end{bmatrix} \end{aligned} \tag{5.10}$$

where $\otimes$ represents the Kronecker product, D is the diattenuation vector, m_D represents the lower 3×3 sub-matrix, and A

$$A = \begin{bmatrix} 1 & 0 & 0 & 1 \\ 1 & 0 & 0 & -1 \\ 0 & 1 & 1 & 0 \\ 0 & i & -i & 0 \end{bmatrix} \tag{5.11}$$

By replacing the eigenvector terms in J with Stokes vector notations:

$$S = \begin{bmatrix} S_0 \\ S_1 \\ S_2 \\ S_3 \end{bmatrix} = \begin{bmatrix} 1 \\ \cos 2\theta \\ \sin 2\theta \cos \delta \\ \sin 2\theta \sin \delta \end{bmatrix} = \begin{bmatrix} 1 \\ S \end{bmatrix} \tag{5.12}$$

we can get:

$$D = \cos 2\gamma \begin{bmatrix} S_1 \\ S_2 \\ S_3 \end{bmatrix} = \cos 2\gamma S \tag{5.13}$$

$$m_D = \sin 2\gamma I_{3\times 3} + (1 - \sin 2\gamma) S \bullet S^T \tag{5.14}$$

5.2.2 V-AO placement strategy and correction limits

In previous work, the V-AO correction module was effectively realised by a cascade of two SLMs and a DM. To achieve arbitrary-to-arbitrary phase and arbitrary SoP to arbitrary SoP conversion (ATA), a new V-AO module comprising four SLMs (or three SLMs and a DM) is also proposed[92,98,99,141] (see Fig. 5.2a). Phase, as a scalar quantity, can be arbitrarily modulated using a single device, thus our experiments in this work mainly adopt the three-SLM configurations to specifically target polarisation control. The versatility of ATA devices enables their broad applications across many different scenarios, including the illumination and detection arms of modern Stokes/Mueller microscopes[48] that require specific uniform SoPs for effective sample illumination and analysis[46,142].

In V-AO, the matrix reciprocity issue is crucial, particularly the placement of AO devices relative to aberrations influences system performance. With ATA ability, assuming no intensity loss, an AO module placed after the aberration (see Fig. 5.2 (b); location 2) can always correct for the system, barring complete intensity attenuation. However, positioning the AO device before the aberration (see Fig. 5.2(b); location 1), which is required by the pre-correction systems and associated applications, will introduce complexity. This is because a diattenuator may attenuate certain SoPs in the output field which cannot be recovered via pre-correction, thus limiting the aberration correction ability of V-AO even with perfect ATA. For instance, one can easily show that if the DoP of the incident light is smaller than the diattenuation of the system, then the transformation of the PS induced by the diattenuating element is not surjective[116], and therefore there exist SoPs that can never be present in the output.

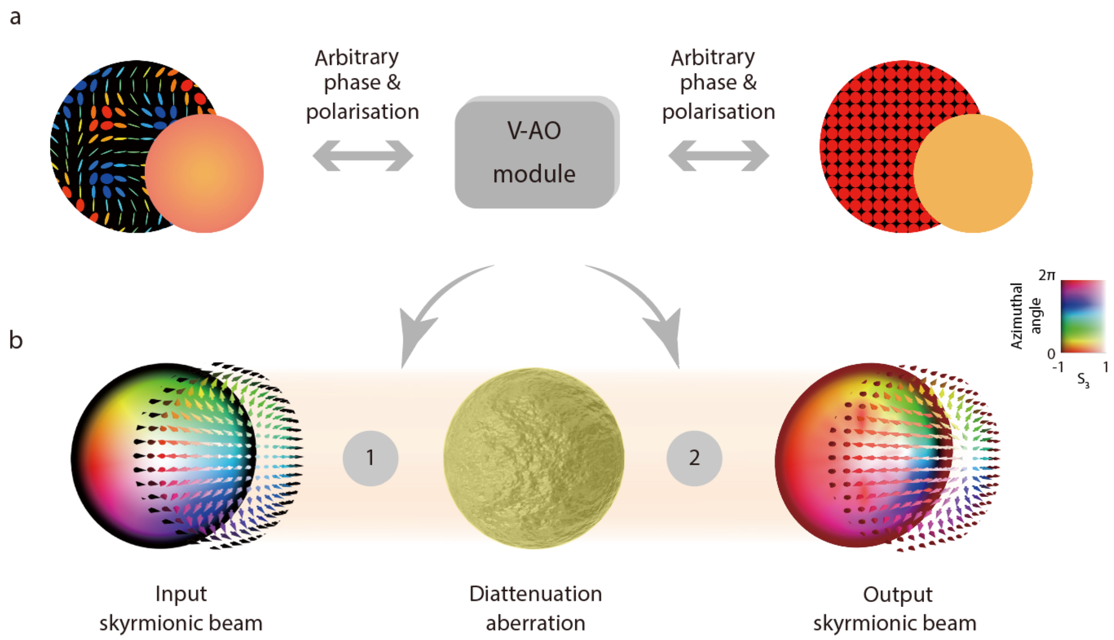

Figure 5.2: V-AO correction module, and schematic of V-AO correction strategy for a diattenuation aberration. (a) The V-AO module, consisting of a cascade of four SLMs, enables arbitrary phase and SoP conversion. This capability is essential for correcting spatially varying vectorial aberrations, such as phase, polarisation, and intensity aberrations, that commonly arise in non-depolarising media. (b) The V-AO pre-correction strategy towards diattenuation aberration is illustrated, with the V-AO module positioned before the aberration. It also illustrates the Stokes fields of a typical *Néel-type* skyrmion as it passes through this diattenuation aberration. Colour is used to represent the azimuthal angle on the PS, and saturation is used to represent height (similar to ref[135]).

5.3 Optical skyrmions for assessing correctability

5.3.1 Theoretical model and polarimetric analysis

Using the SN as the evaluation metric enables direct assessment of V-AO correction capability without requiring explicit reconstruction of diattenuation parameters through matrix inversion or multiple measurements involving complex setups. The number of SoPs that remain detectable after passing through the diattenuation reflects the residual polarisation diversity, which is equivalent to V-AO system's remaining correction capability to enable effective aberration compensation. This directly benefits applications such as maintaining optimised SoPs required for imaging tasks in polarimetry.

The theoretical model presented in this section describes how an intensity threshold level F, defined by detector sensitivity, intersects with the PS representation of the SoP. When a skyrmionic beam passes through a diattenuator, intensity of certain output SoPs may be attenuated below the threshold. This results in a spherical cap being removed from the observable SoP domain. The radius of this cap is jointly determined by the threshold level F and the extinction ratio E, and its geometry is analytically described.

This framework enables the SN to serve as a global metric that quantitatively reflects the polarisation diversity retained in the system, providing a direct and interpretable assessment of V-AO correctability, with potential applications in fields such as biomedical imaging, astronomy, and communications.

5.3.1.1 General derivations

For an arbitrary incident light,

$$S_{in} = \begin{bmatrix} S_{in0} \\ S_{in1} \\ S_{in2} \\ S_{in3} \end{bmatrix} = \begin{bmatrix} 1 \\ \cos 2\theta \\ \sin 2\theta \cos \delta \\ \sin 2\theta \sin \delta \end{bmatrix} = \begin{bmatrix} 1 \\ S_{in} \end{bmatrix} \tag{5.15}$$

therefore, the Stokes vector of the outgoing light can be expressed as:

$$S_{out} = \frac{1}{2}\begin{bmatrix} 1 & D^T \\ D & m_D \end{bmatrix}\begin{bmatrix} 1 \\ S_{in} \end{bmatrix} = \frac{1}{2}\begin{bmatrix} 1 + D^T * S_{in} \\ D + m_D * S_{in} \end{bmatrix} = \begin{bmatrix} I \\ S_{out} \end{bmatrix} \tag{5.16}$$

The intensity can be expressed as:

$$\begin{aligned} I &= S_{out0} \\ &= \frac{1}{2}\left(1 + D^T * S_{in}\right) \\ &= \frac{1}{2}\left(1 + cos\ 2\gamma S^T * S_{in}\right) \end{aligned} \tag{5.17}$$

And the polarisation vector can be expressed as:

$$S_{out} = \frac{1}{2}(D + m_D * S_{in}) \tag{5.18}$$

In Fig. 5.3, we represent the simulated output Stokes fields of a *Néel-type* skyrmionic beam that are modulated by different diattenuators.

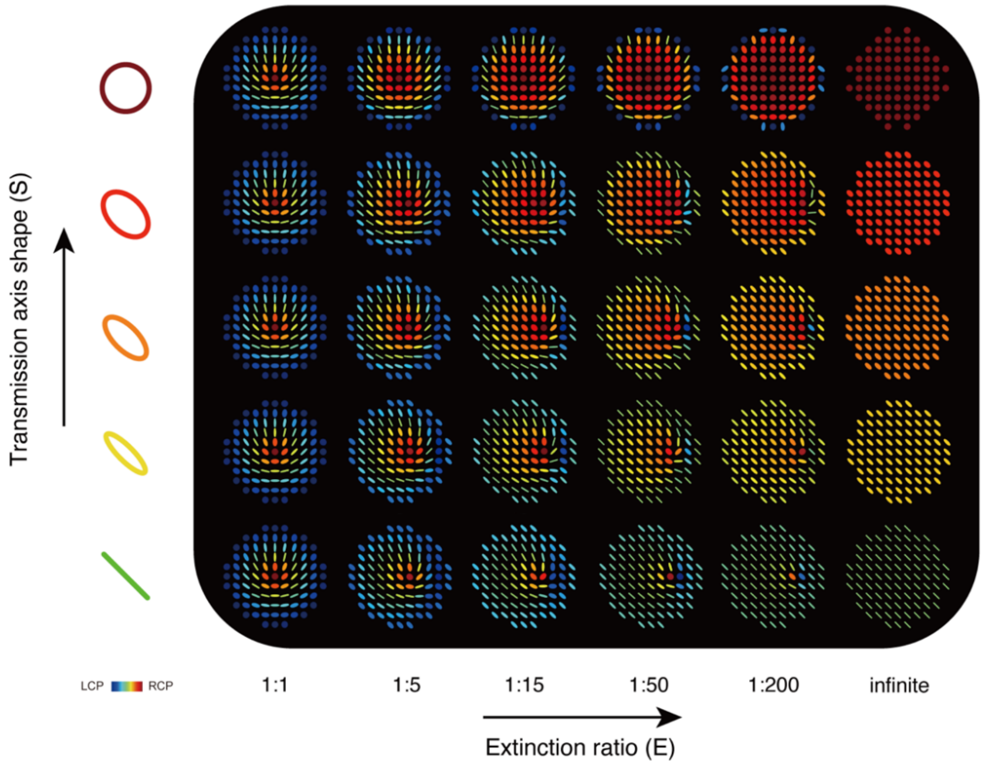

Figure 5.3: The output Stokes fields as a result of *Néel-type* skyrmionic beams being modulated by different diattenuators. The x axis of the figures represents different diattenuation values (E) of the diattenuators, and the y axis represents different transmissive axis shapes (S). The shaded region (dark grey region) represents the filtered-out region when applying the intensity filter F=0.1.

5.3.1.2 The incident field

If we set a certain criterion to filter the output intensity, we can cut a certain region on the PS, assuming that the diattenuator has a non-ideal extinction ratio. Given that $I \le F$ and assuming that $0 < \gamma < 45°$, we can derive:

$$I \le F$$

$$\frac{1}{2}\left(1+\cos 2\gamma\, S^T * S_{in}\right) \leq F$$

$$S^T * S_{in} \leq \frac{2F-1}{\cos 2\gamma}$$

$$s_1 \bullet S_{in1} + s_2 \bullet S_{in2} + s_3 \bullet S_{in3} \leq \frac{2F-1}{\cos 2\gamma} \tag{5.19}$$

As S and S_{in} are from the normalized Stokes vector, thus ${s_1}^2 + {s_2}^2 + {s_3}^2 = 1$ and ${S_{in1}}^2 + {S_{in2}}^2 + {S_{in3}}^2 = 1$. So,

$$(s_1 + S_{in1})^2 + (s_2 + S_{in2})^2 + (s_3 + S_{in3})^2 \leq \frac{4F-2}{\cos 2\gamma} + 2$$

$$((-s_1) - S_{in1})^2 + ((-s_2) - S_{in2})^2 + ((-s_3) - S_{in3})^2 \leq \frac{4F-2}{\cos 2\gamma} + 2 \tag{5.20}$$

It turns out that the incident light which will be filtered out after passing through the arbitrary diattenuator will cover a spherical cap on the PS which is cut by a plane perpendicular to the axis $[-s_1, -s_2, -s_3]$. And the max distance between the filtered Stokes vector and the axis vector is defined as:

$$D = \frac{4F-2}{\cos 2\gamma} + 2 \tag{5.21}$$

Mathematically, this distance represents the Euclidean separation in the normalised Stokes space, serving as a quantitative metric to evaluate the maximum deviation of the local polarisation states from the target SoP.

It implicitly defines:

$$2 \geq \frac{4F-2}{\cos 2\gamma} + 2 \geq 0$$

$$\frac{1}{2} \geq F \geq \frac{1-\cos 2\gamma}{2} \tag{5.22}$$

So we can define the boundary condition for the filter as:

$$S^T * S_{in} = s_1 \bullet S_{in1} + s_2 \bullet S_{in2} + s_3 \bullet S_{in3} = \frac{2F-1}{\cos 2\gamma} = \chi \tag{5.23}$$

Then according to the geometric relationship, the radius of the corresponding latitude circle can be expressed as:

$$R_{in} = D\sqrt{1-(\frac{D}{2})^2} = \sqrt{1-\chi^2} \tag{5.24}$$

5.3.1.3 The output field

It can also be proved that, for a given intensity filter value F, the output light which is filtered out will also cover a spherical cap on the PS which is cut by a plane perpendicular to the axis $[-s_1, -s_2, -s_3]$. This can also be demonstrated by calculating the distance between the polarisation vector (normalized Stokes vector) and eigen-vector $-S$, which is:

$$\begin{aligned} D^2 &= \left\|\hat{S}_{out} + S\right\|^2 = \left\|\frac{\cos 2\gamma\, S + m_D * S_{in}}{1+\cos 2\gamma\, S^T * S_{in}} + S\right\|^2 \\ &= \left\|\frac{(1+\cos 2\gamma)\, S + (m_D + \cos 2\gamma\, SS^T) * S_{in}}{1+\cos 2\gamma\, S^T * S_{in}}\right\|^2 \\ &= \left\|\frac{(1+\cos 2\gamma)S + m_D{}' * S_{in}}{1+\cos 2\gamma S^T * S_{in}}\right\|^2 \end{aligned} \tag{5.25}$$

where $\hat{S}_{out}$ is the normalized vector of S_{out} and we define $m_D{}'$:

$$m_D{}' = m_D + \cos 2\gamma\, SS^T$$

$$= \begin{bmatrix} \sin 2\gamma + (1-\sin 2\gamma + \cos 2\gamma){s_1}^2 & (1-\sin 2\gamma + \cos 2\gamma)s_1 s_2 & (1-\sin 2\gamma + \cos 2\gamma)s_1 s_3 \\ (1-\sin 2\gamma + \cos 2\gamma)s_1 s_2 & \sin 2\gamma + (1-\sin 2\gamma + \cos 2\gamma){s_2}^2 & (1-\sin 2\gamma + \cos 2\gamma)s_2 s_3 \\ (1-\sin 2\gamma + \cos 2\gamma)s_1 s_3 & (1-\sin 2\gamma + \cos 2\gamma)s_2 s_3 & \sin 2\gamma + (1-\sin 2\gamma + \cos 2\gamma){s_3}^2 \end{bmatrix}$$

$$= \begin{bmatrix} m'_{D11} & m'_{D12} & m'_{D13} \\ m'_{D21} & m'_{D22} & m'_{D23} \\ m'_{D31} & m'_{D32} & m'_{D33} \end{bmatrix} \tag{5.26}$$

We know that:

$$\chi = s_1 \bullet S_{in1} + s_2 \bullet S_{in2} + s_3 \bullet S_{in3}$$

$$\chi^2 = {s_1}^2 \bullet {S_{in1}}^2 + {s_2}^2 \bullet {S_{in2}}^2 + {s_3}^2 \bullet {S_{in3}}^2 + 2s_1 S_{in1} s_2 S_{in2} + 2s_1 S_{in1} s_3 S_{in3} + 2s_2 S_{in2} s_3 S_{in3} \tag{5.27}$$

Then it can be calculated that,

$$(1+\cos 2\gamma\,\chi)^2 D^2 = 2(1+\cos 2\gamma) + 2(1+\cos 2\gamma)^2\chi + 2\cos 2\gamma\,(1+\cos 2\gamma)\chi^2$$

$$= 2(1+\cos 2\gamma)(1+\chi)(1+\cos 2\gamma\,\chi)$$

Thus,

$$D^2 = \frac{2(1+\chi)(1+\cos 2\gamma)}{(1+\cos 2\gamma\chi)} \tag{5.28}$$

The radius of the corresponding latitude circle in the output field can be expressed as:

$$R_{out} = D\sqrt{1-(\frac{D}{2})^2} = \frac{\sin 2\gamma}{1+\cos 2\gamma\chi}\sqrt{1-\chi^2} \tag{5.29}$$

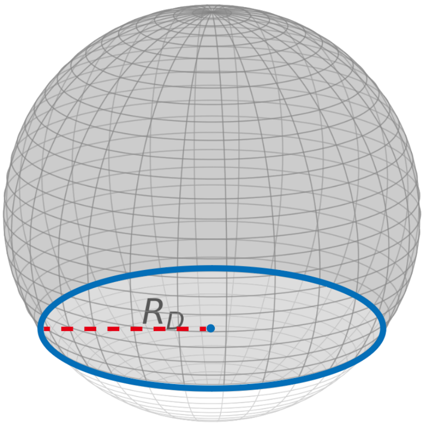

Figure 5.4: Schematic of the output SoP distribution after diattenuation on the PS. The grey region indicates the remaining (detectable) output states on the normalised PS, while the white spherical-cap region represents incident states that are cut off by the detection threshold after diattenuation.

It is intuitive that after modulation by a diattenuator, if the beam still serves as a single unit skyrmionic beam (with SN=1), it implies the preservation of all SoPs in the output. Hence an AO device can do pre-correction to correct the errors introduced by any such aberration. Conversely, a deviation from SN=1 signifies that the output beam no longer contains all the SoPs, suggesting there exist certain SoPs that cannot be pre-corrected by V-AO. Therefore, the output SoP field can be used to quantitatively evaluate the correction ability of a V-AO system towards such an aberration. In particular, the change in SN serves as a quantitative measure for the loss of SoPs through the diattenuator. Beyond the correctability of V-AO, such an evaluation is important for many applications, such as advanced dipole orientation-based fluorescence super-resolution microscopes[4] or Stokes vector/Mueller matrix microscopes[48], where the ability to generate arbitrary SoPs is essential for effective illumination and analysis. It is noted that this approach does not conflict with the topological protection properties of optical skyrmions under diattenuation, as defining the integration region through intensity filtering already breaks the field continuity, and thus the SN is expected to change[116]; Therefore, the new integration region is defined by excluding the portion of the beam that falls below the intensity threshold, in accordance with the criterion described above.

To investigate the correction ability of V-AO for compensation of arbitrary diattenuation, we used such a *Néel-type* optical skyrmionic beam as input field and conducted simulations to evaluate the change in SN after passing through a diattenuator. The orientation θ of the transmissive axis was fixed at 45° throughout this work, as it does not affect the loss of SoPs. Fig. 5.5 illustrates the output fields obtained from the input beam interacting with different diattenuators. The x axis of Fig. 5.5 represents the different extinction ratios (E) of the diattenuators, whereas the y axis represents different axis shape (S). The observed trend shows an increasing homogeneity in the output fields with rising E values, reaching completely homogeneous when E approaches infinity. A similar effect can be observed along the y axis with the increasing ellipticity of S.

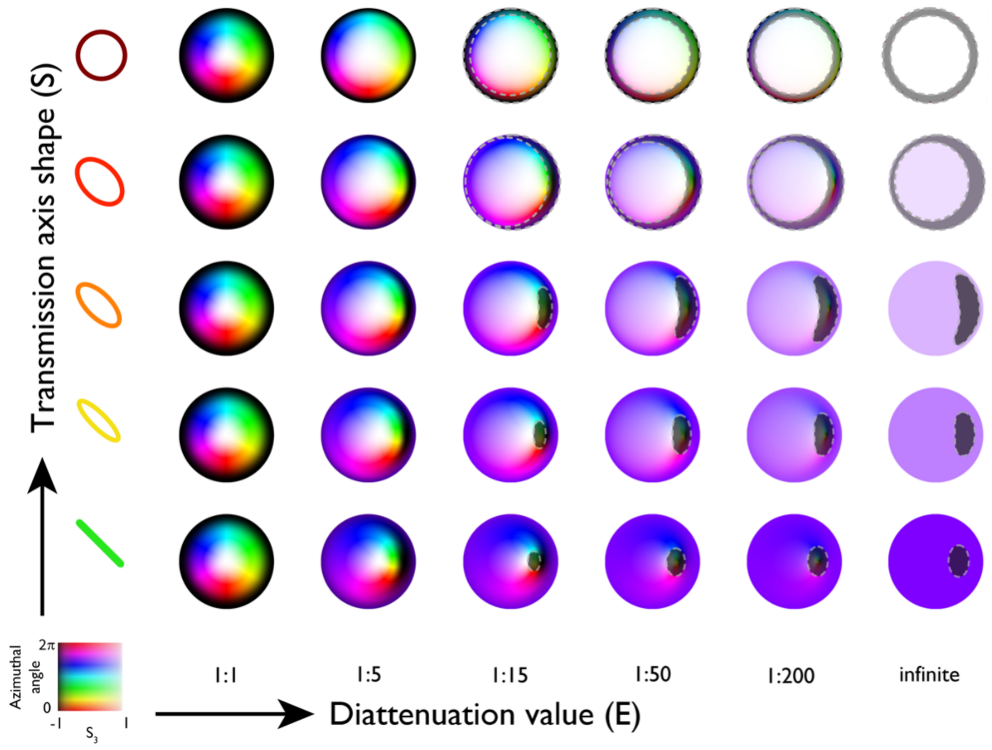

Figure 5.5: The output skyrmionic fields after being modulated by different diattenuators. Illustration of how different diattenuation values (represented on the x-axis) and the transition of the transmissive axis shape from linear to right-hand circular

(depicted on the y-axis) influence the *Néel-type* skyrmionic beams. The orientation of transmissive axis is consistently maintained at 45° throughout the work. The highlighted shaded area (dark grey area) indicates regions excluded by applying an intensity filter threshold of $F = 0.1$, illustrating the impact of diattenuation on the detectability of certain field regions.

5.3.1.4 Characterisation of diattenuations

To provide a quantitative basis that supports our skyrmion-based correction evaluation framework, the ground-truth parameters of the samples – extinction ratio E, transmission-axis orientation θ, and axis-shape parameter S – are measured from established polarimetric techniques. Two complementary studies were conducted: (i) experimental Mueller- and Stokes-based measurements, and (ii) LUT-driven simulations that sweep the parameter space under noise-free conditions

1) **Experimental characterisation.** The diattenuation properties were characterised using conventional Mueller matrix and Stokes polarimetry. This includes characterisation of the extinction ratio E, the shape of transmissive axis S, and the axis orientation θ. As shown in Fig. 5.6, representative measurements are presented for six diattenuation configurations (A-F), corresponding to extinction ratios $E = 1, 1.65, 2.76, 3.36, 4.16, 724.79$. Configurations A to E were

equivalently obtained using either single or cascaded weak diattenuators (i.e., beam splitters here), while the configuration F employed commercial polarisers to simulate strong diattenuators, theoretically approaching infinite values. As E increases, the output SoPs converge towards the transmissive axis of the diattenuator.

For each diattenuation configuration shown in Fig. 5.6, the corresponding Mueller matrix of the sample was measured using a standard polarimetric setup; these results are presented in the first row of the figure. To illustrate the effect of each diattenuation, three representative input SoPs – horizontal linear, right-circular, and +45◦ linear – were applied, and the resulting output fields were recorded using Stokes polarimetry and displayed in the remaining three rows. The measured results serve as a quantitative basis that supports the skyrmion-based method, which achieves direct assessment of system correctability without requiring multiple input SoPs or full Mueller matrix reconstruction.

These experiments were conducted using spatially uniform samples to ensure control and interpretability of the results (as mentioned before), thereby providing a reliable basis for defining the correction boundary. Once the underlying correction limits are known, the system's pixelated control architecture can be applied effectively to achieve aberration correction.

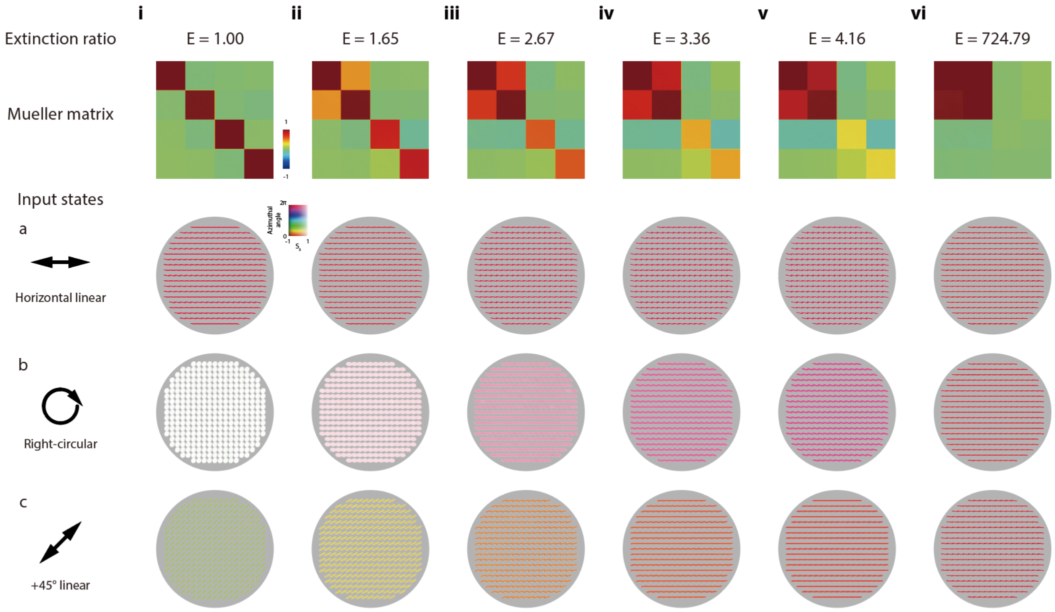

Figure 5.6: Experimental diattenuation characterisation via Mueller and Stokes polarimetry. Six representative diattenuation cases (i–vi) with increasing extinction ratios ($E = 1, 1.65, 2.76, 3.36, 4.16, 724.79.$) are shown. For each configuration, the first row presents the measured Mueller matrix, then followed by the output Stokes fields for three input states – (a) horizontal linear, (b) right-circular, and (c) +45◦ linear. As E increases, the output fields gradually converge towards the diattenuation's transmissive axis, revealing the stronger attenuation against the orthogonal component.

2) **Simulation results.** The simulation approach uses a look-up table (LUT), constructed by simulating the Jones matrices of diattenuators across a range of the key parameters, including extinction ratio, axis orientation, and shape. These matrices are used to simulate the corresponding diattenuation effects under

various configurations, and the results are recorded into the LUT. To find the matched simulation results, the experimental diattenuation parameters for each sample, measured using Mueller matrix polarimetry, are mapped to the closest entries in the LUT.

The results shown in Fig. 5.7 demonstrate that the LUT-based simulation framework can reveal physical characteristics of the samples and provide a solid basis for exploring the potential of further skyrmion-based probing approaches as a cost-effective method for diattenuation analysis.

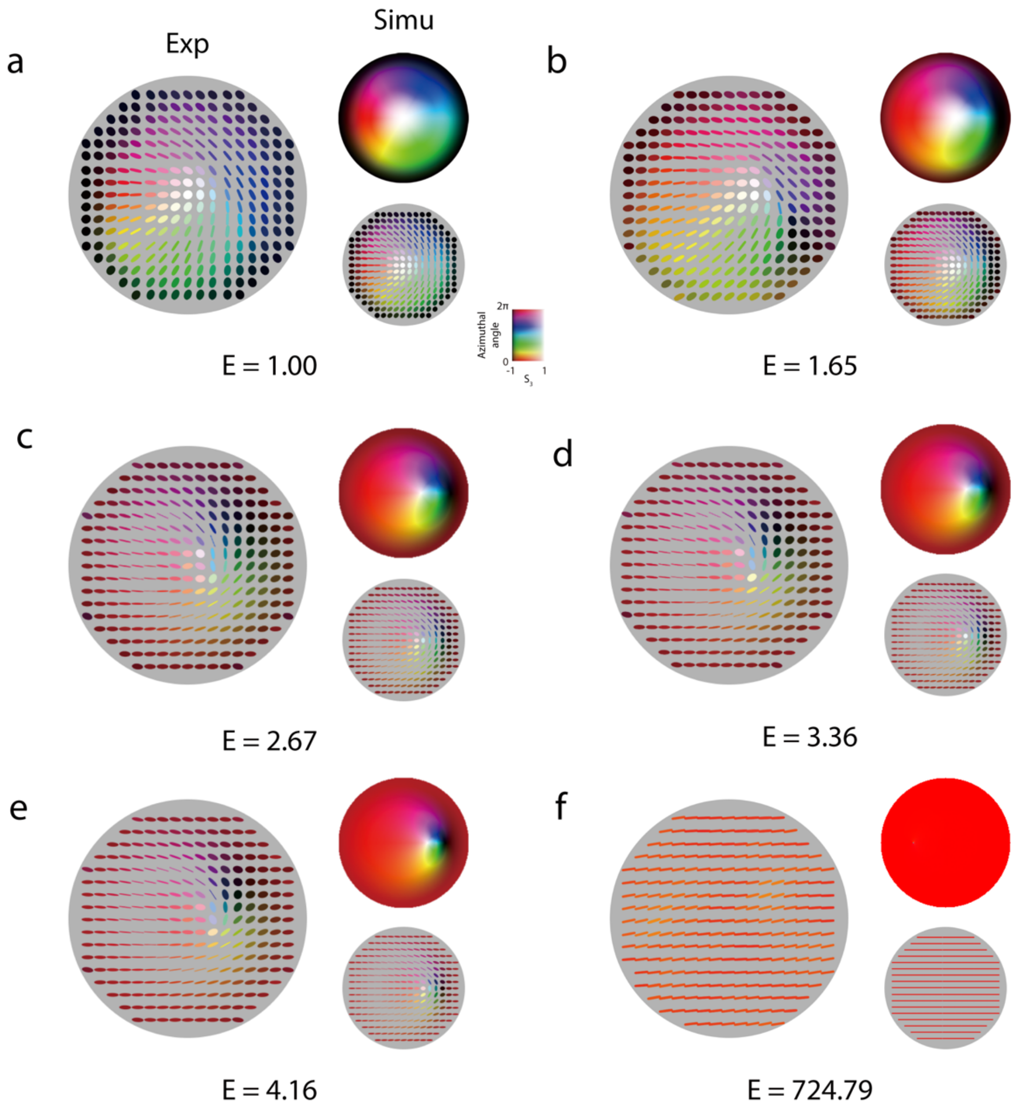

Figure 5.7: Experimental and simulated Stokes fields with corresponding skyrmionic structures under varying diattenuations. Stokes fields measured experimentally after propagation through diattenuators with extinction ratios (E) of (a) $E = 1$, (b) $E = 1.65$, (c) $E = 2.67$, (d) $E = 3.36$, (e) $E = 4.16$, and (f) $E = 724.79$ are displayed to the left. For each case, the corresponding simulated Stokes field and skyrmionic structure are presented to the right.

5.3.2 Characterisation of output skyrmionic fields

A proof-of-concept experiment was conducted to validate that the SN can be used to evaluate the V-AO correction ability for diattenuation aberrations. An incident unit skyrmionic beam was generated via a cascade of SLMs as shown in Fig. 5.8.

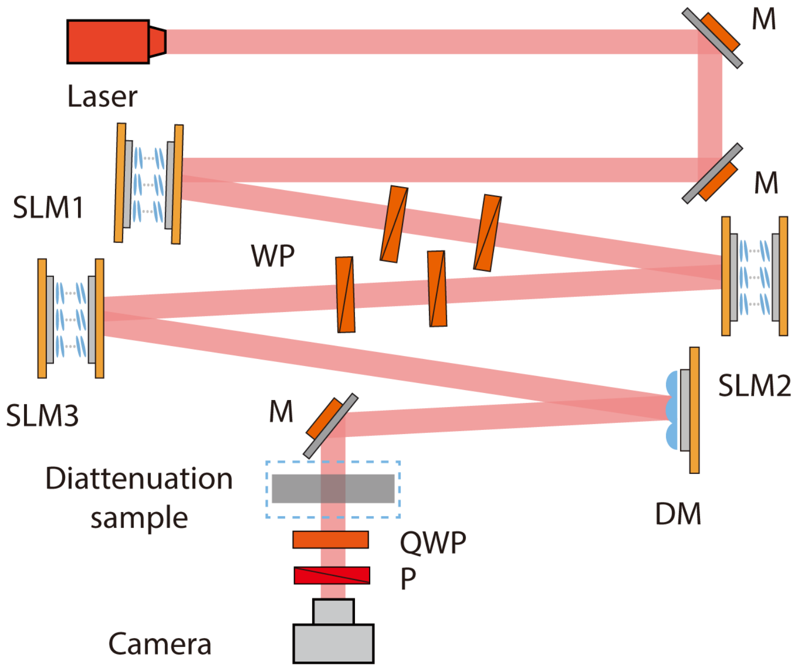

Figure 5.8: Illustration of experimental setup. The skyrmionic beam generator and Stokes polarimeter configuration. A He-Ne Laser (Melles Griot, 05-LHP171, 632.8 nm) serves as the light source. The beam is modulated by a cascade of three SLMs (Hamamatsu, X10468-01) to obtain the desired SoP field and a DM (Boston Micromachines Corporation, Multi-3.5) to compensate the initial phase aberration. A waveplate assembly (WP, Thorlabs, WPH10M-633) is used to set the axes of two SLMs at 45° angle. The modulated beam then passes through the diattenuation sample and is analysed by the Stokes polarimeter, comprising a quarter-waveplate (QWP, Thorlabs, WPQ10M-633), a polariser (P, Thorlabs, GL10-A) and a camera (Thorlabs, DCC3240N).

The calibration result of SLMs is shown in Fig. 5.9, demonstrating the precise pixelated control of SLMs.

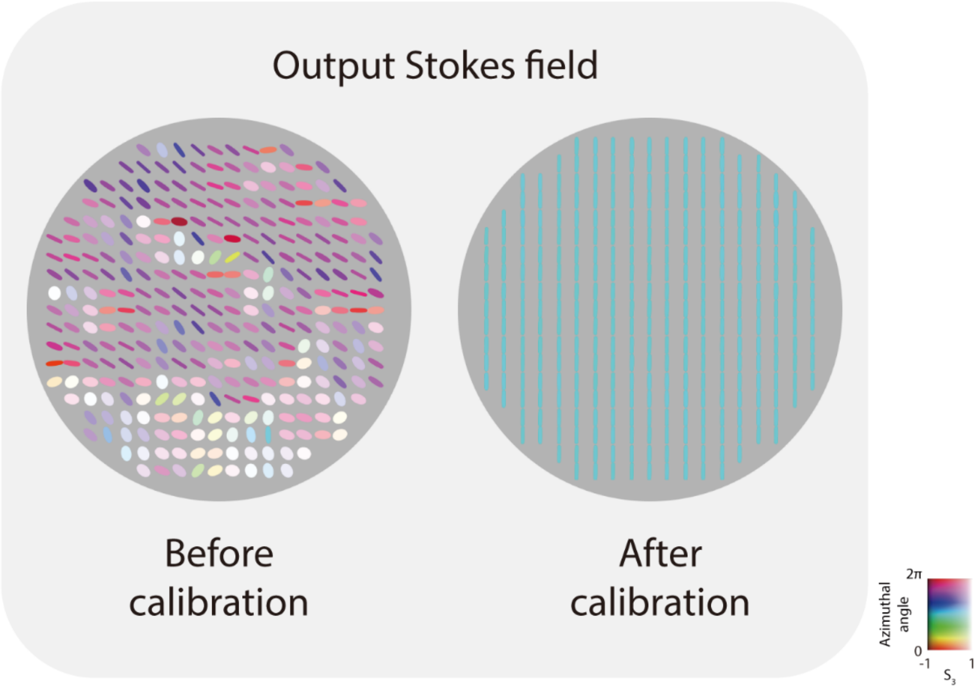

Figure 5.9: SLM calibration result. The output Stokes field before and after SLM calibration is shown. Different ellipses and colours represent different Stokes vectors.

The experiment proceeded as follows. First, after initial SLM calibration, the correct phase patterns were applied to each SLM to generate the target skyrmionic beam. Second, the diattenuation sample was placed after the DM. Third, a Stokes polarimeter was utilised to measure the output SoP field after the beam passed through the diattenuation sample. This process was repeated for different diattenuation samples. The output Stokes and skyrmionic fields are shown in Fig.

5.10, the experimental and theoretical results of both Stokes fields and skyrmionic fields (see Fig. 5.7) are well matched. Fig. 5.10 presents three simulated curves based on different intensity thresholds, illustrating the changes in SN as E increases. This demonstrated that the change of SN can quantitatively indicate the diminishing correction ability of V-AO system within this framework.

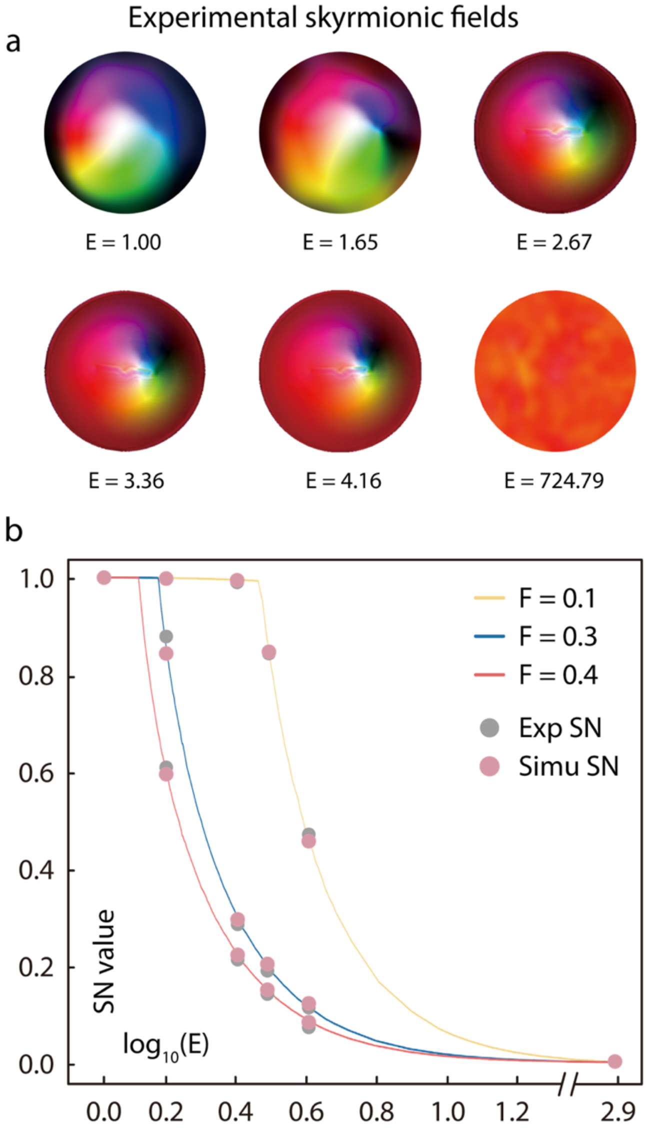

Figure 5.10: Characterisation of output skyrmionic fields and SN values under different diattenuation aberration configurations. (a) Experimental skyrmionic fields after passing through diattenuations with $E = 1, 1.65, 2.76, 3.36, 4.16. 724.79$. (b) Simulated relationship between SN and E, evaluated under three intensity thresholds $F = 0.1, 0.3, 0.4$, respectively. SN is calculated over the region with intensity greater than F. A logarithmic scale (base 10) is used to encompass a broad range of diattenuation values.

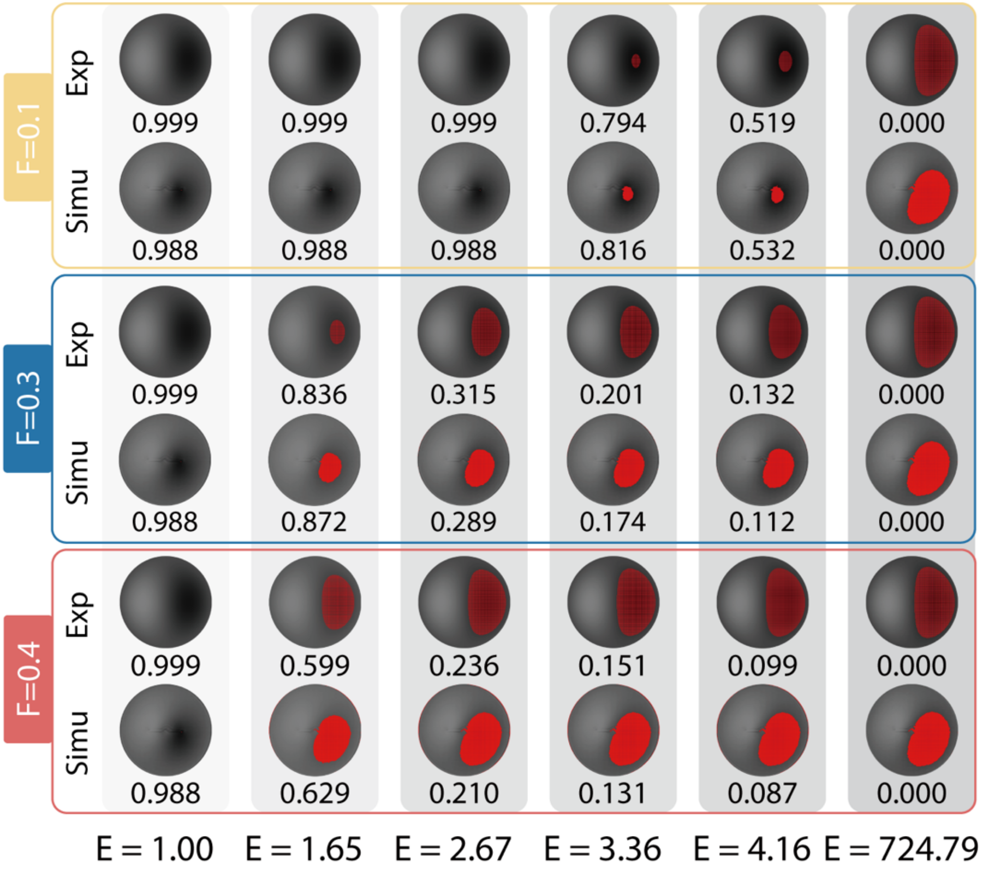

Figure 5.11: Intensity images after different diattenuation aberration. Simulated and experimental output intensity images for each threshold *F*. Top and bottom rows show simulated and experimental results, respectively. Red areas indicate regions excluded by the threshold. Numerical SN values are annotated below each image.

Note that the sudden drop in the SN is primarily attributed to the implementation of the intensity filter threshold. As the diattenuation value increases, the attenuation of light intensity becomes more pronounced, resulting in certain SoPs in the output field falling below this threshold, which are marked red in Fig. 5.11.

These SoPs are consequently excluded from the analysis, leading to a sharp decline in SN.

As the homogeneity of the Stokes vector field increases, the correction ability of V-AO diminishes due to an augmented loss of SoPs. This shows that within any V-AO framework employing pre-correction strategies for existing diattenuation, there always exist SoPs that remain inherently uncorrectable via current V-AO techniques. Consequently, the correction ability towards diverse diattenuations can be in effect quantified via the SN, establishing a critical connection between V-AO correction ability and given diattenuator through a single metric.

Such a relationship and quantitative descriptions are important as they potentially provide a look-up-table, or a reference framework, to enhance the practical application of V-AO system. For instance, the performance of advanced polarisation sensing systems utilised in biomedical research is susceptible to diattenuation aberration due to light propagation through the sample[143]. The correction ability can be derived by analysing the SN value, and the optical system can be corrected accordingly (apply V-AO directly, or first use passive compensation to precondition the system for possible V-AO operation), enhancing the efficiency.

5.4 V-AO assisted polarimetric measurement

Stokes vector and Mueller matrix microscopy are pivotal techniques for acquiring vectorial information and are valuable for material characterisation and pathological diagnosis[48,138,140,144–155]. The accuracy of vectorial information is one of the core aspects of Stokes-Mueller polarimetry, but can be significantly affected by vectorial aberrations, including phase, retardance and diattenuation. Phase and retardance can be effectively corrected by using existing AO toolboxes since they do not intrinsically limit the correction ability of the AO system within its dynamic range. However, diattenuation introduces unique challenges due to its impact on intensity in addition to phase and SoP. Despite diattenuation being common in optical components, such as beam splitters, conventional calibration methods have not addressed this problem.

In this section, the effectiveness of V-AO was first demonstrated, as probed by the optical skyrmionic field, in correcting diattenuation aberrations. Two spatially varying samples of high practical significance were selected – specifically, biomedical and archaeological samples. The biomedical sample is a bone marrow trephine from a myelofibrosis case, where vectorial information captures fibrotic structural changes that are critical for pathological analysis, clinical staging, and precise treatment planning[141]. The archaeological sample is red pigment extracted from cinnabar used in China during the Qin and Han dynasties, the vectorial analysis of the cinnabar is essential for tracing the mineral's provenance[141].

5.4.1 V-AO correction for real-world samples

The procedure proceeded as follows: first, to obtain the ground truth of the samples' vectorial information, a circular SoP illumination was used and the polarimetric images of the samples were recorded without any induced diattenuation with the results shown in Fig. 5.12(a) and 5.13(a); second, to validate the performance of V-AO system under non-recoverable aberration, a diattenuation with $E = 3.36$ is introduced. The output Stokes fields before and after V-AO correction are shown in Fig. 5.12(b) and 5.13(b). Under this severe diattenuation, intensities of certain SoPs (masked in red) were attenuated below the detection threshold, resulting in unrecoverable SoPs, thus revealing the intrinsic correction limit of V-AO system; third, the aberrated and corrected output Stokes field after passing through a diattenuation with $E = 1.65$ (within the correction boundary) is recorded. As shown in Fig. 5.12(c) and 5.13(c), V-AO effectively restored the Stokes fields; finally, to further quantify the correction performance, the matching error between corrected output and the ground-truth SoPs by calculating the Euclidean distance between them[118,141,156], with results plotted in Fig. 5.12(d) and 5.13(d).

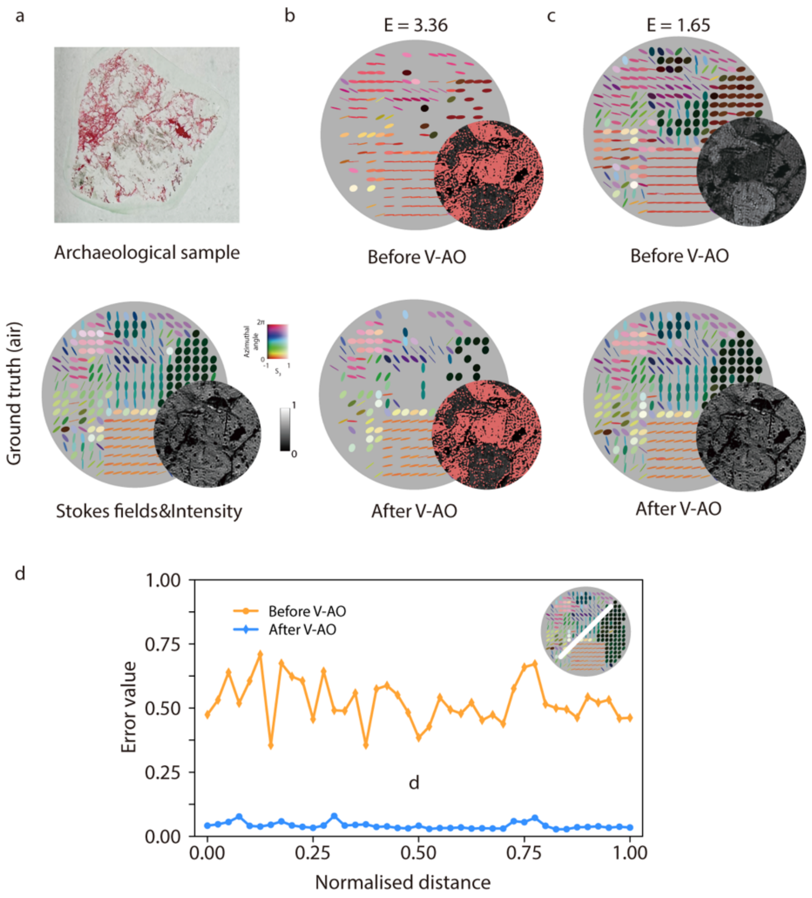

Figure 5.12: Diattenuation correction in archaeological sample via V-AO. Here (a) presents the real world picture and ground truth reference field; (b) shows results under a severe diattenuation ($E = 3.36$) before and after V-AO correction; (c) illustrates the corresponding results for a moderate diattenuation ($E = 1.65$); and (d) quantifies the correction performance by plotting the matching error between the corrected SoPs and the ground truth (which is evaluated by their Euclidean distance) along a selected cross-section of the field with a moderate diattenuation. Regions where SoPs fall below the detection threshold are indicated by red-marked areas in the intensity image.

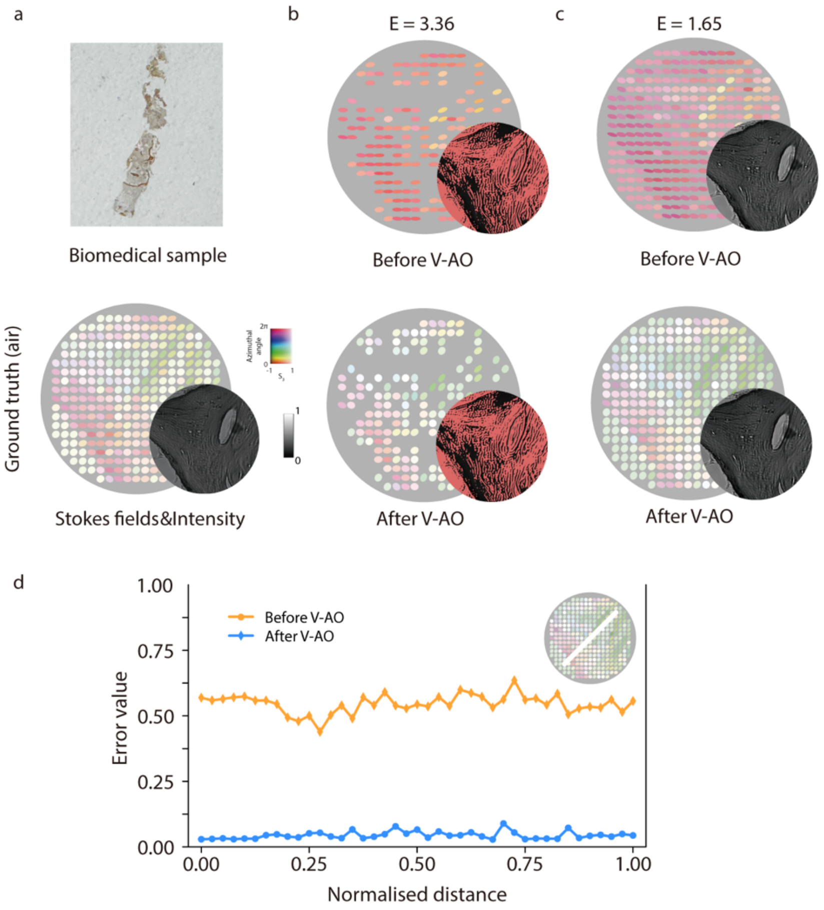

Figure 5.13: Diattenuation correction in biomedical sample via V-AO. Panel layout, definitions and analysis are identical to Fig. 5.11. Briefly, (a) photograph and ground-truth Stokes field; (b) results before/after V-AO under severe diattenuation; (c) under moderate diattenuation; (d) matching-error profile along the selected cross-section.

For moderate diattenuation, full SoP recovery was achieved through V-AO correction, confirming the system's effectiveness in complex, spatially varying media. However, under severe diattenuation (condition 4), some SoPs were attenuated below the detection threshold, resulting in signal loss and unrecoverable polarisation states. This limitation is visible as dark regions in the

Stokes fields and red-shaded areas in the intensity images, indicating that the correction capacity of the V-AO system was exceeded.

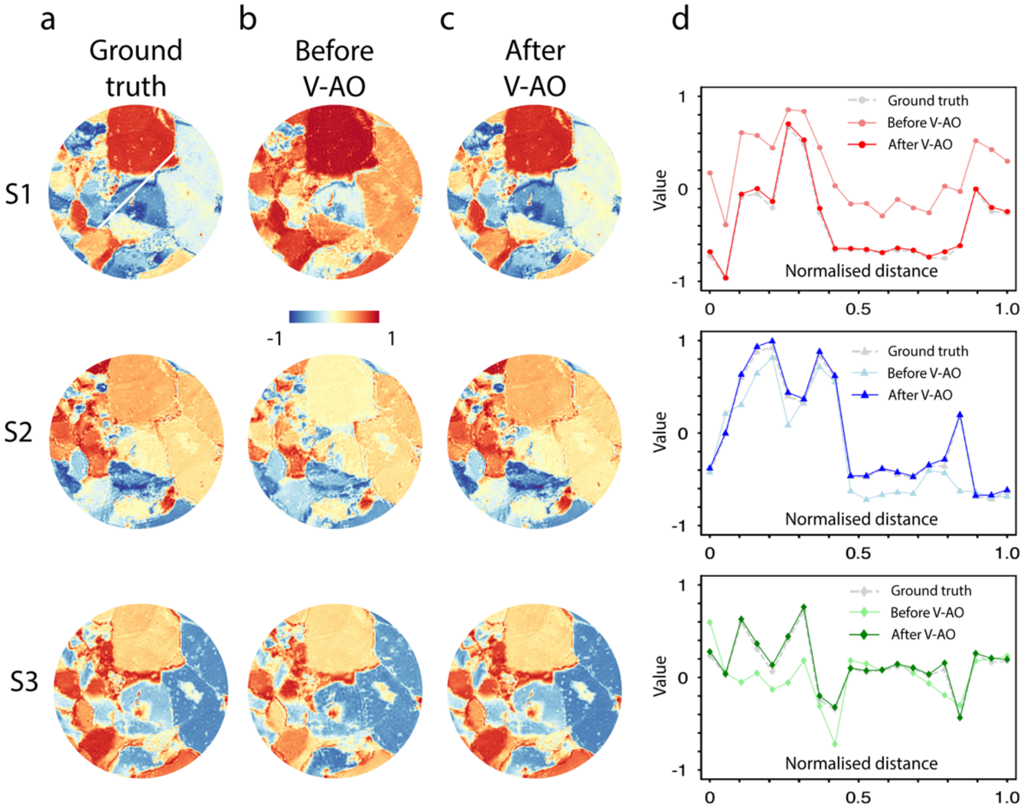

Figure 5.14: Stokes parameter fields evaluation of V-AO correction performance in archaeological sample. Stokes parameter fields and numerical analyses of archaeological sample. The Stokes parameters for (a) ground truth, (b) before V-AO correction under a moderate diattenuation ($E = 1.65$) and (c) after V-AO correction are illustrated; (d) evaluates the V-AO correction performance by plotting the values of each Stokes parameter along a selected cross-section.

To further demonstrate the effectiveness of V-AO correction under diattenuation aberrations, we present an additional quantitative comparison in Fig. 5.14 and 5.15. For both the archaeological and biomedical samples, the three Stokes vector components S_1, S_2, S_3 are visualised under three conditions: 1) ground truth; 2) before V-AO correction under a moderate diattenuation ($E = 1.65$); 3) after V-AO correction. For each component, the value profile along the selected cross-section is presented. The close match between the V-AO corrected and ground-truth curves confirms the effectiveness of V-AO in restoring the polarisation field in the presence of diattenuations aberrations, enabling robust measurements in complex environments.

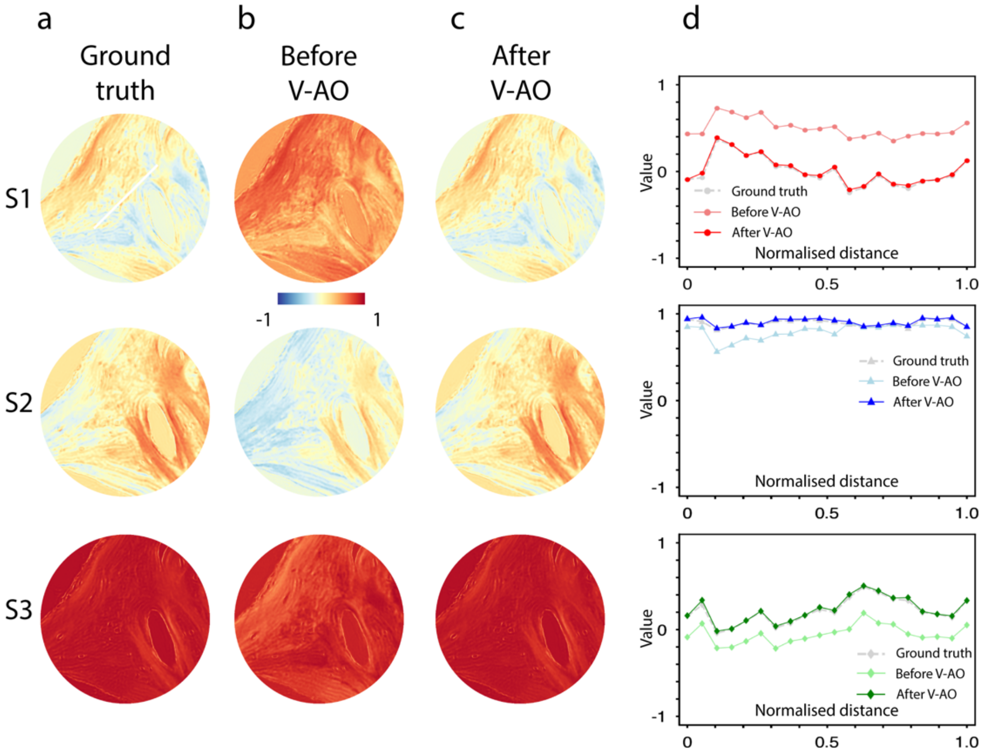

Figure 5.15: Stokes parameter fields evaluation of V-AO correction performance in biomedical sample (bone marrow). Stokes parameter fields and numerical analyses of biomedical sample. The layout, definitions and analysis are identical to Fig. 5.14.

These results illustrate that, once the correction boundary of V-AO is understood, our pixelated V-AO architecture can effectively achieve aberration correction, demonstrating potential to real-world imaging scenarios where SoP fidelity is required – such as in complex or spatially varying samples affected by diattenuation.

5.4.2 Stokes polarimetric imaging under diattenuation aberration

As an extension of V-AO beyond traditional correction, the SN is further considered as an indicator of the performance of polarimetric imaging under diattenuation, particularly by guiding the selection of optimal measurement configurations, with V-AO implemented in the analysing arm to control the detection states. For Stokes vector polarimetry, the configuration typically involves a PSA, whereas Mueller matrix polarimetry setups incorporate a PSG and a PSA. A minimum of N ($N = 4$ for Stokes vector, 16 for Mueller matrix) independent SoPs is required to reconstruct the polarisation information. The optimisation approaches for both PSG and PSA in measurement process are analogous[142]. In the following section, the PSA is analysed as a representative case study

To evaluate the performance of the PSA module, various metrics have been introduced, including condition number (CN)[157], equally weighted variance (EWV)[158] and Poincaré sphere internal volume (PSIV)[159,160]. Geometrically, the independent analysing SoPs define a polyhedron within the PS. Azzam et al.[159,160] proposed that the optimal set of analysing SoPs is achieved when this inscribed polyhedron reaches its maximum volume.

The superiority of any particular optimisation method is not claimed here; the PSIV approach is adopted here to demonstrate our analysis, but similar methodology can be applied using other metrics. For illustrative purposes, we consider N=4. The four independent SoPs serve as the vertices to construct a tetrahedron within the PS. The maximal volume is achieved when the configuration forms a regular tetrahedron, as illustrated in Fig 5.15. Previous demonstration shows that applying an intensity filter leads to an exclusion of certain SoPs, visually represented by a spherical cap. According to the geometric relationship, it is intuitive that the integrity of the regular tetrahedron configuration is preserved as long as the spherical cap's cross-section does not extend beyond the tetrahedron's base.

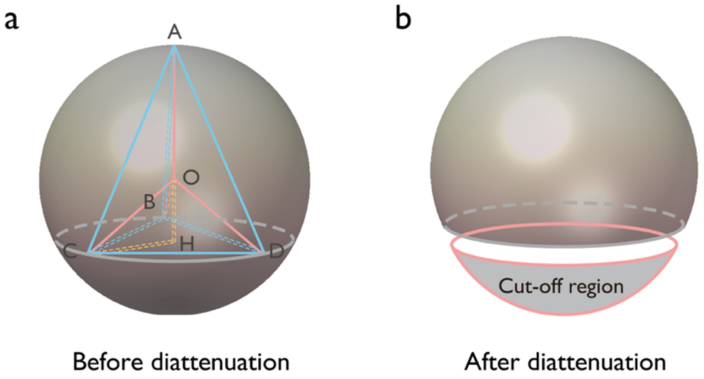

Figure 5.16: Geometrical visualisation of maximum tolerance of diattenuation aberration for optimal Stokes vector measurement. (a) Before diattenuation, an inscribed regular tetrahedron in PS defined by four optimal SoPs at vertices A, B, C and D. Point O represents the central point of the sphere, point H denotes the central point of the tetrahedron’s base. (b) After diattenuation, the filtered output field covers a spherical cap (the grey region) in the PS surface, the radius of its cross section is related to the intensity filter value F.

The maximum tolerance of diattenuation is mathematically determined here using geometric arguments. Consider a sphere with radius r and an inscribed regular tetrahedron with edge length a, where $AO = r, AC = a$. From the geometry, we have $r = \frac{\sqrt{6}}{4}a$, $OH = \frac{\sqrt{6}}{12}a$, $\frac{OH}{OC} = \frac{1}{3}$.

The surface area enclosed by the cone with vertices O, B, C and D can be calculated through surface integral:

$$S = \int_{\varphi=0}^{\varphi'} \int_{\theta=0}^{\theta=2\pi} R^2 sin^2\varphi d\varphi d\theta = 2\pi R^2 \tag{5.30}$$

where $cos\,\varphi' = \frac{1}{3}$, the maximal reduced superficial area can be quantified as $\frac{4}{3}\pi R^2$. We reach the boundary when $R = \frac{\sqrt{8}}{3}r$, then we have:

$$9\sin^2 2\gamma = 16 + 16(2F - 1) + \tan^2 2\gamma(2F - 1)^2 \tag{5.31}$$

where γ represents the extinction ratio, F denotes the intensity threshold. Then for a given intensity filter value F, we can deduce the boundary of diattenuation that maintains the optimal SoPs. Furthermore, the SN corresponding to the boundary diattenuation can also be calculated. Therefore, whenever the resulting SN remains within this limit, the system can operate optimally.

When E increases and exceeds this boundary, the optimal configuration is compromised. However, it remains feasible to find four SoPs that maximise the volume of inscribed tetrahedron within the deficient PS. The related output SN provides an indication of the optimal performance this system can achieve under such a diattenuation.

5.4.3 SN assisted V-AO for Stokes polarimetric imaging

To demonstrate how SN serves as a practical indicator for guiding V-AO correction for optimal Stokes polarimetric imaging, five representative cases are illustrated in Fig. 5.17: two within the boundary (a and b), one on the boundary (c), and two beyond it (d and e). For each case, both the residual region on the PS and the largest inscribable tetrahedron (representing optimised measurement states) are shown.

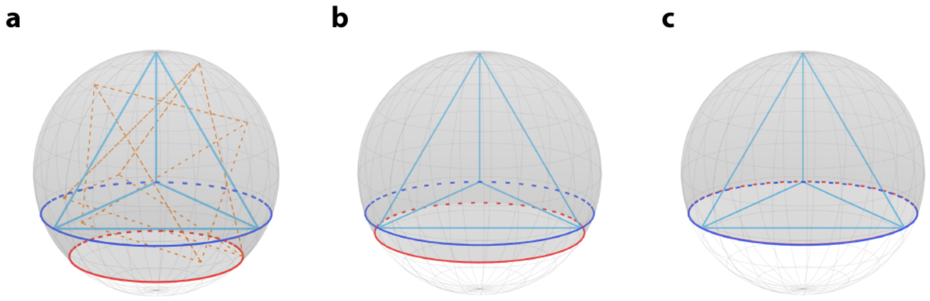

SN=0.90
Diattenuation within
tolerance boundary

SN=0.80
Diattenuation within
tolerance boundary

SN=0.67
Diattenuation at
tolerance boundary

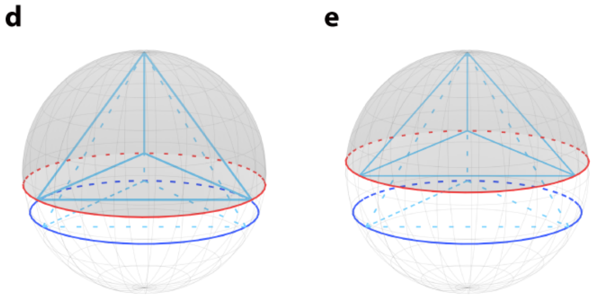

SN=0.50
Diattenuation beyond
tolerance boundary

SN=0.40
Diattenuation beyond
tolerance boundary

Figure 5.17: Optimal analysing SoPs for Stokes vector measurement under different diattenuation cases. (a)-(b): diattenuation values within the tolerance boundary, the dashed orange outline shows rotated yet equivalent optimal tetrahedrons; (c): diattenuation value at the tolerance boundary; (d)-(e): diattenuation values beyond the tolerance boundary. Both the remaining portion of the sphere and the largest tetrahedron that can be inscribed in each case are illustrated.

For diattenuation levels within the tolerance boundary (a-c), the accessible surface on the PS is sufficiently large to accommodate a full regular tetrahedron. Under these conditions, the original four analysing SoPs – and therefore the existing SLM phase settings – already support optimal measurement. For diattenuation levels beyond the tolerance boundary (d and e), if we aim to optimise the measurement states via V-AO in analysing arm (by controlling the SLM parameters), then the four analysing SoP points of the SN-linked tetrahedron (representing four optimised states) need to be realised by the SLMs' retardance settings. In this way, SN provides a clear and quantitative link with V-AO system, offering a practical metric for system optimisation – through SLM parameter control – even beyond ideal conditions.

It is also worth noting that in all cases a family of equivalent optimal SoPs exists, because the tetrahedron can be freely rotated about the sphere (as shown in Fig. 5.17 (a)). This rotational freedom gives the control algorithm flexibility to choose whichever set of four SoPs is most convenient for implementation.

While this section demonstrates the use of SN to guide V-AO correction towards optimal Stokes polarimetric imaging, the underlying principle holds potential for broader applications in more complex measurement scenarios. For instance, extending the current methodology from uniform to spatially variant diattenuation profiles could enable corrections in increasingly realistic environments. Furthermore, systematically investigating how the spatial placement of vectorial aberrations impacts both polarisation generation and detection, as well as exploring the potential of SN as a versatile indicator for system robustness, calibration, or adaptive control, presents intriguing avenues for future research.

5.5 Summary and discussion

In this chapter, a vectorial structured light field – *Néel-type* skyrmionic beam – is used to evaluate quantitatively the correction ability of V-AO in the presence of non-depolarising aberrations. The limit of AO system is not solely determined by the dynamic range and configuration of the AO devices but is significantly influenced by the inherent properties of the aberrations. Specifically, the intensity loss and polarisation changes induced by diattenuation play a crucial role in defining the correctability boundaries of the system, taking the camera's sensitivity into consideration.

Attention was focused on pre-correction of diattenuation aberration, where the correction ability is related to the intrinsic properties of diattenuation itself. The results led to an interesting observation that, for a determined diattenuation aberration, certain pre-correction of the SoPs can still be beneficial – i.e., if the desired SoP can be achieved in the output Stokes vector field, then this state can be produced through correction modules. Hence for several important applications, such as polarisation microscopy that suffers from diattenuation aberrations, V-AO may still take on a pre-correction geometry and provide the required performance. Furthermore, by analysing the properties of vectorial aberration, the maximum level of diattenuation aberration that can be corrected via AO to maintain the optimal performance of a Stokes vector/Mueller matrix microscope was also derived.

There are intriguing areas to be further explored:

1) In real-world applications, such analysis provides a standard for determining appropriate correction strategies. For example, in scenarios where the aberration is beyond the AO correction boundary, current optimal solutions of the system may be unable to correct the aberrated field, and other compensation strategies, such as passive or hybrid compensation methods, may be needed.

2) From the SN-assisted V-AO correction experiments, we found an interesting "duality": the V-AO module, while targeting compensation of vectorial errors within its capacity, in effect also dynamically optimises polarimetric imaging performance via optimal channels under existing conditions. There remains intriguing scope for future exploration of such properties in both theoretical and experimental analysis.

3) Besides *Néel-type* skyrmionic beams, other types of complex skyrmionic beams may also be used to optimally sense different diattenuation profiles. Hence, future studies can thus extend our methodology by exploring various optical skyrmion textures, investigating how each of them responds to distinct diattenuation patterns and/or optimising the beam design accordingly. Such expansions will not only enhance the versatility of our technique but also provide more refined correction strategies for different aberrated scenarios.

Overall, this chapter introduce a new usage of complex skyrmionic beams, as well as fundamental probing methodologies in next-generation V-AO. The potential applications of this work span from AO-enhanced sensing/imaging techniques to biomedical/material applications, and importantly, represent a first step towards interdisciplinary research integrating optical skyrmions, AO, sample information analysis/characterisation, as well as polarimetric measurements.

Chapter 6 Conclusion and future work

6.1 Conclusion

This thesis has expanded AO from a phase-only technique to a higher-dimensional framework and then realised its vectorial core in practice. The work firstly began by integrating a V-AO correction module into a widefield Stokes polarimetric microscope, where a pupil intensity metric guided the correction of spatially varying retardance. Two evaluation criteria – precision and uniformity – were introduced, and the substantial improvements achieved in both demonstrated the effectiveness of V-AO correction (Chapter 3).

To circumvent the complex field conversion process required in vectorial aberration correction operation, the concept of O-AO (another type of V-AO) was introduced. By cascading four modulators (three SLMs and a DM in this thesis), a pixel-tunable arbitrary-retarder array was realised. It can be programmed to implement the inverse Jones/Mueller matrix of the aberration for direct compensation. Both sensor-based and sensor-less optimisation restored the focus spot under complex vectorial aberrations (Chapter 4).

Building on the demonstrated correction of phase and retardance aberrations, the correction ability of V-AO to address diattenuation was explored. Unlike phase or retardance, diattenuation redistributes energy between different SoPs and reduces the total intensity, effectively compressing the Stokes vector toward the diattenuators' transmission axis. In practice, the camera's noise level and dynamic range then impose a correctability limit: certain SoPs become indistinguishable or even unreachable, so vectorial recovery cannot be guaranteed. This motivates a quantitative assessment of when and how V-AO can still succeed under diattenuation. Optical skyrmionic beams were used to probe diattenuation-aberrated systems and provide metrics that characterise the performance of V-AO, with both theoretical and experimental validations. Based on the probed results, V-AO correction ability under real-world aberrated conditions for complex media imaging was demonstrated and the correction strategies to optimise measurements in aberrated polarimetric systems were also analysed (Chapter 5). Together these contributions demonstrate that V-AO can be configured across diverse architectures and applications, establishing the vectorial foundation of the unified high-dimensional AO framework.

6.2 Future work

This section outlines future research directions that naturally follow from this thesis. Looking beyond the vectorial emphasis demonstrated here, the goal is a unified high-dimensional AO toolbox that addresses phase, polarisation (retardance and diattenuation), intensity error, and further combined with depolarisation. Two complementary tracks are proposed: 1) high-dimensional AO methodology – advancing devices and optimisation/control algorithms for joint sensing and correction; 2) applications – deploying and validating high-dimensional AO across representative practical applications.

6.2.1 Methodological advances towards high-dimensional AO

6.2.1.1 Towards depolarisation adaptive optics (D-AO)

This thesis has focused on non-depolarising media. A natural next step is to extend the framework to depolarisation correction, completing the move toward high-dimensional AO. Conceptually, D-AO is a specialised modality within the V-AO framework: it retains an explicit DoP control channel. In many practical scenes – e.g., thick tissues, fibrous or heterogeneous materials – multiple scattering[161,162], sub-resolution anisotropy[48,163], and temporal fluctuations scramble the field and convert a portion of fully polarised light into an unpolarised component[11,164]. The resulting drop in DoP degrades polarimetric contrast and biases Stokes/Mueller retrievals, even when phase and retardance have been corrected.

A D-AO module would add active DoP control to the field. A practical route might be achieved by synthesising a controllable depolariser with pixel-addressable retarders: alternate two retardance states ϕ_A and ϕ_B at a rate faster than the detector integration time (or interleave them spatially within the detector pixel), so that the detector measures the averaged Mueller response. Because both states are non-diattenuating, the effective matrix is depolarising without diattenuation. In the Lu–Chipman decomposition method, this average is equivalent to a depolariser cascaded with a pure retarder (for an isotropic depolariser the order does not matter). Thus, by tuning the duty cycle between the two retardance states, we in effect realise a tuneable depolariser without adding extra optics.

The correction operation might be then proceeded in two modes: 1) sensor-based D-AO, where a Mueller polarimeter provides per-pixel DoP maps to drive the modulators; 2) quasi-sensorless D-AO, where a PSA provides DoP proxies (e.g., analyser pairs or compact DoP meters) that guide metric-based optimisation. Implementation could possibly be achieved via the cascade of SLMs or upgrade to faster, compact devices, such as electro-optic or metasurface based devices, that provided the modulation rate exceeds the detector's temporal averaging. Integrating this DoP channel with existing phase/retardance/diattenuation correction may yield a unified high-dimensional AO toolbox capable of maintaining image fidelity and polarimetric accuracy even in partially depolarising scenes.

6.2.1.2 Towards joint sensing and correction in four dimensions

Having established D-AO as another important part alongside phase, retardance and diattenuation control, the next step is planned to achieve a unified high-dimensional AO that treats intensity, phase, SoP, DoP as a coupled state to be sensed and corrected jointly.

On the sensing side, a practical route might be a compact, multi-dimensional sensor that multiplexes several analyser states onto a single camera exposure. One snapshot could then illustrate a pupil-resolved estimate of intensity, scalar phase, Stokes parameters (hence SoP and DoP), and simple diattenuation, providing exactly the multi-channel state required by high-dimensional AO.

On the correction side, the goal could be obtaining a unified, pixel-addressable field that phase, retardance, diattenuation and effective depolarisation can be simultaneously manipulated. In the near term this can be realised by cascading pixelated-controlled modulators such as SLMs[13]; longer-term, integrated electro-optic or metasurface devices[113] should provide the same degrees of freedom with higher efficiency and speed.

The correction implementation could be developed as follows: a sensor-based mode that deliver the joint measurements directly to a multi-objective controller (e.g. driving towards flat phase, uniform SoP, prescribed DoP and adequate intensity level under hardware constraints); while a quasi-sensorless mode replaces explicit measurements with higher-dimensional metrics and employs learning-based models to minimise the number of acquisitions[165–169]. In parallel, high-dimensional control bases – spanning coupled phase, retardance, intensity and DoP modes – can be developed to improve conditioning and convergence. Together, a multi-dimensional sensor and an integrated vectorial corrector would complete the transition to four-dimensional AO, enabling snapshot estimation and fast compensation in practical optical imaging systems. Looking ahead, the hardware might follow two tracks: 1) open-path module that utilises pixelated modulators for temporal mixing; and 2) compact/integrated unit. This may exploit techniques such as patterned liquid-crystal optics, reconfigurable metasurfaces, or thin-film electro-optic platforms to enable sensing and correction – and, ultimately, migrate four-dimensional AO toward an on-chip form factor.

6.2.2 Application expansion of high-dimensional AO framework

Direct laser writing (DLW) – particularly two-photon polymerisation – forms 3D micro/nanostructures by delivering a tightly focused, high-intensity spot whose dose sets the voxel size and shape. Polarisation is frequently exploited to control feature orientation, while prior AO assistance has mainly targeted scalar phase to restore diffraction-limited focusing[97].

In practice, however, DLW performance is limited by additional aberration dimensions beyond phase. Multi-spot techniques suffer from intensity non-uniformity across the focal array, and even single-spot systems inherit the throughput variations across the field[170–172]. At the same time, high-NA focusing, and thick or weakly scattering substrates introduce vectorial distortions[173]. The resulting mismatch between the intended and realised vectorial field perturbs the focal point-spread function (PSF) – with depth-dependent asymmetry, broadened cores and sidelobe growth – so the delivered dose may drift with depth, ultimately lowering write fidelity.

High-dimensional AO approaches could possibly address these coupled limitations by jointly sensing and correcting the relevant aberrations. The correction operation may follow either the sensor-based workflow (using the joint maps directly); or a quasi-sensorless workflow that replaces explicit measurements with fabrication-relevant metrics accelerated by learning-based optimisation. By stabilising dose and the vectorial field simultaneously, high-dimensional AO could be expected to tighten voxel distributions, improve multi-spot uniformity and stitching, thus extending DLW toward faster, larger-area, and higher-fidelity fabrication.

Beyond DLW techniques, the same high-dimensional AO framework could be possibly extended to various research areas. For instance, 1) in correction scenarios where system and sample-induced errors drift slowly over time, such as confocal and multiphoton microscopes, saturated depletion optical microscopy (SDOM)[174] and structured illumination microscopy (SIM)[175], polarisation-resolved nonlinear imaging[176] and high-NA lithography scanners[177], joint sensing and correction deliver the desired phase, intensity, SoP and DoP across the field, tightening the PSF, improving contrast, and reducing stitching and quantitative bias; 2) In dynamic settings, where aberrations vary rapidly due to, for example, atmospheric turbulence in astronomy, motion and refractive-index fluctuations in in-vivo/live-cell imaging, or scintillation and depolarisation in free-space optical communications, passive calibration is insufficient. High-dimensional AO may provide insight on real time joint correction.

Taken together, high-dimensional AO framework could contribute to push systems or instruments closer to their physical limits, delivering more robust, reproducible vectorial measurements and higher throughput across laboratory and industry applications.

Reference:

1. Booth, M. J. Adaptive optical microscopy: the ongoing quest for a perfect image. *Light Sci Appl* 3, e165–e165 (2014).
2. Booth, M. J. Adaptive optics in microscopy. *Philosophical Transactions of the Royal Society A: Mathematical, Physical and Engineering Sciences* 365, 2829–2843 (2007).
3. Girkin, J. M., Poland, S. & Wright, A. J. Adaptive optics for deeper imaging of biological samples. *Curr Opin Biotechnol* 20, 106–110 (2009).
4. Ji, N. Adaptive optical fluorescence microscopy. *Nat Methods* 14, 374–380 (2017).
5. Babcock, H. W. The possibility of compensating astronomical seeing. *Publications of the Astronomical Society of the Pacific* 65, 229–236 (1953).
6. Tyson, R. K. & Frazier, B. W. *Principles of Adaptive Optics*. (CRC press, 2022).
7. Berry, M. Pancharatnam, virtuoso of the Poincaré sphere: an appreciation. *Curr Sci* 67, 220–223 (1994).
8. De Zela, F. The Pancharatnam-Berry phase: Theoretical and experimental aspects. *Theoretical concepts of quantum mechanics* 289–312 (2012).
9. Berry, M. V. The adiabatic phase and Pancharatnam's phase for polarized light. *J Mod Opt* 34, 1401–1407 (1987).
10. Zhao†, Z. *et al.* Intensity adaptive optics. *Light Sci Appl* 14, 128 (2025).

11. Marco, D. *et al.* Customized depolarization spatial patterns with dynamic retardance functions. *Sci Rep* 11, 9415 (2021).

12. He, C., Antonello, J. & Booth, M. J. Vectorial adaptive optics. *eLight* 3, 23 (2023).

13. He, C. *et al.* A reconfigurable arbitrary retarder array as complex structured matter. *Nat Commun* 16, 4902 (2025).

14. Azzam, R. M. A. Mueller-matrix ellipsometry: a review. *Polarization: Measurement, Analysis, and Remote Sensing* 3121, 396–405 (1997).

15. Pezzaniti, J. L. & Chipman, R. A. Mueller matrix imaging polarimetry. *Optical engineering* 34, 1558–1568 (1995).

16. Fan, J. *et al.* Stain transformation using Mueller matrix guided generative adversarial networks. *Opt Lett* 49, 5135–5138 (2024).

17. Arteaga, O., Freudenthal, J., Wang, B. & Kahr, B. Mueller matrix polarimetry with four photoelastic modulators: theory and calibration. *Appl Opt* 51, 6805–6817 (2012).

18. Smith, M. H. Optimization of a dual-rotating-retarder Mueller matrix polarimeter. *Appl Opt* 41, 2488–2493 (2002).

19. Du, E. *et al.* Mueller matrix polarimetry for differentiating characteristic features of cancerous tissues. *J Biomed Opt* 19, 076013 (2014).

20. Born, M. & Wolf, E. *Principles of Optics: Electromagnetic Theory of Propagation, Interference and Diffraction of Light*. (Elsevier, 2013).

21. Rubinsztein-Dunlop, H. *et al.* Roadmap on structured light. *Journal of Optics* 19, 013001 (2016).
22. Zhan, Q. Cylindrical vector beams: from mathematical concepts to applications. *Adv Opt Photonics* 1, 1–57 (2009).
23. Konnen, G. P. *Polarized Light in Nature*. (CUP Archive, 1985).
24. Shurcliff, W. A. *Polarized Light: Production and Use*. (Harvard University Press, 1962).
25. Chipman, R., Lam, W. S. T. & Young, G. *Polarized Light and Optical Systems*. (CRC press, 2018).
26. Kliger, D. S. & Lewis, J. W. *Polarized Light in Optics and Spectroscopy*. (Elsevier, 2012).
27. Tuchin, V. V. Tissue optics. in (Society of Photo-Optical Instrumentation Engineers (SPIE) Bellingham, WA, USA, 2015).
28. Goldstein, D. H. *Polarized Light*. (CRC press, 2017).
29. Chipman, R., Lam, W. S. T. & Young, G. *Polarized Light and Optical Systems*. (CRC press, 2018).
30. Bass, M. *Handbook of Optics: Volume I-Geometrical and Physical Optics, Polarized Light, Components and Instruments*. (McGraw-Hill Education, 2010).
31. Singh, K., Tabebordbar, N., Forbes, A. & Dudley, A. Digital Stokes polarimetry and its application to structured light: tutorial. *Journal of the Optical Society of America A* 37, C33–C44 (2020).

32. Samim, M., Krouglov, S. & Barzda, V. Nonlinear Stokes-Mueller polarimetry. *Phys Rev A (Coll Park)* 93, 013847 (2016).

33. Ahmad, J. E. & Takakura, Y. Error analysis for rotating active Stokes-Mueller imaging polarimeters. *Opt Lett* 31, 2858–2860 (2006).

34. Skumanich, A., Lites, B. W., Pillet, V. M. & Seagraves, P. The calibration of the advanced stokes polarimeter. *Astrophys J Suppl Ser* 110, 357 (1997).

35. He, C. *et al.* Linear polarization optimized Stokes polarimeter based on four-quadrant detector. *Appl Opt* 54, 4458–4463 (2015).

36. Hsu, W.-L. *et al.* Full-Stokes imaging polarimeter using an array of elliptical polarizer. *Opt Express* 22, 3063–3074 (2014).

37. Gil, J. J. Review on Mueller matrix algebra for the analysis of polarimetric measurements. *J Appl Remote Sens* 8, 81599 (2014).

38. Baba, J. S., Chung, J.-R., DeLaughter, A. H., Cameron, B. D. & Cote, G. L. Development and calibration of an automated Mueller matrix polarization imaging system. *J Biomed Opt* 7, 341–349 (2002).

39. Gil, J. J. Characteristic properties of Mueller matrices. *Journal of the Optical Society of America A* 17, 328–334 (2000).

40. Smith, M. H. Interpreting Mueller matrix images of tissues. in *Laser-tissue interaction XII: Photochemical, photothermal, and photomechanical* vol. 4257 82–89 (SPIE, 2001).

41. Gil, J. J. & Ossikovski, R. *Polarized Light and the Mueller Matrix Approach*. (CRC press, 2022).
42. Goldstein, D. H. & Chipman, R. A. Error analysis of a Mueller matrix polarimeter. *JOSA A* 7, 693–700 (1990).
43. Azzam, R. M. A. Photopolarimetric measurement of the Mueller matrix by Fourier analysis of a single detected signal. *Opt Lett* 2, 148–150 (1978).
44. Zhou, J., He, H., Chen, Z., Wang, Y. & Ma, H. Modulus design multiwavelength polarization microscope for transmission Mueller matrix imaging. *J Biomed Opt* 23, 16007 (2018).
45. Smith, M. H. Optimization of a dual-rotating-retarder Mueller matrix polarimeter. *Appl Opt* 41, 2488–2493 (2002).
46. Goldstein, D. H. Mueller matrix dual-rotating retarder polarimeter. *Appl Opt* 31, 6676–6683 (1992).
47. Pust, N. J. & Shaw, J. A. Dual-field imaging polarimeter using liquid crystal variable retarders. *Appl Opt* 45, 5470–5478 (2006).
48. He, C. *et al.* Polarisation optics for biomedical and clinical applications: a review. *Light Sci Appl* 10, 194 (2021).
49. Gao, S. & Gruev, V. Gradient-based interpolation method for division-of-focal-plane polarimeters. *Opt Express* 21, 1137–1151 (2013).

50. Pezzaniti, J. L. & Chenault, D. B. A division of aperture MWIR imaging polarimeter. in *Polarization Science and Remote Sensing II* vol. 5888 239–250 (Spie, 2005).

51. Bhandari, P., Voss, K. J. & Logan, L. An instrument to measure the downwelling polarized radiance distribution in the ocean. *Opt Express* 19, 17609–17620 (2011).

52. Chang, J., Zeng, N., He, H., He, Y. & Ma, H. Single-shot spatially modulated Stokes polarimeter based on a GRIN lens. *Opt Lett* 39, 2656–2659 (2014).

53. Hsu, W.-L. *et al.* Polarization microscope using a near infrared full-Stokes imaging polarimeter. *Opt Express* 23, 4357–4368 (2015).

54. Zhang, Z. *et al.* Nano-fabricated pixelated micropolarizer array for visible imaging polarimetry. *Review of scientific instruments* 85, (2014).

55. Gao, S. & Gruev, V. Bilinear and bicubic interpolation methods for division of focal plane polarimeters. *Opt Express* 19, 26161–26173 (2011).

56. Zimmerman, B. G., Ramkhalawon, R., Alonso, M. & Brown, T. G. Pinhole array implementation of star test polarimetry. in *Three-Dimensional and Multidimensional Microscopy: Image Acquisition and Processing XXI* vol. 8949 164–173 (SPIE, 2014).

57. Heredero, R. L. *et al.* Liquid-crystal variable retarders for aerospace polarimetry applications. *Appl Opt* 46, 689–698 (2007).

58. Bueno, J. M. Polarimetry using liquid-crystal variable retarders: theory and calibration. *Journal of Optics A: Pure and Applied Optics* 2, 216 (2000).

59. Hornbeck, L. J. Deformable-mirror spatial light modulators. in *Spatial Light Modulators and Applications III* vol. 1150 86–103 (Spie, 1990).

60. Madec, P.-Y. Overview of deformable mirror technologies for adaptive optics and astronomy. in *Adaptive optics systems III* vol. 8447 22–39 (SPIE, 2012).

61. Zou, W., Qi, X. & Burns, S. A. Wavefront-aberration sorting and correction for a dual-deformable-mirror adaptive-optics system. *Opt Lett* 33, 2602–2604 (2008).

62. Perreault, J. A., Bifano, T. G., Levine, B. M. & Horenstein, M. N. Adaptive optic correction using microelectromechanical deformable mirrors. *Optical Engineering* 41, 561–566 (2002).

63. Bold, G. T., Barnes, T. H., Gourlay, J., Sharples, R. M. & Haskell, T. G. Practical issues for the use of liquid crystal spatial light modulators in adaptive optics. *Opt Commun* 148, 323–330 (1998).

64. Fisher, A. D. A review of spatial light modulators. *Optical Computing* TuC1 (1985).

65. Yao, K., Wang, J., Liu, X. & Liu, W. Closed-loop adaptive optics system with a single liquid crystal spatial light modulator. *Opt Express* 22, 17216–17226 (2014).

66. Ren, Y., Lu, R. & Gong, L. Tailoring light with a digital micromirror device. *Ann Phys* 527, 447–470 (2015).

67. Qiao, L. *et al.* Designing transparent piezoelectric metasurfaces for adaptive optics. *Nat Commun* 15, 805 (2024).

68. Marsh, P. N., Burns, D. & Girkin, J. M. Practical implementation of adaptive optics in multiphoton microscopy. *Opt Express* 11, 1123–1130 (2003).

69. Žurauskas, M. *et al.* IsoSense: frequency enhanced sensorless adaptive optics through structured illumination. *Optica* 6, 370–379 (2019).

70. Débarre, D. *et al.* Image-based adaptive optics for two-photon microscopy. *Opt Lett* 34, 2495–2497 (2009).

71. Hampson, K. M. *et al.* Adaptive optics for high-resolution imaging. *Nature Reviews Methods Primers* 1, 68 (2021).

72. Lane, R. G. & Tallon, M. Wave-front reconstruction using a Shack–Hartmann sensor. *Appl Opt* 31, 6902–6908 (1992).

73. Neal, D. R., Copland, J. & Neal, D. A. Shack-Hartmann wavefront sensor precision and accuracy. in *Advanced Characterization Techniques for Optical, Semiconductor, and Data Storage Components* vol. 4779 148–160 (SPIE, 2002).

74. Seifert, L., Liesener, J. & Tiziani, H. J. The adaptive shack–hartmann sensor. *Opt Commun* 216, 313–319 (2003).

75. Platt, B. C. & Shack, R. History and principles of Shack-Hartmann wavefront sensing. *Journal of refractive surgery* vol. 17 S573–S577 Preprint at (2001).

76. Booth, M. J., Neil, M. A. A., Juškaitis, R. & Wilson, T. Adaptive aberration correction in a confocal microscope. *Proceedings of the National Academy of Sciences* 99, 5788–5792 (2002).

77. Facomprez, A., Beaurepaire, E. & Débarre, D. Accuracy of correction in modal sensorless adaptive optics. *Opt Express* 20, 2598–2612 (2012).

78. Booth, M. J. Wavefront sensorless adaptive optics for large aberrations. *Opt Lett* 32, 5–7 (2006).

79. Adkins, S. M., Azucena, O. & Nelson, J. E. The design and optimization of detectors for adaptive optics wavefront sensing. in *Advances in Adaptive Optics II* vol. 6272 452–463 (SPIE, 2006).

80. Johnston, D. C. & Welsh, B. M. Analysis of multiconjugate adaptive optics. *Journal of the Optical Society of America A* 11, 394–408 (1994).

81. Wang, C. *et al.* Wavefront detection method of a single-sensor based adaptive optics system. *Opt Express* 23, 21403–21413 (2015).

82. Chew, T. Y. Wavefront sensors in adaptive optics. (2008).

83. Niu, K. & Tian, C. Zernike polynomials and their applications. *Journal of Optics* 24, 123001 (2022).

84. McAlinden, C., McCartney, M. & Moore, J. Mathematics of Zernike polynomials: a review. *Clin Exp Ophthalmol* 39, 820–827 (2011).

85. Noll, R. J. Zernike polynomials and atmospheric turbulence. *J Opt Soc Am* 66, 207–211 (1976).

86. Jian, Y. *et al.* Wavefront sensorless adaptive optics optical coherence tomography for in vivo retinal imaging in mice. *Biomed Opt Express* 5, 547–559 (2014).

87. Booth, M. J. Wave front sensor-less adaptive optics: a model-based approach using sphere packings. *Opt Express* 14, 1339–1352 (2006).

88. Linhai, H. & Rao, C. Wavefront sensorless adaptive optics: a general model-based approach. *Opt Express* 19, 371–379 (2010).

89. Skorsetz, M., Artal, P. & Bueno, J. M. Performance evaluation of a sensorless adaptive optics multiphoton microscope. *J Microsc* 261, 249–258 (2016).

90. Booth, M. J., Neil, M. A. A. & Wilson, T. Aberration correction for confocal imaging in refractive-index-mismatched media. *J Microsc* 192, 90–98 (1998).

91. Jesacher, A. & Booth, M. J. Sensorless adaptive optics for microscopy. in *MEMS Adaptive Optics V* vol. 7931 115–123 (SPIE, 2011).

92. Dai, Y. *et al.* Active compensation of extrinsic polarization errors using adaptive optics. *Opt Express* 27, 35797–35810 (2019).

93. Berry, M. V. The adiabatic phase and Pancharatnam's phase for polarized light. *J Mod Opt* 34, 1401–1407 (1987).

94. He, C., Antonello, J. & Booth, M. J. Vectorial adaptive optics. *eLight* 3, 23 (2023).

95. He, C. & Booth, M. J. Improvement of Resolution and Polarisation Measurement Precision in Biomedical Imaging Through Adaptive Optics. in *Polarized Light in*

Biomedical Imaging and Sensing: Clinical and Preclinical Applications 345–360 (Springer, 2022).

96. He, C. *et al.* Complex vectorial optics through gradient index lens cascades. *Nat Commun* 10, 1–8 (2019).

97. Salter, P. S. & Booth, M. J. Adaptive optics in laser processing. *Light Sci Appl* 8, 1–16 (2019).

98. Hu, Q., Dai, Y., He, C. & Booth, M. J. Arbitrary vectorial state conversion using liquid crystal spatial light modulators. *Opt Commun* 459, 125028 (2020).

99. Hu, Q., He, C. & Booth, M. J. Arbitrary complex retarders using a sequence of spatial light modulators as the basis for adaptive polarisation compensation. *Journal of Optics* 23, 065602 (2021).

100. Kenny, F., Lara, D., Rodríguez-Herrera, O. G. & Dainty, C. Complete polarization and phase control for focus-shaping in high-NA microscopy. *Opt Express* 20, 14015–14029 (2012).

101. Shribak, M. I., Inoue, S. & Oldenbourg, R. Polarization aberrations caused by differential transmission and phase shift in high numerical aperture lenses: theory, measurement, and retification. *Optical Engineering* 41, 943–954 (2002).

102. Zhang, Q. & Gu, M. Vectorial adaptive optics: expanding the frontiers of optical correction. *Light Sci Appl* 13, 32 (2024).

103. He, C., Antonello, J. & Booth, M. J. Vectorial adaptive optics. *eLight* 3, 23 (2023).

104. Ma, Y., Zhao, Z., Cui, J., Wang, J. & He, C. Vectorial adaptive optics for advanced imaging systems. *arXiv preprint arXiv:2312.05610* (2023).

105. Moreno, I., Davis, J. A., Hernandez, T. M., Cottrell, D. M. & Sand, D. Complete polarization control of light from a liquid crystal spatial light modulator. *Opt Express* 20, 364–376 (2012).

106. Davis, J. A., Evans, G. H. & Moreno, I. Polarization-multiplexed diffractive optical elements with liquid-crystal displays. *Appl Opt* 44, 4049–4052 (2005).

107. Rubin, N. A., Shi, Z. & Capasso, F. Polarization in diffractive optics and metasurfaces. *Adv Opt Photonics* 13, 836–970 (2021).

108. Han, W., Yang, Y., Cheng, W. & Zhan, Q. Vectorial optical field generator for the creation of arbitrarily complex fields. *Opt Express* 21, 20692–20706 (2013).

109. Zhong, R.-Y. *et al.* Gouy-phase-mediated propagation variations and revivals of transverse structure in vectorially structured light. *Phys Rev A (Coll Park)* 103, 053520 (2021).

110. Li, Y. *et al.* Single-exposure fabrication of tunable Pancharatnam-Berry devices using a dye-doped liquid crystal. *Opt Express* 27, 9054–9060 (2019).

111. Rong, Z.-Y., Han, Y.-J., Wang, S.-Z. & Guo, C.-S. Generation of arbitrary vector beams with cascaded liquid crystal spatial light modulators. *Opt Express* 22, 1636–1644 (2014).

112. Wang, X.-L., Ding, J., Ni, W.-J., Guo, C.-S. & Wang, H.-T. Generation of arbitrary vector beams with a spatial light modulator and a common path interferometric arrangement. *Opt Lett* 32, 3549–3551 (2007).

113. Shaltout, A. M., Shalaev, V. M. & Brongersma, M. L. Spatiotemporal light control with active metasurfaces. *Science (1979)* 364, eaat3100 (2019).

114. Sit, A., Giner, L., Karimi, E. & Lundeen, J. S. General lossless spatial polarization transformations. *Journal of Optics* 19, 094003 (2017).

115. Hu, Q., He, C. & Booth, M. J. Arbitrary complex retarders using a sequence of spatial light modulators as the basis for adaptive polarisation compensation. *Journal of Optics* 23, 065602 (2021).

116. Wang, A. A. *et al.* Topological protection of optical skyrmions through complex media. *Light Sci Appl* 13, 314 (2024).

117. Shen, Y. *et al.* Optical skyrmions and other topological quasiparticles of light. *Nat Photonics* 18, 15–25 (2024).

118. Ma, Y., Zhao, Z., Cui, J., Wang, J. & He, C. Vectorial adaptive optics for advanced imaging systems. *Journal of Optics* 26, 065402 (2024).

119. He, C. & Booth, M. J. Enhancing polarisation imaging through novel polarimetry and adaptive optics. in *Polarized Light and Optical Angular Momentum for Biomedical Diagnostics 2022* (eds. Ramella-Roman, J. C., Ma, H., Novikova, T., Elson, D. S. & Vitkin, I. A.) vol. 11963 1196302 (SPIE, 2022).

120. He, C. & Booth, M. J. Vectorial adaptive optics: correction of polarization and phase. in *Adaptive Optics and Applications* OTh3B-4 (Optica Publishing Group, 2022).

121. CHIPMAN, R. A. POLARIZATION ABERRATIONS (THIN FILMS). *ProQuest Dissertations and Theses* (United States -- Arizona, 1987).

122. Ossikovski, R. Interpretation of nondepolarizing Mueller matrices based on singular-value decomposition. *Journal of the Optical Society of America A* 25, 473–482 (2008).

123. Gil, J. J. & Ossikovski, R. *Polarized Light and the Mueller Matrix Approach*. (CRC press, 2022).

124. Skyrme, T. H. R. A non-linear field theory. *Proc R Soc Lond A Math Phys Sci* 260, 127–138 (1961).

125. Fert, A., Reyren, N. & Cros, V. Magnetic skyrmions: advances in physics and potential applications. *Nat Rev Mater* 2, 1–15 (2017).

126. Foster, D. *et al.* Two-dimensional skyrmion bags in liquid crystals and ferromagnets. *Nat Phys* 15, 655–659 (2019).

127. Król, M. *et al.* Observation of second-order meron polarization textures in optical microcavities. *Optica* 8, 255–261 (2021).

128. Donati, S. *et al.* Twist of generalized skyrmions and spin vortices in a polariton superfluid. *Proceedings of the National Academy of Sciences* 113, 14926–14931 (2016).

129. He, C., Shen, Y. & Forbes, A. Towards higher-dimensional structured light. *Light Sci Appl* 11, 205 (2022).

130. Tsesses, S. *et al.* Optical skyrmion lattice in evanescent electromagnetic fields. *Science (1979)* 361, 993–996 (2018).

131. Du, L., Yang, A., Zayats, A. V & Yuan, X. Deep-subwavelength features of photonic skyrmions in a confined electromagnetic field with orbital angular momentum. *Nat Phys* 15, 650–654 (2019).

132. Shen, Y. *et al.* Topologically controlled multiskyrmions in photonic gradient-index lenses. *Phys Rev Appl* 21, 024025 (2024).

133. Shen, Y., Martínez, E. C. & Rosales-Guzmán, C. Generation of optical skyrmions with tunable topological textures. *ACS Photonics* 9, 296–303 (2022).

134. Nape, I. *et al.* Revealing the invariance of vectorial structured light in complex media. *Nat Photonics* 16, 538–546 (2022).

135. Shen, Y. *et al.* Optical skyrmions and other topological quasiparticles of light. *Nat Photonics* 18, 15–25 (2024).

136. Wang, A. A. *et al.* Unlocking new dimensions in photonic computing using optical Skyrmions. *arXiv preprint arXiv:2407.16311* (2024).

137. Gao, S. *et al.* Paraxial skyrmionic beams. *Phys Rev A (Coll Park)* 102, 053513 (2020).

138. He, C. *et al.* Complex vectorial optics through gradient index lens cascades. *Nat Commun* 10, 4264 (2019).

139. He, C. *et al.* Revealing complex optical phenomena through vectorial metrics. *Advanced Photonics* 4, 026001 (2022).

140. He, H. *et al.* Mueller matrix polarimetry—an emerging new tool for characterizing the microstructural feature of complex biological specimen. *Journal of Lightwave Technology* 37, 2534–2548 (2019).

141. He, C. *et al.* A universal optical modulator for synthetic topologically tuneable structured matter. *arXiv e-prints* arXiv:2311.18148 (2023) doi:10.48550/arXiv.2311.18148.

142. Azzam, R. M. A. Stokes-vector and Mueller-matrix polarimetry. *JOSA A* 33, 1396–1408 (2016).

143. Shukla, P., Awasthi, A., Pandey, P. K. & Pradhan, A. Discrimination of normal and dysplasia in cervix tissue by Mueller matrix analysis. in *Biomedical Applications of Light Scattering II* vol. 6864 248–255 (SPIE, 2008).

144. He, C. *et al.* Characterizing microstructures of cancerous tissues using multispectral transformed Mueller matrix polarization parameters. *Biomed Opt Express* 6, 2934–2945 (2015).

145. Wang, Y. *et al.* Mueller matrix microscope: a quantitative tool to facilitate detections and fibrosis scorings of liver cirrhosis and cancer tissues. *J Biomed Opt* 21, 071112 (2016).

146. Dong, Y. *et al.* Quantitatively characterizing the microstructural features of breast ductal carcinoma tissues in different progression stages by Mueller matrix microscope. *Biomed Opt Express* 8, 3643–3655 (2017).

147. Chang, J. *et al.* Division of focal plane polarimeter-based 3× 4 Mueller matrix microscope: a potential tool for quick diagnosis of human carcinoma tissues. *J Biomed Opt* 21, 56002 (2016).

148. Deng, L. *et al.* A dual-modality imaging method based on polarimetry and second harmonic generation for characterization and evaluation of skin tissue structures. *Int J Mol Sci* 24, 4206 (2023).

149. Qi, J., He, C. & Elson, D. S. Real time complete Stokes polarimetric imager based on a linear polarizer array camera for tissue polarimetric imaging. *Biomed Opt Express* 8, 4933–4946 (2017).

150. He, H. *et al.* Monitoring microstructural variations of fresh skeletal muscle tissues by Mueller matrix imaging. *J Biophotonics* 10, 664–673 (2017).

151. He, C. *et al.* Quantitatively differentiating microstructures of tissues by frequency distributions of Mueller matrix images. *J Biomed Opt* 20, 105009 (2015).

152. Zhang, Z. *et al.* Analysis and optimization of aberration induced by oblique incidence for in-vivo tissue polarimetry. *Opt Lett* 48, 6136–6139 (2023).

153. Zhang, Z. *et al.* Analyzing the influence of oblique incidence on quantitative backscattering tissue polarimetry: a pilot *ex vivo* study. *J Biomed Opt* 28, 102905 (2023).

154. Chang, J. *et al.* Optimization of GRIN lens Stokes polarimeter. *Appl Opt* 54, 7424–7432 (2015).

155. Shao, C. *et al.* Analyzing the Influence of Imaging Resolution on Polarization Properties of Scattering Media Obtained From Mueller Matrix. *Front Chem* 10, (2022).

156. He, C. *et al.* Full Poincaré polarimetry enabled through physical inference. *Optica* 9, 1109–1114 (2022).

157. MARENKO, V. V & Molebnaya, T. V. Optimization of Stokes polarimeters employing a measurement of 4 intensities. *Soviet Journal of optical technology* 57, 452–455 (1990).

158. Sabatke, D. S. *et al.* Optimization of retardance for a complete Stokes polarimeter. *Opt Lett* 25, 802–804 (2000).

159. Azzam, R. M. A., Elminyawi, I. M. & El-Saba, A. M. General analysis and optimization of the four-detector photopolarimeter. *JOSA A* 5, 681–689 (1988).

160. Azzam, R. M. A. Arrangement of four photodetectors for measuring the state of polarization of light. *Opt Lett* 10, 309–311 (1985).

161. Zimnyakov, D. A., Tuchin, V. V & Yodh, A. G. Characteristic scales of optical field depolarization and decorrelation for multiple scattering media and tissues. *J Biomed Opt* 4, 157–163 (1999).

162. Ghosh, N. & Vitkin, I. A. Tissue polarimetry: concepts, challenges, applications, and outlook. *J Biomed Opt* 16, 110801 (2011).

163. Shao, C. *et al.* Analyzing the influence of imaging resolution on polarization properties of scattering media obtained from Mueller matrix. *Front Chem* 10, 936255 (2022).

164. Peinado, A., Lizana, A. & Campos, J. Use of ferroelectric liquid crystal panels to control state and degree of polarization in light beams. *Opt Lett* 39, 659–662 (2014).

165. Guo, Y. *et al.* Adaptive optics based on machine learning: a review. *Opto-Electronic Advances* 5, 200081–200082 (2022).

166. Fu, H.-B. *et al.* Experimental demonstration of deep-learning-enabled adaptive optics. *Phys Rev Appl* 22, 034047 (2024).

167. Rai, M. R., Li, C., Ghashghaei, H. T. & Greenbaum, A. Deep learning-based adaptive optics for light sheet fluorescence microscopy. *Biomed Opt Express* 14, 2905–2919 (2023).

168. Nousiainen, J., Rajani, C., Kasper, M. & Helin, T. Adaptive optics control using model-based reinforcement learning. *Opt Express* 29, 15327–15344 (2021).

169. Hu, Q. *et al.* Universal adaptive optics for microscopy through embedded neural network control. *Light Sci Appl* 12, 270 (2023).

170. Arnoux, C. *et al.* Understanding and overcoming proximity effects in multi-spot two-photon direct laser writing. *Addit Manuf* 49, 102491 (2022).

171. Maibohm, C. *et al.* Multi-beam two-photon polymerization for fast large area 3D periodic structure fabrication for bioapplications. *Sci Rep* 10, 8740 (2020).

172. Winfield, R. J., Bhuian, B., O'Brien, S. & Crean, G. M. Fabrication of grating structures by simultaneous multi-spot fs laser writing. *Appl Surf Sci* 253, 8086–8090 (2007).

173. Shen, Y. *et al.* Polarization Aberrations in High-Numerical-Aperture Lens Systems and Their Effects on Vectorial-Information Sensing. *Remote Sens (Basel)* 14, 1932 (2022).

174. Zhanghao, K. *et al.* Super-resolution dipole orientation mapping via polarization demodulation. *Light Sci Appl* 5, e16166–e16166 (2016).

175. Zhanghao, K. *et al.* Super-resolution imaging of fluorescent dipoles via polarized structured illumination microscopy. *Nat Commun* 10, 4694 (2019).

176. Morizet, J. *et al.* High-speed polarization-resolved third-harmonic microscopy. *Optica* 6, 385–388 (2019).

177. Levinson, H. J. High-NA EUV lithography: current status and outlook for the future. *Jpn J Appl Phys* 61, SD0803 (2022).